Nano Energy 131 (2024) 110282

Contents lists available at ScienceDirect

Nano Energy

journal homepage: www.elsevier.com/locate/nanoen

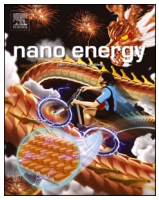

Review

Progress in passivating selective contacts for heterojunction silicon solar cells

Yu Zhang [a,*], Tingshu Shi [a], Leiping Duan [b], Bram Hoex [c], Zeguo Tang [a,*]

[a] College of New Materials and New Energies, Shenzhen Technology University, Shenzhen, Guangdong 518118, China
[b] Hiking PV Technology Co. Ltd., Shenzhen, Guangdong 518109, China
[c] School of Photovoltaic and Renewable Energy Engineering, University of New South Wales, Sydney 2052, Australia

ARTICLE INFO

Keywords:
Photovoltaic
Silicon solar cells
Heterojunction
Passivating selective contacts
Power
Conversion efficiency

ABSTRACT

Photovoltaic (PV) technology, particularly silicon solar cells (SSCs), has emerged as a key player in meeting this demand due to its mature technology, prolonged stability, non-toxicity, and material abundance. Heterojunction (HJT) solar cells have shown significant promise by eliminating dopant-diffusion processes and separating c-Si wafers from metal contacts. In recent years, the notable enhancement in the record PCE of SSCs primarily hinges on advancements in HJT technology, incorporating sophisticated passivating selective contacts. This review explores the evolution and recent progress of passivating selective contacts in HJT solar cells, examining doped silicon-based materials, metal compounds, and organic materials. Despite dopant-free contacts still lagging in efficiency, their potential for high fill factor (FF) values suggests viable pathways for future research. This study aims to provide a comprehensive overview, highlighting key advancements, challenges, and prospects in the ongoing development of HJT technology for higher performance, enhanced stability, and reduced costs.

1. Introduction

The need for energy is unequivocal for human sustenance[1]. Given the anticipated twofold increase in global energy consumption by the midcentury due to population and economic expansion, conserving natural resources becomes paramount[2,3]. Photovoltaic (PV) technology, which harnesses solar energy, is seen as a key means of meeting the escalating demand for electricity while reducing the environmental impact of resource depletion associated with fossil energy technologies [4]. According to The International Technology Roadmap for Photovoltaics (ITRPV), the solar PV market exhibited notable expansion, reaching a record 502 gigawatt (GW) in shipments in 2023[5]. This means we are now truly in the terawatt (TW) era of PV. Silicon solar cells (SSCs) are the predominant PV technology, commanding over 97 % of the market share[5]. Besides technology's maturity, prolonged stability, non-toxicity, and the abundance of materials, this market dominance is mainly attributed to their continuously increased power conversion efficiency (PCE) and reduced levelized cost of electricity (LCOE)[6,7].

Presently, industrial SSCs are dominated by the homojunction crystalline silicon (c-Si) technology, encompassing aluminum back surface field (Al-BSF) cells, passivated emitter and rear contact cells (PERC), tunnel oxide passivated contact cells (TOPCon), heterojunction with intrinsic thin layer cells (HJT or HIT), back contact cells (BC), and so on [8–10]. Thanks to its relatively simple structure, low manufacturing cost and excellent long-term stability, the Al-BSF technology has played a pivotal role in the success of the silicon PV industry during the first fifteen years of the new millennium[5]. A typical p-type Al-BSF cell comprises a phosphorus-doped n^+ emitter and an Al-doped p^+ BSF, formed through a firing process following the screen-printing of Al paste [11]. Nevertheless, the PCE of Al-BSF cells ($\leq$ 20 %) is primarily constrained by the high carrier recombination velocity at the rear surface of the c-Si[12]. To mitigate recombination losses at the rear surface, the PERC technology incorporates a passivation dielectric layer between the rear side of c-Si and Al contacts[13]. A record-breaking PCE of 25.0 % was attained on a lab-scale PERC cell in 1999, employing thermally grown silicon dioxide (SiO_2) passivation on both sides[14]. From 2015 onwards, the market has seen a shift with PERC cell technology overtaking Al-BSF and maintaining its dominance[5]. However, further improving the PCE of the PERC is constrained by severe carrier recombination losses at the metal-silicon contact regions with an induced significant loss in device open-circuit voltage (V_{oc})[15]. In this context, a promising route on PERC is the Tunnel Oxide Passivated Contact (TOPCon) solar cells, which replace the local metal contact for electron collection with a stack of SiO_x/doped poly-Si layer, reducing

* Corresponding authors.
E-mail addresses: zhangyu1@sztu.edu.cn (Y. Zhang), tangzeguo@sztu.edu.cn (Z. Tang).

https://doi.org/10.1016/j.nanoen.2024.110282
Received 22 July 2024; Received in revised form 18 September 2024; Accepted 19 September 2024
Available online 24 September 2024

recombination current density[16,17]. The merit of this configuration lies in the efficient extraction of electrons while simultaneously providing surface passivation[18]. This concept is referred to as passivating selective contact.

For homojunction SSCs, the need for heavy doping in bulk induces Auger recombination, bandgap narrowing, and free carrier absorption in c-Si, limiting the device's overall performance[19,20]. In this regard, HJT SSCs are the most promising solution that eliminates the dopant-diffusion process and entirely separates the c-Si wafer from the metal contacts[21]. In the HJT structure, passivating selective contacts are applied on both sides of the c-Si wafer to form a sandwich structure [22]. Early in 1974, Fuhs and co-workers elucidated the heterojunction concept, presenting a structure comprising hydrogenated amorphous silicon (a-Si:H) on c-Si[23]. Later in the 1990s, Sanyo pioneered the development of the first HJT SSC[24], swiftly attaining a PCE surpassing 21 % by 2005[25]. In a conventional HJT SSC, the dangling bonds on the surface of c-Si are effectively passivated by a-Si:H, which possesses a larger bandgap while being almost identical to c-Si at the nanoscale level [26]. Beyond fostering strong covalent bonds between a-Si and c-Si, the hydrogen atoms in a-Si:H play a crucial role in terminating any residual dangling bonds, thereby enhancing the overall passivation quality[27]. In contrast to homojunction SSCs, HJT SSCs typically exhibit significantly lower recombination rates, leading to high V_{oc} values[28]. Additionally, a-Si:H can be doped, whether n-type or p-type, and provide carrier selectivity in a similar way as doped poly or single crystalline silicon[22]. This selective layer enhances carrier extraction by establishing a unidirectional pathway for either electrons or holes[29].

Over the past decade, the notable enhancement in the record PCE of SSCs primarily hinges on advancements in HJT technology, incorporating sophisticated passivating selective contacts[31]. As of November 2022, the certified highest PCE for single-junction SSCs has achieved 26.81 %, utilizing the HJT structure developed by LONGi. Soon enough, they improved the PCE to 27.30 % by combining the HJT with an interdigitated back-contact (IBC) structure, also known as heterojunction back-contact (HBC) solar cells[32]. Attributed to the superior surface passivation quality and the effective extraction of charged carriers, HJT SSCs have garnered significant research attention, leading to a substantial increase in publication numbers over the past two decades, as shown in Fig. 1a. Recently, Long and coworkers proposed that the practical PCE up limit of HJT SSCs can be as high as 28.5 %, which indicates that there is still room for researchers to explore and enhance the efficiency of HJT SSCs[33–35]. In recent years, great advances have been made in terms of the scope and depth of the passivating selective contacts in HJT SSCs[36]. In addition to conventional a-Si:H(i)/a-Si:H(n or p) stacks, many advanced passivating selective contacts have been devised for this purpose, such as the a-SiO_x(i)/a-SiO_x(n) stacks and dopant-free asymmetric heterocontacts (DASH). Therefore, a progress review screening and discussion of these recent advancements in a broader context is believed to be beneficial for the ongoing development of HJT technology, aiming for higher performance, enhanced stability, and reduced costs.

Recent progress in selective passivating contacts for HJT SSCs classified by doped silicon-based materials, metal compounds, and organic materials has been summarized in Fig. 1b-e. It is clear to see that contacts based on doped silicon-based materials exhibit exceptional electrical properties, achieving high *FF* and V_{oc} values that are approaching their fundamental limits. The most outstanding electrical performance observed for passivating selective contacts is still based on stacks with doped amorphous silicon-based materials, while they suffer from optical losses. The integration of HJT and IBC reports the highest efficiency, which exhibits both superior electrical properties and optical advantages due to the absence of front-side metal contacting that shades part of the front surface of the solar cell. It is also worth mentioning that the electrical performance of passivating selective contacts based on dopant-free compounds is not yet on par with that of doped silicon-based materials contacts with only efficiencies of just over 23 % reported to date. This discrepancy is largely attributed to the more advanced state of silicon-based contacts in terms of the learning curve, benefiting from the processing of billions of cells and enabling more accurate optimization through statistical analysis while dopant-free contacts are only investigated at the lab scale by research institutions [30]. However, it's noteworthy that *FF* values exceeding 80 % have been achieved for all families of dopant-free contacts, suggesting efficient charge-carrier extraction is feasible. Yet, for most metal compound-based contacts, the gap to the FF limit appears notably larger. On the other hand, metal compound-based contacts that achieve V_{oc} values comparable to the best doped-silicon contacts do so by relying on dedicated a-Si:H passivation layers. This underscores that while certain metal compound materials can establish strong asymmetry in carrier conductivity, they lag in terms of surface passivation. Moreover, in comparison to doped-silicon materials and metal compounds, research on passivating selective contacts based on organic materials lags, with the maximum PCE only reaching 21 %. As shown in Fig. 1e, due to their excellent transparency, metal oxides are among the most promising candidates to replace doped silicon materials as passivating selective contacts. However, their passivation quality and selectivity still need improvement, ideally without the use of silicon-based passivation layers.

This study systematically explores passivating selective contacts for HJT SSCs, providing a comprehensive survey of research conducted over the past decade. Section 2 focuses on the fundamental mechanisms and theory of passivating selective contacts. Subsequently, we discuss the evolution of passivation layers for HJT SSCs, emphasizing material modifications. Then, we evaluate various selective layers, categorized into doped silicon-based materials and dopant-free materials, including transition metal oxides, other metal compounds, and organic materials. Finally, we present our perspectives and highlight challenges within this research domain.

2. Mechanisms and theories of passivating selective contacts

2.1. Surface passivation

Because of an abrupt disruption in the periodicity of the silicon crystal, a significant quantity of dangling bonds (DB) are typically present at the silicon interface, leading to a high density of surface states [37]. These states exhibit distributed energy levels throughout the energy bandgap, which serve as highly dynamic centers for electronic recombination, capturing excess electrons and holes[38]. They are characterized by their density D_{it} and capture cross-sections σ_n or σ_p. In situations of non-equilibrium, the driving force for recombination stems from the charge imbalance. The recombination rate is influenced by D_{it}, the surface density of electrons (n_s) and holes (p_s), and the likelihood, per unit time, that an electron or hole will be captured by a specific state. The capture probability relies on $\sigma_{n\ or\ p}$ and the thermal velocity (v_{th}) of the charge carriers. The semiconductor surface's recombination activity can quantified by the so-called surface recombination velocities (often referred as S), where $S_{n0} = v_{th}D_{it}\sigma_n$, and $S_{p0} = v_{th}D_{it}\sigma_p$, corresponding to electrons and holes, respectively. Here, v_{th} is approximately 10^7 cm/s and sets an upper limit for the S values. The capture cross-section ratio of mid-gap defects is notably asymmetric, with a generally higher affinity for electrons. To simplify, D_{it} can be approximated as states at a single energy N_{it} at the mid-gap, given that recombination efficiency is most significant in the middle of the bandgap. During illumination, the net recombination at the surface is defined by a parameter known as the effective surface recombination velocity, S_{eff}, which can be calculated by using the equation below[39,40]:

$$S_{eff} = \frac{U_s}{\Delta \quad n(x=d)} \tag{1}$$

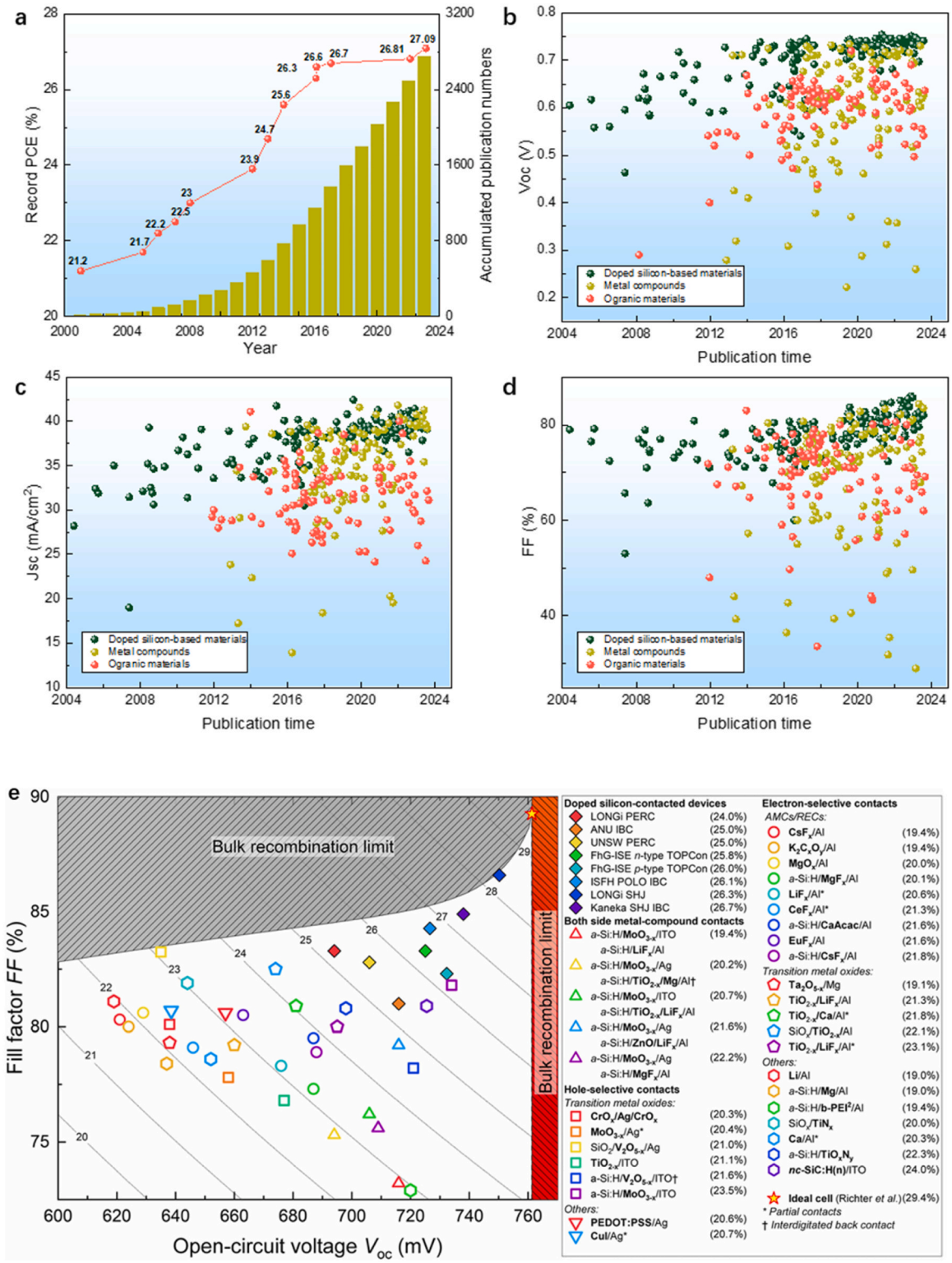

Fig. 1. a) The progress in the record power conversion efficiency (PCE) of heterojunction (HJT) solar cells with accumulated publication numbers during the year 2000–2024. The data on the number of publications is taken from Scopus (www.scopus.com). The progress in selective passivating contacts, classified by doped silicon-based materials, metal compounds and organic materials, for HJT SSCs in terms of a) V_{oc}, b)$J_{sc,}$ and c)*FF* values (data extracted from Tables 1–4). e) A summary of representative passivating selective contacts reported so far and their corresponding device performance. The contour plot illustrates the ideal cell efficiency, assuming a Jsc of 43.31 mA/cm^2, which corresponds to the theoretical Jsc of a 110 μm-thick c-Si solar cell and the star symbol marks this ideal solar cell with an efficiency of 29.43 %. Reproduced with permission from [30] Copyright (2022) John Wiley and Sons.

$$U_s = \frac{v_{th} N_{it} (n_s p_s - n_i^2)}{\frac{n_s + n_1}{\sigma_p} + \left(\frac{p_s + p_1}{\sigma_n}\right)} \tag{2}$$

where U_s represents the surface recombination rate, described by the extended Shockley-Read-Hall (SRH) recombination equation under non-equilibrium conditions[41]. Δn refers to the excess minority carrier concentration at a virtual surface (located at the edge of the space charge region, $x = d$, formed due to surface charge) rather than at the physical silicon surface ($x = 0$). Here, n_i is the intrinsic carrier concentration in Si. Additionally, n_1 and p_1 denote the SRH densities of electrons and holes, respectively, when the energy of the trap level coincides with the Fermi level[42].

There are essentially two methods to decrease S_{eff}. The initial approach involves reducing N_{it} through the deposition of a suitable surface layer with a wider bandgap. Additionally, the bonding nature at the interface can influence the capture cross-section ratio of surface states. This refinement of interface properties is commonly referred to as chemical passivation[43]. Achieving surface chemical passivation involves many methods, such as immersing the wafer in a polar solution and depositing passivation layers to reduce interfacial states or saturating silicon dangling bonds. Usually, many approaches are employed simultaneously, ensuring ample surface chemical passivation to fully saturate the dangling bonds. This makes it an optimal method to prevent carrier recombination for both electrons and holes. Secondly, given that each defect necessitates the presence of both electrons and holes concurrently, the recombination rate reaches its peak when $n_s = p_s$ for asymmetric capture cross-sections. Consequently, minimizing the surface concentration of one of the charge-carrier types substantially reduces the recombination rate. The field-effect passivation, alternatively termed charge-assisted population control, entails reducing either n_s or p_s through an electrostatic field. Field passivation can be achieved by disrupting the equilibrium of carrier concentrations at the interface[44]. The existence of the built-in potential can cause band bending, creating an energy barrier that results in the accumulation or depletion of either carrier type, thus reducing carrier recombination. In the context of SHJ solar cells, the implementation of n-type and p-type selective layers, which enable the unidirectional transport of electrons and holes, respectively, introduces field effect passivation[45].

Silicon wafers with good passivation exhibit a high effective carrier lifetime τ_{eff}, which can be described in the equation below[42]:

$$\frac{1}{\tau_{eff}} = \frac{1}{\tau_{bulk}} + \frac{1}{\tau_{surf}} \tag{3}$$

where τ_{bulk} is the bulk carrier lifetime and τ_{surf} is the surface carrier lifetime. The passivation layers mainly contribute to the enhancement of τ_{surf}. An alternative method for assessing the passivation effect involves the analysis of recombination current density J_0. The surface recombination current density is defined by the equation below[42]:

$$J_{0,surf} = \frac{q n_i^2 S_{eff}}{N_D} \tag{4}$$

where N_D is the doping concentration. In the case of high-performance SHJ solar cells, the τ_{eff} and $J_{0,surf}$ typically exhibit values in the range of several milliseconds and below 2 fA cm^{-2}, respectively[46].

2.2. Charge carrier selectivity

For an SSC to operate effectively, it is imperative to selectively extract photoexcited electrons and holes at the cathode and anode[22]. The interface between the metal and silicon in the conventional SSC experiences a pinning effect, giving rise to the formation of a depletion region in proximity to the contacts. Fermi level pinning (FLP) occurs due to the establishment of a Schottky barrier at the metal-semiconductor interface when the work function of the metal contact is unable to control the concentration of carriers[47]. Fortunately, the mitigation of Fermi-level pinning can be achieved by physically separating the metal electrode from the bulk silicon by using passivating selective contacts. As illustrated in Fig. 2a, this necessitates establishing a path between the absorber and each electrode, showcasing a notable asymmetry in conductivity that favors one type of carrier[30]. This path is well-established by the charge carrier selective layers (CSLs), which exhibit asymmetry transport arising from external doping procedures or its intrinsic material properties[30]. The performance of the solar cell is highly dependent on the strength of this asymmetry. Electron transport layers (ETLs) facilitating electrons, characterized by high electron conductivity and a significantly lower hole conductivity, allow the passage of electrons through the contact region while impeding holes[48]. Conversely, hole transport layers (HTLs) exhibit the opposite conductivity, aligning with hole selectivity.

Brendel and Peibst has proposed a quantitative definition of the carrier selectivity, offering a more straightforward evaluation and comparison of the selectivity across different materials, which is now been widely used both in academic and industry [49]. According to their model, a generalized expression for the carrier selectivity was summarized in Eq. (5) below, with the assumption of ideal perfect Si wafer with unity ideality factor, spatially constant carrier concentrations and recombinations[49].

$$S_{10} = \log\left(\frac{V_{th}(n\mu_n + p\mu_p)}{rW^2} - \left(\frac{np}{n_i^2} - 1\right)\right) \tag{5}$$

where S_{10} is the logarithm of minority carrier selectivity S, V_{th} is the thermal voltage at a temperature of 298.15 K, r represents the recombination rate, W is the wafer thickness, n and p denote for electron and hole concentration, respectively, μ_n and μ_p stand for electron and hole mobility, respectively, and n_i is the intrinsic carrier concentration.

For a typical homojunction solar cell under illumination, the current is carried predominantly by electrons on the phosphorus-diffused regions, owing to the substantial conductivity of electrons[22]. Despite holes experiencing a considerably larger driving force towards the electron contact side, which corresponds to a greater gradient in their quasi-Fermi energy, their current is inferior to the electron current due to their significantly smaller hole conductivity[48]. In contrast, in a conventional HJT solar cell exposed to light, the function of charge separation and selective carrier transport is achieved through the presence of two wide bandgap selective layers with different conductivities for electrons and holes[48]. This configuration guarantees minimal minority carrier conductivity in the wide bandgap transport layers, both in the absence and presence of illumination, reducing carrier recombination at the metal contacts[22].

2.3. Charge carrier transport

When contacting the ETL or HTL with c-Si, comprehending the energy band alignment at the interface of c-Si/CSL is crucial for understanding the mechanisms of charge carrier transport, as shown in Fig. 2b-d.

As shown in Fig. 2b, the materials for the ETL are primarily n-type wide-bandgap semiconductors. They need to exhibit a sufficiently small conduction band offset (ΔE_C) in relation to c-Si. This ensures the smooth transfer of electrons from c-Si to the ETL, while simultaneously preventing the passage of holes due to a large valence band offset (ΔE_V) [50]. For HTL, there are two types of charge transport based on different mechanisms. The first one is analogous to the HTL, as shown in Fig. 2c, having a minimal ΔE_V at the c-Si/HTL interface allows for the effective transport of holes from c-Si to HTL, with electrons being impeded by the large ΔE_C[50]. The second theory is based on the high work function n-type materials, as shown in Fig. 2d and e. Upon the interaction of the high work function n-type materials with c-Si, the energy band alignment results in a pronounced upward band bending on the c-Si surface.

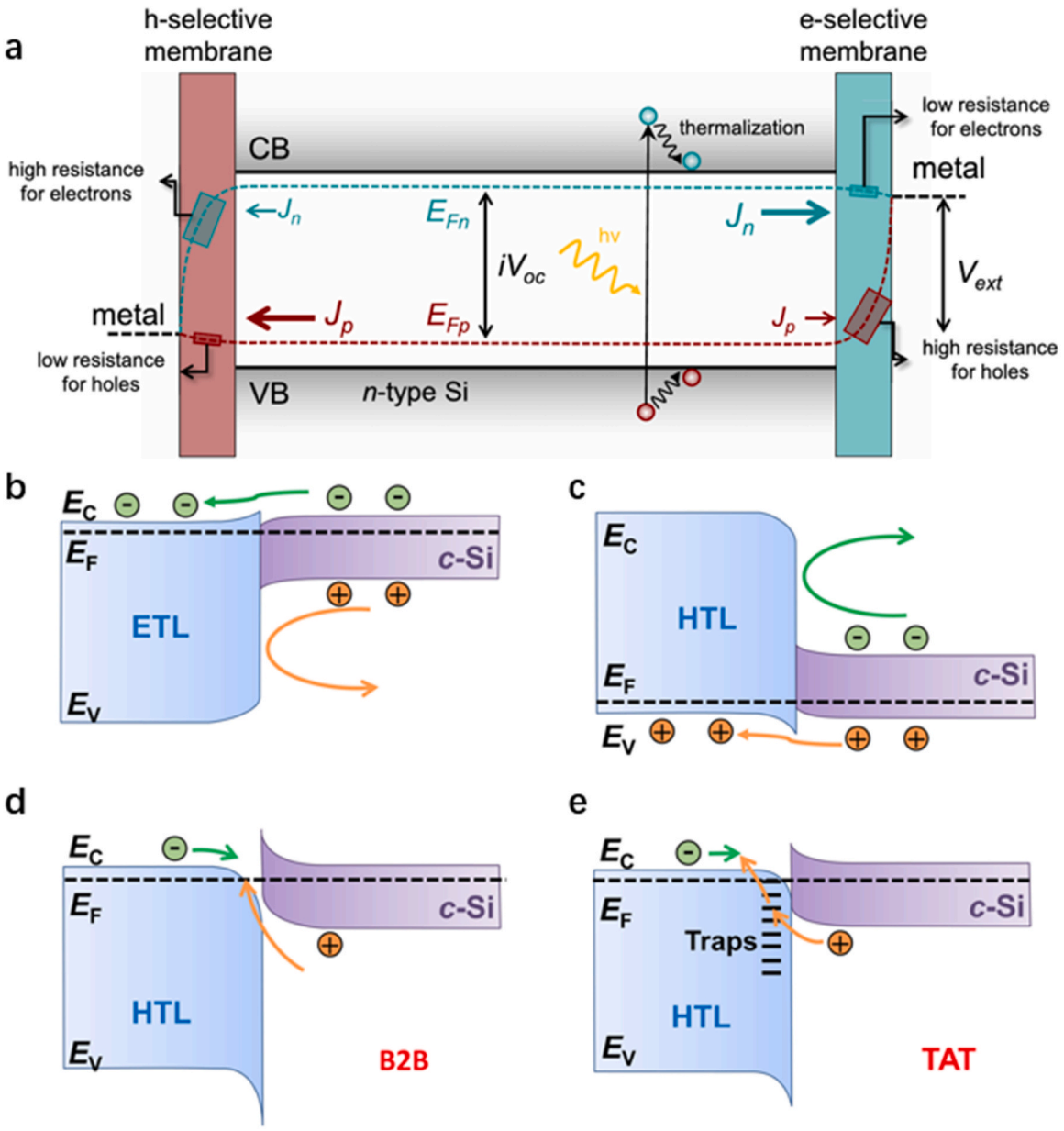

Fig. 2. a) The operational principle of a silicon solar cell: Light absorption creates a non-equilibrium distribution of carriers, using separate quasi-Fermi levels for electrons (EFn) and holes (EFp). Post-excitation, carriers thermalize towards band edges. The free energy difference between quasi-Fermi levels is the implied voltage (iVoc). Electron (Jn) and hole (Jp) currents are driven by quasi-Fermi level gradients and conductivities. Selective membranes on either side of the absorber layer exhibit high conductivity asymmetry, resulting in a voltage build-up (Vext) between metal contacts for work extraction. Reproduced with permission from [30] Copyright (2022) John Wiley and Sons. b) Depicts the band alignment between the n-type Electron Transport Layer (ETL) material and c-Si. Here, a low ΔEC promotes electron transport, while a large ΔEV hinders hole movement. c) Illustrates the band alignment between the p-type Hole Transport Layer (HTL) material and c-Si, where a low ΔEV facilitates hole transport and a large ΔEC prevents electron flow. The band alignment between n-type high Work Function Transition Metal Oxides (TMOs) and c-Si is shown in d) and e), where hole transport is enabled by d) Back-to-Back (B2B) tunneling and/or e) Trap-Assisted Tunneling (TAT). Reproduced with permission from [50] Copyright (2022) John Wiley and Sons.

Given the proximity of the conduction band of these high work function n-type materials to the valence band of c-Si, holes generated in the valence band of the c-Si absorber can traverse the contact interface through a tunneling effect. Subsequently, these holes recombine with electrons in the conduction band of the high work function n-type materials[50]. As illustrated schematically in Fig. 2d and e, the transfer of holes from c-Si to these high work function n-type materials can occur either through band-to-band (B2B) tunneling or trap-assisted tunneling (TAT)[51]. In cases where the conduction band energy (E_C) of high work function n-type materials surpasses the valence band energy (E_V) of c-Si, holes transport via the B2B tunneling mechanism. Conversely, the TAT mechanism prevails if the high work function n-type materials has slightly lower E_C than E_V of c-Si, aided by the abundance of traps near the contact interface[52].

2.4. Contact resistivity

Besides the contact recombination current density (J_{0c}) discussed in section 2.1, contact resistivity (ρ_c) is another important parameter used to evaluate the performance of passivating selective contacts. ρ_c denotes the interface resistance to collected charge carriers in the contact area, indicating the resistive loss. A reduced ρ_c is indicative of a higher *FF*

value, which is highly dependent on the energy level alignment at the interface[53]. Typically, there are two methods that can be used to estimate the ρ_c value, including the transfer length method (TLM) and Cox and Strack method (CSM)[54]. In a conventional TLM measurement, metal electrode stripes are created with varying separation distances. I-V curves are then recorded across pairs of electrodes with different spacings. By fitting the R_T against the spacing between electrode stripes (D), the transfer length (L_T) is derived by extending the fitting curve to the x-axis. The intercept corresponds to $2L_T$, and the y-intercept of the curve represents $2R_C$. The value of R_C can be expressed by using the equation below[55]:

$$R_C = \frac{\rho_c}{L_T Z}\coth\left(\frac{L}{L_T}\right) \tag{6}$$

where Z and L denote the length and width of the metal stripes, respectively.

The conventional CSM utilizes a vertical configuration featuring circular metal electrodes of varying diameters on the front surface and complete metallization on the backside[56]. This design minimizes spreading current, resulting in reduced measurement errors. It is usually assumed that the resistance of the back contact is negligible. Through the measurement of current-voltage (I-V) curves for pads of different diameters, the total resistances (RT) can be expressed using the equation below[57]:

$$R_T = \frac{4\rho_c}{\pi d^2} + \frac{\rho_s}{\pi d}\arctan\left(\frac{4t}{d}\right) + R_0 \tag{7}$$

where d represents the pad diameter, ρ_s denotes the resistivity of Si, t stands for the Si thickness, and R_0 is the residual resistance. By creating a plot of R_T against $1/d$, the ρ_c can be determined through curve fitting [58]. The widespread use of CSM and TLM techniques has facilitated the exploration and evaluation of new CSL materials that demonstrate Ohmic contact with c-Si[59].

It is crucial to recognize that while contacts can be highly selective, they may lack sufficient conductivity, leading to a detrimental drop in fill factor (*FF*). Conversely, some contacts may offer good selectivity but suffer from poor passivation. For instance, in c-Si cells, aluminum back-surface field contacts provide high selectivity and conductivity but underperform due to inadequate passivation. Similarly, an amorphous silicon (a-Si) heterojunction hole contact to c-Si, comprising thick intrinsic and doped a-Si layers, delivers excellent selectivity and passivation, resulting in high iV_{oc} and V_{oc}. However, its poor conductivity diminishes both *FF* and overall efficiency. In summary, a well-designed passivating selective contact must simultaneously offer strong passivation, high conductivity, and effective selectivity, as these factors directly impact key solar cell parameters. Effective passivation enhances quasi-Fermi level (*qFL*) separation, thereby increasing iVoc within the absorber. High conductivity minimizes resistive losses at the maximum power point, preserving a high *FF*. Finally, strong selectivity reduces voltage losses at the contact, allowing the actual V_{oc} to approach or match the iV_{oc}[60].

3. Passivation layers

3.1. Hydrogenated amorphous silicon

In comparison with homojunction solar cells, HJT SSCs usually exhibit superiority in surface passivation, showing a high V_{oc} value. Well-established passivation layers for homojunction solar cells, such as silicon oxides (SiO_x), aluminum oxides (AlO_x), and silicon nitride (SiN_x), have been comprehensively reviewed by other works and will not be focused here[41,61–63]. In a typical HJT SSC, a thin film of a-Si:H(i) is deposited between the selective layer and the c-Si as the passivation layer[64]. It is well known that this a-Si:H(i) passivating layer should possess a high hydrogen content, be grown epitaxially free, and exhibit good optoelectrical properties[65,66]. A high-quality a-Si:H(i) layer and an excellent a-Si:H/c-Si interface can function to inhibit tunneling, reduce dangling bonds, and decrease the complexation rate[67].

Plasma-enhanced chemical vapor deposition (PECVD), a non-invasive and cost-effective approach, is widely used for the preparation of a-Si:H(i) layer[68]. This deposition is a low-temperature process using silane (SiH_4), often diluted by hydrogen (H_2) plasmas, which is a dynamic process, as the entire film undergoes alterations induced by the reactive plasma. During the process, critical factors such as substrate temperature, air pressure, gas ratio, and RF power density should be carefully controlled[69]. The microstructure and optoelectrical properties of the a-Si:H(i) layer play a significant role, where the formation of voids and epitaxial growth deteriorate surface passivation[65]. The layer produced in the intermediate region between the amorphous and crystalline phases has been proven to showcase excellent surface passivation quality[70]. At this stage, the interface between a-Si:H(i) and c-Si is fully relaxed, with minimal electron-active defects[64].

Attaining the high-quality a-Si:H(i) layer involves strategies such as using a higher hydrogen flow rate during deposition and applying pre/post hydrogen plasma treatment[65]. For example, Descoeudres and co-workers demonstrated superior surface passivation by using a multi-step approach involving pure silane plasma deposition followed by hydrogen plasma annealing. They reached carrier lifetimes up to 5.9 ms with 17 nm intrinsic a-Si:H layers on FZ polished wafers[73]. Morales-Vilches and co-workers reported an a-Si:H(i) layer with a higher minority lifetime showing iV_{oc} up to 736 mV by using a diluted plasma with a SiH_4 to H_2 ratio of 1:1[74]. The effectiveness of passivation offered by the a-Si:H(i) layer often reduces after the deposition of the doped a-Si film[75]. This is possibly related to Si-H fracture in the a-Si:H (i) film, where the epitaxial layer can be created after depositing the doped selective layer[76]. In this regard, an intrinsic bilayer passivation method has been proposed[71,77]. In adopting a bilayer approach, the deposition process can be segmented into the initial deposition stage and the growth stage. The function of the initial deposition stage is pivotal for achieving a well-defined interface. During the initial stage, an ultra-thin buffer layer is deposited using a pure silane plasma, followed by the subsequent stage where silane is diluted with hydrogen to complete the deposition[78]. As compared in Fig. 3 a and b, the i1 layer possesses a markedly porous structure, which acts as a barrier to inhibit epitaxial growth[71]. The i2 layer exhibits minimal defects with high compactness, contributing to a denser film and consequently delivering more effective passivation quality than the single-layer passivation[79].

3.2. Hydrogenated amorphous silicon carbides

To impede epitaxial growth, incorporating carbon into the passivation layer proves to be a viable strategy, as carbon atoms contribute to enhancing disorder in the amorphous Si layer[80,81]. Furthermore, hydrogenated amorphous silicon carbides [a-SiC_x:H(i)] demonstrate a higher bandgap up to 4 eV compared to a-Si:H(i), leading to a substantial reduction in parasitic absorption when used as the passivation layer[82,83]. Nevertheless, the efficiency of a-SiC_x:H(i) passivated devices still lag, primarily due to the commonly observed high density of interface traps at the a-SiC_x:H(i)/c-Si interface, particularly with an increased carbon atomic concentration[84]. The introduction of carbon into a-SiC_x:H induces structural defects and inhomogeneities. Ehling and co-workers reported that a reduced carbon content ($[CH_4]/[(CH_4) + (SiH_4)]$) of 1.3 % correlated with a higher minority lifetime value of 1.2 ms. A low absorption strength ratio implies a dense structure when carbon incorporation is low. However, with increased carbon content, the diffusion of hydrogen to the interface is hindered by the stronger C-H bond. This reduction in hydrogen atoms at the a-SiC_x:H(i)/c-Si interface results in a deterioration in passivation quality[85]. The perceived benefits of using carbon do not outweigh the potential drawbacks associated with increased defectiveness in these alloyed layers. Recently, Donercark and co-workers suggested employing a stacked

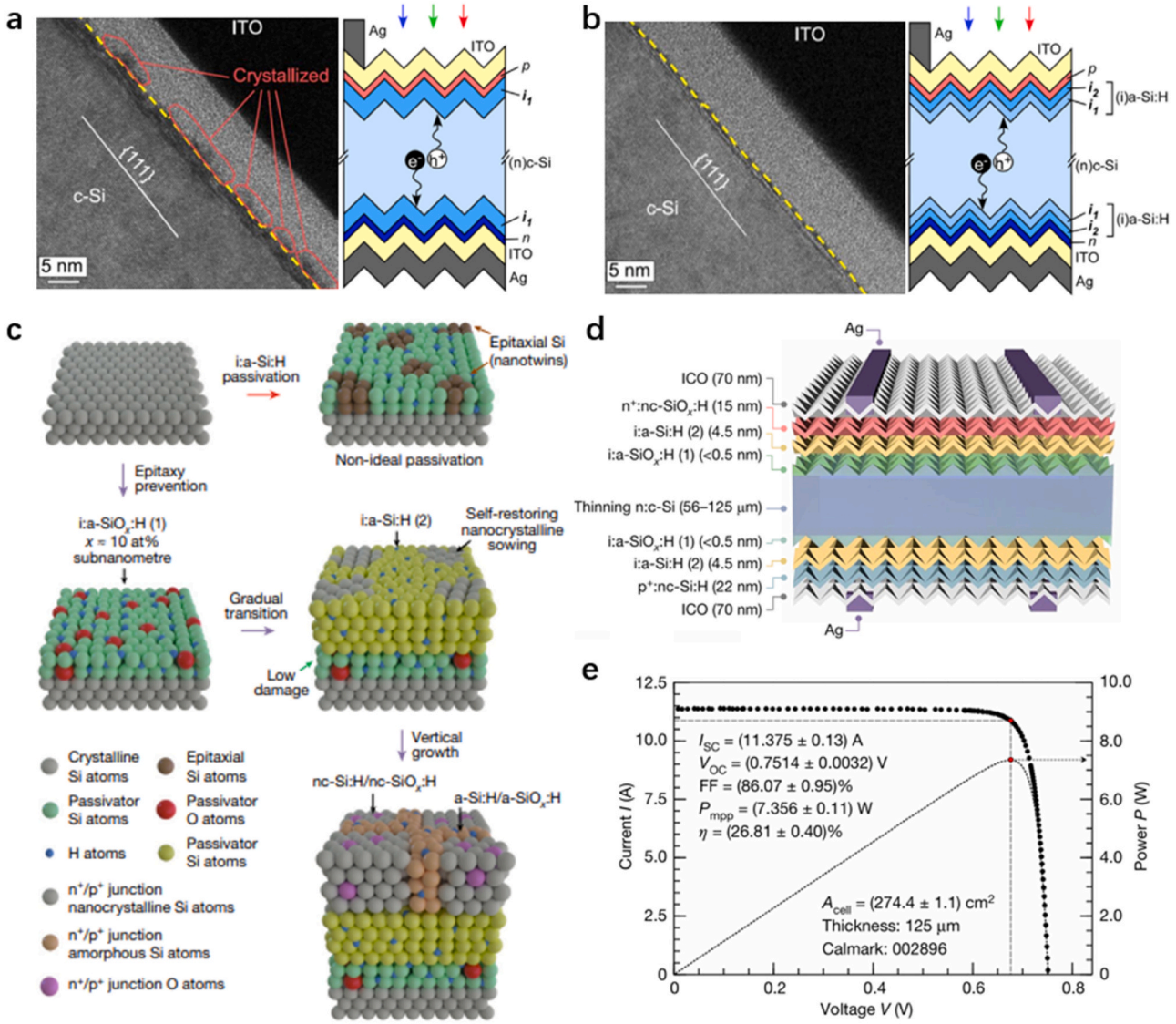

Fig. 3. Cross-sectional TEM images with schematic diagrams of front-junction SHJ solar cells prepared with a) single a-Si:H(i) layer, and b) two-step a-Si:H(i) layers or bilayers (i1 + i2). Reproduced with permission from [71] Copyright 2018 AIP Publishing. c) schematic diagrams detail the continuous-plasma CVD composite gradient passivation, nanocrystalline sowing, and vertical growth induction steps. The continuous plasma CVD process maintains stable RF plasma (fluctuation < ±0.5 %), monitored in real-time with rapid-response regulation to protect the epitaxy-preventing i:a-SiOx:H (1) subnanolayer. The composite gradient passivation involves creating low-damage i:a-SiOx:H (1)/a-Si:H (2) layers with a gradually transitional interface through continuous-plasma CVD. d) Schematic diagrams of the solar cell in Li's work. e) Current density to voltage (J-V) diagram of the champion solar cells in Li's work. Reproduced with permission from [72] Copyright 2024 Springer Nature.

structure comprising a-Si:H(i) and a-SiC_x:H(i) to enhance interface passivation quality and ensure the utilization of the large band gap of a-SiC_x:H(i) to minimize optical absorption losses, simultaneously. By inserting a 3 nm intrinsic a-Si buffer layer between the c-Si and intrinsic a-SiCx layers, they achieved an effective lifetime of 100 μs and an implied open-circuit voltage (iV_{oc}) of 650 mV [84].

3.3. Hydrogenated amorphous silicon oxides

In addition to a-SiC_x:H(i), various efforts have been made to address parasitic absorption in a-Si:H(i) film by incorporating oxygen[86,87]. Hydrogenated amorphous silicon oxides [a-SiO_x:H(i)], possessing higher electronegativity compared to a-SiC_x:H(i), can generate a lower defect state[88]. Ascribed to its tunable band gap and high-quality surface passivation, making a-SiO_x:H(i) a viable passivation layer in HJT SSCs [89]. Utilizing a-SiO_x:H(i) as a passivation material has also been demonstrated to hinder epitaxial growth. This observation is linked to the creation of an abrupt interface by the a-SiO_x:H(i) passivation layer [90]. The a-SiO_x:H(i) passivated cells usually exhibit higher J_{sc} value than a-Si:H(i) passivated cells, due to the wider band gap of a-SiO_x:H(i) film. However, for a-SiO_x:H(i) passivation layer, it is crucial to assess the equilibrium between passivation and carrier transport. Zhang and co-workers observed that an increase in gas ratio of CO_2/CO_2:SiH_4 from 0.33 to 0.4 enhanced ΔE_V, resulting the transport of photogenerated electrons and compensating for absorption losses in the a-SiO_x:H(i) passivation layer due to porosity and high defect density[91]. However, such a gas ratio above 0.4 led to reduced photovoltaic performance, attributed to poor passivation quality on the backside and hindered hole transport due to a higher energy barrier. To avoid such issues and prevent the mismatch of valence band, it is advisable to use the a-SiO_x:H(i) layer as a passivation layer on the front surface field side of the n-type silicon wafer in SHJ solar cells[91]. The a-SiO_x:H(i) passivation layer, when applied to the front side, enhanced J_{SC} value, while a-Si:H(i) functioned as an effective post-passivation interface when used as a

passivation layer on the rear side, culminating in an overall photovoltaic efficiency of 22.2 %[90]. Very recently, Li and co-workers reported a two-step composite gradient passivation approach to address the aforementioned contradiction, as shown in Fig. 3c and d[72]. During the initial stage, a sub-nanolayer (<0.5 nm) of oxygen-containing amorphous silicon (i:a-SiO_x:H (1), x ≈ 10 at%) was deposited on both sides of c-Si using PECVD. This ultrathin passivation layer [i:a-SiO_x:H (1)] serves to disrupt the crystal arrangement periodicity of c-Si without significantly affecting the electrical properties of the passivation contacts. In the subsequent stage, an epitaxy-free layer of amorphous silicon [i:a-Si:H (2)] with a thickness of approximately 4.5 nm was intentionally applied on i:a-SiO_x:H (1). This additional layer enhances the passivation effectiveness and acts as a barrier to isolate the subsequent doping layers from the underlying structure, contributing to an increase in effective lifetime from 2.8 ms to 5.0 ms. As a result, the HJT SSC by using this strategy reached a record PCE of 26.81 % with a high V_{oc} value of 0.751 V, as shown in Fig. 3e[72].

3.4. Other materials

Besides amorphous silicon-based materials, other wide bandgap materials such as metal oxides also exhibit the passivation effects on c-Si. Gerling and co-workers demonstrated that molybdenum oxides (MoO_x), vanadium oxides (VO_x), and tungsten oxides (WO_x) possess inherent passivation capabilities arising from the reduced density of surface electrons due to their high work function[92]. This passivation is further supported by the presence of a SiO_x layer formed through the redox reaction between the metal oxides and c-Si. They highlighted that the induced band bending might be mitigated by dipole effects, and the SiO_x layer formed may exhibit limitations in passivating the interface due to potential defects. Among these three materials, VO_x demonstrates the best passivation effect on n-type c-Si, with an implied V_{oc} of 653 mV and a J_{0c} of 150 fA/cm^2, followed by MoO_x (637 mV and 230 fA/cm^2) and WO_x (543 mV and 420 fA/cm^2). Liao and co-workers illustrated that titanium oxides (TiO_x) can provide effective surface passivation quality through a process involving low-temperature atomic layer deposition (ALD) followed by post-deposition annealing and light-soaking[93]. TiO_x stands out as the most effective surface passivation material among various metal oxides, and notably, it achieves this without the need for a pre-existing SiO_x layer. Recently, Yang and co-workers achieved incremental improvements in TiO_x passivated HJT SSCs, showing iV_{oc} up to 700 mV reaching PCE of 22.1 %[94]. The primary enhancement was attributed to an increased V_{oc} of the cell facilitated by the incorporation of an ultrathin thermally grown SiO_x layer. This addition aimed to enhance surface passivation quality, albeit with a slight rise in contact resistivity.

Nevertheless, it is obvious that these wide bandgap materials cannot provide as effective passivation as with the amorphous silicon-based materials. This can be attributed to the lattice mismatch between these materials and c-Si[43]. There are investigations that distinctly indicate that silicon-based materials deposited through PECVD yield the lowest surface recombination velocity values[43]. On the other hand, the lack of hydrogen during the preparation of these wide bandgap materials as the passivation layer can be another reason.

4. Selective layers

4.1. Doped silicon-based materials

External doping is typically required to achieve charge carrier selectivity in silicon-based materials[95]. Depending on the type of doping, these materials can create an interface between themselves and c-Si that only allows one type of charge carrier to pass through[95]. N-type doped silicon-based materials form electron-selective contacts, while p-type doped silicon-based materials form hole-selective contacts.

As summarized in Table 1, the commonly employed selective layers

Table 1
Summary of device performance using doped silicon-based materials as selective contacts in chronological order.

Publication time	Device structure	Voc (V)	Jsc (mA/cm^2)	FF (%)	PCE (%)	Ref
2004	Ag/ITO/a-Si:H (p)/a-Si:H(i)/n-c-Si/μc-Si(n)/Al	0.605	28.2	79	13.5	[118]
2006	Ag/ITO/nc-Si:H (n)/a-Si:H(i)/p-c-Si/Al	0.558	31.88	79.19	14.09	[119]
2006	Ag/ITO/a-Si:H (n)/pm-Si:H/p-c-Si/Al	0.617	32.4	76.5	15.25	[120]
2007	Al/a-Si:H(p)/p-c-Si/μc−3 C-SiC:H (n)/ITO/Al	0.56	35	72.4	14.2	[121]
2007	Ag/AZO/a-Si:H (n)/a-Si:H(i)/p-c-Si/a-Si:H(p)/Al	0.596	31.46	65.7	12.3	[122]
2007	Al/Si-NC:SiC(p)/n-c-Si/Al/Ti	0.463	19	53	4.66	[123]
2008	Ag/ITO/μc-SiO:H (n)/a-SiO:H(i)/p-c-Si/a-SiO:H(p)/Al	0.62	32.1	77	15.32	[124]
2008	Al/Ag/ITO/μc-SiO:H(p)/a-SiO:H(i)/n-c-Si/a-Si:H(i)/a-Si:H(n)/Ag/Al	0.671	35.2	76	17.9	[125]
2008	Ag/AZO/a-Si:H (n)/p-c-Si/a-Si:H (p)/Al	0.639	39.3	78.9	19.8	[126]
2009	Ag/ITO/nc-Si (n)/a-Si(i)/p-c-Si/Al	0.615	32.5	71	14.2	[127]
2009	Ag/ITO/μc-Si (n)/a-Si(i)/p-c-Si/Al	0.583	30.61	74.2	13.25	[128]
2009	Ag/AZO/a-Si:H (p)/SiO_2/n-c-Si/a-Si:H(n)/Al	0.62	31.9	63.61	12.58	[129]
2009	Ag/ITO/a-Si:H (n)/a-Si:H(i)/p-c-Si/Al	0.585	34.63	74.7	15.14	[130]
2009	Al/Ag/ITO/μc-SiO:H(p)/a-SiO:H(i)/n-c-Si/a-Si:H(i)/a-Si:H(n)/Ag/Al	0.665	34.9	77	17.8	[131]
2010	Al/Ag/ITO/nc−3 C–SiC:H (n)/p-c-Si/μc-Si1-xOx:H(p)/Al	0.668	36.7	73.1	17.9	[132]
2010	Ag/ITO/a-Si:H (p)/a-Si:H(i)/n-c-Si/a-Si:H(i)/a-Si:H(n)/ITO/Ag	0.717	38.2	74.2	20.3	[73]
2011	Al/Ag/ITO/a-Si:H(p)/a-Si:H(i)/n-c-Si/a-Si:H(i)/a-Si:H(n)/Al	0.631	36.27	76.13	17.43	[133]
2011	Ag/ITO/a-Si:H (p)/a-Si:H(i)/n-c-Si/a-Si:H(i)/a-Si:H(n)/BZO/Ag	0.694	31.4	76	16.5	[134]
2011	Ag/ITO/a-Si:H (n)/a-Si:H(i)/p-c-Si/μc-SiOx:H(p)/Al	0.659	34.7	80.9	18.5	[135]
2011	Ag/GZO/a-Si:H (p)/a-Si:H(i)/n-c-Si/GZO/Ag	0.612	37.1	76	17.27	[136]
2011	Ag/ITO/a-Si:H (p)/a-Si:H(i)/n-c-	0.69	39.1	72.7	19.6	[137]

(continued on next page)

Table 1 (*continued*)

Publication time	Device structure	Voc (V)	Jsc (mA/cm^2)	FF (%)	PCE (%)	Ref
	Si/a-Si:H(i)/a-Si:H(n)/ITO/Ag					
2012	Al/ZnO/a-Si:H(n)/a-Si:H(i)/p-c-Si/Al	0.59	33.6	71	14.1	[138]
2013	Ag/IO:H/ITO/a-Si:H(p)/a-Si:H(i)/n-c-Si/a-Si:H(i)/a-Si:H(n)/ITO/Ag	0.727	38.9	78.4	22.1	[139]
2013	Ag/SiOx/ITO/a-Si:H(p)/a-Si:H(i)/n-c-Si/a-Si:H(n)/Al	0.662	35.7	74	17.6	[140]
2013	Ag/Al/ITO/a-Si:H(p)/a-Si:H(i)/n-c-Si/a-Si:H(i)/a-Si:H(n)/Al	23.43	35.1	73.2	17.1	[141]
2013	Ag/BZO/a-Si:H(p)/n-c-Si/a-Si:H(n)/ITO/Ag	0.593	35.26	78.05	16.3	[142]
2013	Ag/Al/ITO:Zr/a-Si:H(p)/a-Si:H(i)/n-c-Si/a-Si:H(i)/a-Si:H(n)/Al/Ag	0.71	33.66	72.4	17.31	[143]
2014	Ag/ITO/In2O3/a-Si:H(p)/a-Si:H(i)/n-c-Si/a-Si:H(i)/a-Si:H(n)/ITO/Ag	0.67	37.42	71.16	17.84	[144]
2014	Ag/ITO/a-Si:H(p)/a-Si:H(i)/n-c-Si/a-Si:H(i)/a-Si:H(n)/Ag	0.647	38.1	74.7	18.41	[145]
2014	Ag/ITO/a-Si:H(p2)/a-Si:H(p1)/a-Si:H(i)/n-c-Si/a-Si:H(i)/a-Si:H(n)/ITO/Ag	0.725	33.82	77.41	19	[146]
2014	Al/ITO/a-Si:H(n)/a-Si:H(i)/p-c-Si/Al	0.72	35.5	73	18.66	[147]
2014	AZO/μc-Si:H(p)/a-Si:H(i)/n-c-Si/a-Si:H(i)/μc-Si:H(n)/AZO/Al	0.708	34.35	79.1	19.2	[148]
2015	Al/Ag/ITO/a-Si:H(p)/a-Si:H(i)/n-c-Si/a-Si:H(i)/μc-Si:H(n)/Al.	0.696	36.09	71	18.06	[149]
2015	Ag/ITO/μc-Si1-xOx:H(p)/a-Si:H(i)/a-SiO_x:H(i)/n-c-Si/a-SiO_x:H(i)/a-$Si_{1-x}O_x$:H(n)/Ag/Al	0.738	33.46	77	19	[150]
2015	Ag/IZO/a-Si:H(p)/a-Si:H(i)/n-c-Si/a-Si:H(i)/a-Si:H(n)/ITO/Ag	0.722	38.6	78.5	21.5	[151]
2015	Ag/IWO/a-Si:H(p)/a-Si:H(i)/n-c-Si/a-Si:H(i)/a-Si:H(n)/IWO/Ag	0.73	38.3	80.44	22.5	[152]
2015	Ag/IWO/a-Si:H(n)/a-Si:H(i)/n-c-Si/a-Si:H(i)/a-Si:H(p)/IWO/Ag	0.727	38.56	78.48	22.03	[153]
2015	Ag/BZO/a-Si:H(p)/a-Si:H(i)/n-c-Si/a-Si:H(i)/a-Si:H(n)/BZO/Ag	0.628	41.75	67.8	17.78	[154]

Table 1 (*continued*)

Publication time	Device structure	Voc (V)	Jsc (mA/cm^2)	FF (%)	PCE (%)	Ref
2016	Ag/ITO/a-Si(p)/n-c-Si/a-Si(n)/ITO/Ag	0.618	40.1	74.1	18.4	[155]
2016	Ag/ITO/nc-SiO_x:H(n)/a-Si:H(i)/n-c-Si/a-Si:H(i)/nc-SiO_x:H(p)/ITO/Ag	0.704	37.7	76.7	20.4	[156]
2016	Ag/ITO/a-Si:H(p2)/a-Si:H(p1)/a-Si:H(i)/n-c-Si/a-Si:H(i)/a-Si:H(n)/ITO/Ag	0.71	38.77	75.43	20.78	[157]
2016	Ag/ITO/μc-SiO_x:H(p)/a-SiO_x:H(i)/n-c-Si/a-SiO_x:H(i)/μc-SiO_x:H(n)/AZO/Ag	0.646	35.83	75.5	17.47	[157]
2016	Ag/ITO/a-Si:H(p)/a-Si:H(i)/n-c-Si/a-Si:H(i)/μc-Si:H(n)/ITO/Ag	0.721	36.9	79.3	21.1	[44]
2016	Ag/IWO/a-Si:H(p)/a-Si:H(i)/n-c-Si/a-Si:H(i)/a-Si:H(n)/IWO/Ag	0.737	38.3	78	22.5	[158]
2016	Ag/ITO/μc-SiO_x:H(n)/a-SiO_x:H(i)/p-c-Si/μc-SiO_x:H(p)/AZO/a-Si:H textures/AZO/Ag	0.646	38.5	72.9	18.15	[159]
2016	Ag/ITO/a-Si:H(n)/a-Si:H(i)/p-c-Si/SiO_x/Si(i)/SiC_x(p)/ITO/Ag	0.694	37.2	79.1	20.44	[160]
2016	Ti/Ag/ITO/nc-Si:H(p)/a-Si:H(i)/n-c-Si/a-Si:H(i)/nc-SiO_x:H(n)/AZO/Ag	0.727	38.8	74.5	21	[161]
2017	Ag/AZO/a-Si:H(p)/a-Si:H(i)/n-c-Si/Al	0.551	33.39	71.1	13.09	[162]
2017	Ag/In_2O_3:H/a-Si:H(n)/a-Si:H(i)/n-c-Si/a-Si:H(i)/a-Si:H(p)/ITO/Ag	0.73	39.18	73.9	21.13	[163]
2017	Ti/Ag/ITO/a-Si:H(n)/a-Si:H(i)/p-c-Si/BSF/Al	0.594	36.98	72.93	16.02	[164]
2017	Ag/ITO/μc-SiC:H(n)/μc-SiO_x:H(n)/a-SiO_x:H(i)/p-c-Si/a-SiO_x:H(i)/μc-SiO_x:H(p)/ITO/Ag	0.677	37.6	74.2	28.9	[165]
2017	Ag/ITO/a-Si:H(n)/a-Si:H(i)/n-c-Si/a-Si:H(i)/a-Si:H(p)/In_2O_3:H/Ag	0.68	40.2	60	16.3	[166]
2017	Ag/Al/ITO/μc-SiO:H(p)/a-SiO:H(i)/n-c-Si/a-SiO:H(i)/a-Si:H(n)/Al/Ag	0.715	34.9	78	19.4	[167]
2017	Ag/Al/ITO/μc-$Si_{(1-x)}O_x$:H/a-$Si_{(1-x)}O_x$:H/n-c-Si/a-$Si_{(1-x)}O_x$:H/a-Si:H/Ag/Al	0.701	32.8	76.8	17.7	[168]
2017	Al/Ag/ITO/μc-SiO_xC_y:H(p)/a-Si:H(i)/a-SiO_x:H(i)/	0.702	35.32	76.3	18.9	[169]

(*continued on next page*)

Table 1 (*continued*)

Publication time	Device structure	Voc (V)	Jsc (mA/cm^2)	FF (%)	PCE (%)	Ref
	n-c-Si/a-SiO_x:H (i)/a-Si:H(n)/Ag					
2017	Al/Ag/ITO/a-SiO_x(In)/n-c-Si/Al	0.54	30.5	74.2	12.2	[170]
2017	Ag/SiO_x/IWO/a-Si:H(p)/a-Si:H (i)/n-c-Si/a-Si:H (i)/a-Si:H(n)/IWO/Ag	0.739	38.74	80.64	23.08	[171]
2017	Ag/ITO/μc-SiO_x:H(p)/a-Si:H(i)/n-c-Si/a-Si:H(i)/a-Si:H(n)/ITO/Ag	0.616	35	71.35	15.38	[172]
2017	Ag/ITO/a-Si:H (n)/a-Si:H(i)/n-c-Si/a-Si:H(i)/p-SiC_x/ITO/Ag	0.714	38.8	79.8	21.9	[173]
2017	Ag/IWO/a-Si:H (n)/a-Si:H(i)/n-c-Si/a-Si:H(i)/a-Si:H(p)/IWO/Ag	0.745	39	79	22.74	[174]
2017	Ag/ITO/nc-SiO_x:H(n)/a-Si:H(i)/n-c-Si/a-Si:H(i)/a-Si:H(p)/ITO/Ag	0.729	40	80	21.6	[175]
2017	Ag/ITO/a-Si:H (n)/a-Si:H(i)/n-c-Si/a-Si:H(i)/a-Si:H(p)/ITO/Ag	0.731	37.46	79.3	21.71	[176]
2018	Ag/ITO/nc-SiO_x:H(n)/nc-Si:H(n)/n-c-Si/a-Si:H(i)/a-Si:H(p)/ITO/Ag	0.731	38.3	80.6	22.6	[97]
2018	Ag/ITO/nc-Si:H (n)/mp-SiO_x(n)/chem.SiO_x/n-c-Si/a-Si:H(i)/a-Si:H(p)/ITO/Ag	0.691	33.9	79.4	18.6	[177]
2018	Ag/ITO/MoO_x/a-SiO_x(Mo)/n-c-Si/a-SiO_x/poly-Si (n)/Al	0.6	38.2	72.9	16.7	[178]
2019	Ag/AZO/nc-Si:H (n)/a-Si:H(i)/n-c-Si/a-Si:H(i)/a-Si:H(p)/ITO/Ag	0.73	39.94	78	22.6	[179]
2019	Ag/ITO/μc-SiO_x:H(n)/μc-SiO_x:H seed layer/a-Si:H (i)/n-c-Si/a-Si:H (i)/μc-SiO_x:H(p)/ITO/Ag	0.727	39	77	21.8	[102]
2019	Ag/ITO/a-Si:H (p)/a-Si:H(i)/n-c-Si/a-Si:H(i)/a-Si:H(n)/AZO/Ag	0.726	40.81	80.87	23.96	[180]
2019	Ag/AZO/nc-Si:H (n)/a-Si:H(i)/n-c-Si/a-Si:H(i)/a-Si:H(p)/AZO/Ag	0.72	39.1	75.4	21.2	[181]
2019	Ag/ITO/a-Si:H (p)/a-Si:H(i)/n-c-Si/μc-SiO_x:H/poly-Si(n)/Ag	0.719	38.15	76.91	21.1	[182]
2019	Ag/IFO:H/nc-SiO_x(p)/a-Si:H (i)/n-c-Si/a-Si:H (i)/nc-SiO_x(n)/IFO:H/Ag	0.702	38.32	78.08	21.01	[183]
2019	Ag/IZrO/ITO/a-Si:H(n)/a-Si:H (i)/n-c-Si/a-Si:H (i)/a-Si:H(p)/ITO/Ag	0.742	38.18	82.4	23.59	[184]
2020	Ag/ITO/μc-SiC:H (n)/SiO2/n-c-Si/a-Si:H(i)/a-Si:H (p)/ITO/Ag	0.737	39.5	77.1	21.6	[185]
2020	Ag/MGZO/a-Si:H (p)/a-Si:H(i)/n-c-Si/a-Si:H(i)/a-Si:H(n)/MGZO/Al	0.706	36.72	73.3	19.02	[186]
2020	Al/AZO/a-Si:H (n)/a-Si:H(i)/p-c-Si/a-Si:H(p)/Al	0.744	42.43	83.7	25.26	[187]
2020	Ag/ITO/nc-SiO_x:H(p)/nc-Si:H(p)/a-Si:H(i)/n-c-Si/a-Si:H(i)/nc-Si:H (n)/nc-SiO_x:H (n)/nc-Si:H(n)/a-Si:H(n)/ITO/Ag	0.712	39.3	78.6	22	[188]
2020	Ag/ITO/μc-SiO_x:H(n)/seedlayer/a-Si:H(i)/n-c-Si/a-Si:H(i)/a-Si:H (p)/ITO/Ag	0.740	39.19	82.33	23.87	[189]
2020	Ag/ITO/nc-Si:H (n)/nc-SiO_x:H (n)/a-Si:H(i)/n-c-Si/a-Si:H(i)/a-Si:H(p)/ITO/Ag	0.739	38.7	80.7	23.1	[190]
2020	Ag/TCO/nc-SiO_x:H(n)/a-Si:H(i)/n-c-Si/a-Si:H(i)/p^+/TCO/Ag	0.729	39.99	78.06	22.77	[191]
2020	Ag/ITO:Zn(Ar)/ITO:Zn(O_2)/a-Si:H(p)/a-Si:H(i)/n-c-Si/a-Si:H(i)/a-Si:H(n)/Ag	0.739	39.12	75.97	21.96	[192]
2020	Ag/SiN_x/SiO_2/n^+/n-c-Si/mp-Si(i)/SiO_x/mp-Si(i)/μc-Si(p)/ITO/Ag	0.707	39.45	80.3	22.4	[193]
2020	Ag/ITO/poly-SiC_x(n)/SiO_x/p-c-Si/SiO_x/poly-SiC_x(p)/ITO/Ti/Pd/Ag	0.741	38.1	81.6	23	[194]
2020	Ag/ITO/nc-Si:H (n)/a-Si:H(i)/n-c-Si/a-Si:H(i)/a-Si:H(p)/AZO/Ag	0.73	39	77	21.9	[195]
2020	Ag/ITO/a-Si:H (n)/a-Si:H(i)+Catdoping/n-c-Si/a-Si:H(i)/a-Si:H(p)/ITO/Ag	0.723	39	79	21.2	[196]
2020	Ag/ITO/nc-SiO_x:H(n)/a-Si:H(i)/n-c-Si/a-Si:H(i)/nc-SiO_x:H(p)/ITO/Ag	0.719	38.85	80.41	22.47	[197]
2020	Ag/ITiO/a-Si:H (n)/a-Si:H(i)/n-c-Si/a-Si:H(i)/a-Si:H(p)/ITiO/Ag	0.736	39.14	82.7	23.81	[198]
2020	Ag/IWOH/nc-Si:H(p)/a-Si:H(i)/n-c-Si/a-Si:H(i)/a-Si:H(n)/IWOH/Ag	0.733	39.48	81.4	23.54	[199]
2020	Ag/ITO/a-Si:H (n)/a-Si:H(i)/n-c-	0.741	39	81.6	23.6	[200]

(*continued on next page*)

Table 1 (*continued*)

Publication time	Device structure	Voc (V)	Jsc (mA/cm^2)	FF (%)	PCE (%)	Ref
	Si/a-Si:H(i)/a-Si:H(p)/AZO/Ag					
2021	Ag/ITO/a-Si:H(p)/a-Si:H(i2)/a-Si:H(i1)/n-c-Si/a-Si:H(i1)/a-Si:H(i2)/a-Si:H(n)/ITO/Ag	0.724	39.1	81.1	23	[201]
2021	Ag/Au/Ti/SiN_x/a-Si:H(n)/a-Si:H(i)/n-c-Si/a-Si:H(i)/a-Si:H(p)/TCO/Ag	0.729	38.3	79.9	22.34	[202]
2021	Ag/ITO/nc-SiO_x:H(n)/a-Si:H(i)/n-c-Si/a-Si:H(i)/a-SiO_x:H(p)/nc-SiO_x:H(p)/ITO/Ag	0.729	40.5	80	23.6	[203]
2021	SiN_x/a-Si:H(i)/n-c-Si/a-Si:H(i)/nc-Si:H(n)/ITO/Ag	0.71	41.3	78.2	22.9	[204]
2021	Ag/MgF_2/IWO/a-Si:H(n)/a-Si:H(i)/n-c-Si/a-Si:H(i)/a-Si:H(p)/IWO/Ag	0.731	40.16	78.07	22.92	[205]
2021	Ag/ITO/nc-SiO_x:H(n)/a-Si:H(i)/n-c-Si/a-Si:H(i)/a-Si:H(p)/ITO/Ag	0.731	39.8	81.4	23.7	[206]
2021	Ag/IWTO/a-Si:H(n)/a-Si:H(i)/c-Si(n)/a-Si:H(i)/a-Si:H(p)/IWTO/Ag	0.746	38.7	82.9	23.8	[207]
2021	Ag+Al/ITO/nc-Si:H(p^+)/nc-SiOx:H(p)/nc-Si:H(p)/a-Si:H(i)/n-c-Si/a-Si:H(i)/n^+/ITO/Al	0.678	36.6	77	19.11	[208]
2021	Ag/ITO/nc-Si:H(p)/a-Si:H(i)/n-c-Si/a-Si:H(i)/a-Si:H(n)/ITO/Ag	0.754	37.85	81.5	23.27	[209]
2021	Ag/ITO/a-Si:H(p)/a-Si:H(i)/n-c-Si/SiO_x/nc-SiO_x(n)/ITO/Ag	0.724	38.95	75.9	21.4	[210]
2021	Ag/IWO/nc-SiO_x:H(n)/a-Si:H(i)/n-c-Si/a-Si:H(i)/a-Si:H(p)/IWO/Ag	0.744	38.3	84.4	24.09	[211]
2021	Ag/SiO_2/TCO/nc-Si:H(n)/a-Si:H(i)/n-c-Si/a-Si:H(i)/a-Si:H(p)/TCO/SiO_2/Ag	0.747	39.79	82.79	24.61	[212]
2021	Ag/ITO/nc-Si:H(n)/a-Si:H(i)/n-c-Si/a-Si:H(i)/a-SiO_x:H(p)/nc-Si:H(p)/ITO/Ag	0.714	38.82	80.1	22.2	[213]
2022	Ag/ITO/nc-SiO_x(p)/a-Si:H(i)/n-c-Si/SiO_x/poly-Si(n)/ITO/Ag	0.71	39.3	79	22	[214]
2022	Ag/Al_2O_3/IZO/a-Si:H(n)/a-Si:H(i)/n-c-Si/a-Si:H(i)/a-Si:H(p)/ITO/Ag	0.74	40.53	72.33	21.57	[215]
2022	Ag/IWO/a-Si:H(n)/a-Si:H(i)/n-c-Si/a-Si:H(i)/a-Si:H(p)/ITO/Ag	0.719	38.68	82.07	22.84	[216]
2022	Ag/ITO/a-Si:H(p)/a-Si:H(i)/n-c-Si/a-Si:H(i)/a-Si:H(n)/ITO/Ag	0.681	38.06	79.38	20.56	[217]
2022	Ag/IWO/a-Si:H(n)/a-SiO_x:H(i)/n-c-Si/underdense a-Si:H(i)(HPT)/a-Si:H(p)/IWO/Ag	0.735	39.02	77.57	22.23	[90]
2022	Ag/IMO:H/μ-Si:H(n)/n-c-Si/a-Si:H(i)/a-Si:H(p)/ITO/Ag	0.746	40	84.64	25.26	[218]
2022	Ag/ITO/nc-Si:H(n)/a-Si:H(i)/n-c-Si/a-Si:H(i)/a-Si:H(p)/ITO/Ag	0.742	39.27	82.2	23.95	[219]
2022	Ag/ITO/n-poly-SiO_x/SiO_x/n-c-Si/a-Si:H(i)/a-Si:H(p)/ITO/Ag	0.723	40.9	81	23.95	[220]
2022	Ag/ITO/AZO/ITO/a-Si:H(n)/a-Si:H(i)/n-c-Si/a-Si:H(i)/a-Si:H(p)/AZO/Ag	0.738	38.62	83.4	23.8	[221]
2022	Cu/IMO/nc-SiO_x:H(n)/a-Si:H(i)/n-c-Si/a-Si:H(i)/a-Si:H(p)/ITO/Cu	0.746	40.24	85.08	25.54	[222]
2023	Ag/ITO/nc-SiO_x(n)/SiO_x/nc-Si/SiO_x/n-c-Si/SiO_x/nc-Si/SiO_x/nc-SiO_x(p)/ITO/Ag	0.732	39.5	77.95	22.55	[223]
2023	Ag/ITO/a-Si:H(p)/a-Si:H(i)/n-c-Si/a-Si:H(i)/a-Si:H(n)/Al	0.718	36.5	77.5	20.3	[224]
2023	Ag/ITO/a-Si:H(p)/a-Si:H(i)/n-c-Si/a-Si:H(i)/a-Si:H(n)/ITO/Ag	0.722	40.33	79.6	23.19	[225]
2023	Ag/IZO/a-Si:H(n)/a-Si:H(i)/n-c-Si/a-Si:H(i)/a-Si:H(p)/IZO/Ag	0.743	38.35	84.22	24.02	[226]
2023	Ag/MgF_2/ITO/cond.nc-SiC:H/passi nc-SiC:H/SiO_2/n-c-Si/a-Si:H(i)/a-Si:H(p)/ITO/Ag	0.739	41.19	82.7	25	[227]
2023	Ag/IWO/a-Si:H(n)/a-Si:H(i)/n-c-Si/a-Si:H(i)/a-Si:H(p)/GZO/Ag	0.74	38.87	82.13	23.65	[228]
2023	Ag/ITO/μc-SiO_x:H(n)/a-Si:H(i)/n-c-Si/a-Si:H(i)/a-Si:H(p)/ITO/Ag	0.745	39.89	84.85	25.22	[229]
2023	Ag/TCO/nc-SiO_x:H(n)/a-Si:H(i)/n-c-Si/a-Si:H(i)/nc-Si:H(p)/TCO/Ag	0.751	41.45	86.07	26.81	[230]
2023	Ag/IHfO:H/μc-Si:H(n)/a-Si:H(i)/n-	0.745	40.09	83.79	25.03	[231]

(*continued on next page*)

Table 1 (*continued*)

Publication time	Device structure	Voc (V)	Jsc (mA/cm^2)	FF (%)	PCE (%)	Ref
	c-Si/a-SiOH(i)/a-Si:H(p)/ITO/Ag					
2023	Ag/ITO/μc-SiO_x:H(n)/a-Si:H(i)/n-c-Si/a-SiO_x:H(i)/a-Si:H(p)/ITO/Ag	0.742	39.98	85.74	25.44	[232]
2023	ITO/a-Si:H(p)/a-Si:H(i)/n-c-Si/a-Si:H(n)/Aerogel/Ag	0.734	39.76	80.3	23.42	[233]
2023	Ag/IMO:AZO/μ-Si:H(n)/a-Si:H(i)/n-c-Si/a-Si:H(i)/μ-Si:H(p)/IMO:AZO/Ag	0.747	40.1	85.48	25.62	[218]
2023	Ag/SiO_x/IZrO:H/nc-Si:H(p)/nc-SiO_x:H(p)/nc-Si:H(p)/SiO_x/a-Si:H(i)/n-c-Si/a-Si:H(i)/a-Si:H(n)/nc-Si:H(n)/ITO/MgF_2/Ag	0.731	40.74	82.05	24.44	[234]
2023	Ag/a-SnO2/nc-SiO_x:H(n)/a-Si:H(i)/n-c-Si/a-Si:H(i)/nc-Si:H(p)/a-SnO_2/Ag	0.714	39.37	78.9	22.18	[235]
2023	Ag/ICO/nc-Si:H(n)/a-Si:H(i)/n-c-Si/a-Si:H(i)/nc-Si:H(p)/IZrO/Ag	0.747	39.98	82.18	24.55	[236]
2023	Ag/ITO/a-Si:H(n)/a-Si:H(i)/c-Si(n)/a-Si:H(i)/WO_x/Ag	0.697	37.86	79.61	21.01	[237]
2023	Ag/AlO_x/ITO/a-Si:H(n)/a-Si:H(i)/n-c-Si/a-Si:H(i)/a-Si:H(p)/ITO/AlO_x/Ag	0.742	39.2	82.6	24	[238]
2024	Ag/GZO+ITO/nc-SiO_x:H(n)/a-Si:H(i)/c-Si(n)/a-Si:H(i)/nc-Si:H(p)/ITO/Ag	0.741	39.12	82.03	23.8	[239]
2024	Ag/ITO/a-Si:H(i) with Cat-doping/c-Si(n)/a-Si:H(i)/a-Si:H(p)/ITO/Ag	0.734	39.83	81.18	23.76	[240]

are doped a-Si:H layers, which induce the necessary band bending for c-Si/ doped a-Si:H. These layers mitigate recombination losses by establishing an adequate electric field at the interface[98,99]. Adequate band bending facilitates the unimpeded transport of one type of charge carriers while impeding the movement of carriers of opposite polarity, as shown in Fig. 4a. These layers, typically 5–6 nm thick, are deposited with appropriate doping using agent gases such as trimethyl boron (TMB), biborane (B_2H_6), and phosphine (PH_3). These films are deposited using the PECVD method in the same equipment as the intrinsic a-Si:H layers. Therefore, the optical and electrical properties of doped a-Si:H films are also significantly influenced by deposition parameters such as process temperature, pressure, and the flow rates of H_2 and SiH_4 gases [65]. The outstanding electrical properties of doped a-Si:H layers are pivotal in enhancing the performance of HJT solar cells, signifying significant advancements in their PCE[28,100]. Indeed, numerous reported HJT solar cells with high PCE values over 25 % are founded on doped a-Si:H selective layers[72,100]. However, to enhance the PCE of HJT solar cells further, doped a-Si:H selective layers face constraints. Undesirable parasitic optical absorption can arise across the ultraviolet and visible spectrums of the solar spectrum owing to the relatively narrow band gap and the high defect density within the doped a-Si:H[101]. Moreover, silicon-based materials must be adequately doped to facilitate effective carrier separation and collection, while a-Si:H exhibits a low doping efficiency[44].

This has sparked increasing interest, particularly in the past five years, in utilizing doped hydrogenated nanocrystalline silicon (nc-Si:H) materials as a substitute for doped a-Si:H, potentially incorporating oxygen to form a mixed-phase nanocrystalline silicon oxide alloy [102–104]. As shown in Fig. 4b, hydrogenated nanocrystalline silicon-based materials comprise a combination of amorphous and nanostructured phases[105–107]. Essentially, nc-Si:H, nc-SiO_x:H, and nc-SiC_x:H can be viewed as nanostructured silicon embedded within a-Si:H, a-SiO_x:H, and a-SiC_x:H, respectively[108–110]. The alloying characteristics of nc-SiO_x:H and nc-SiC_x:H contribute to their wider band gaps, which serve to reduce optical absorption. For example, as shown in Fig. 4 c and d, switching the front selective contact layer from nc-Si:H(n) to the nc-SiO_x:H(n), the loss in absorption can be reduced by 0.63 mA/cm^2[97]. For integrating these nanocrystalline silicon materials into HJT solar cells, achieving rapid nucleation without compromising passivation quality or hindering current collection is a challenge [111]. Köhler and co-workers observed that employing hot wire chemical vapor deposition (HWCVD) for depositing nc-SiC_x:H(n) at elevated filament temperatures (T_f) leads to a reduction in i-V_{OC}[112]. This decrease is attributed to the higher hydrogen density at elevated T_f (1850°C), causing etching of the SiO_x passivation layer. A similar effect is observed when nc-SiO_x:H(n) is utilized as selective layers[113]. This phenomenon arises from the elevated T_f, which prompts hydrogen in the precursor gas to permeate through microcrystalline and amorphous silicon thin films. Subsequently, hydrogen gradually accumulates within micropores at the interface of a-SiO_x:H(i)/c-Si, leading to a reduction in passivation quality[113]. Nevertheless, achieving high T_f is crucial for attaining high conductivity. As T_f increases within the range of 1700–1900°C, conductivity escalates significantly by nine orders of magnitude[112]. The conductivity in nc-SiC_x:H(n) primarily originates from its nanostructured phase[114]. By introducing only a small amount of doping gas (a few ppm), nc-Si:H can achieve a much higher electrical conductivity compared to the a-Si:H layer[115]. Consequently, materials like nc-SiC_x:H and nc-SiO_x:H exhibit superior conductivity and more pronounced field-effect passivation compared to a-Si:H[115].

Nevertheless, it's important to note that such high conductivity can only be achieved after the nucleation stage. Initiating microcrystalline nucleation necessitates the presence of loosely connected silicon networks. This helps lower the energy barrier for transitioning from a-Si:H to nc-Si:H, especially under high-hydrogen dilution conditions[116]. In pursuing high-efficiency cells, it's vital to deposit highly conductive nanolayers, ensuring sufficiently high crystallization, on a thin intrinsic passivation layer while maintaining excellent passivation quality in the intrinsic layer[97,111]. Employing a pre-deposition treatment has been identified as crucial, whether by employing an oxidizing plasma for p-type layers or by utilizing a high-phosphorous-doped seed layer for n-type layers[104,117]. Mazzarella and co-workers observed that while achieving a higher J_{sc} without a seed layer (nc-Si:H), there was a clear lower effective lifetime of 1.3 ms and iV_{oc} of 727 mV[97]. However, they achieved a high cell performance of 22.6 % by depositing a seed layer of nc-Si:H before the nc-SiO_x:H layer. Similarly, Pham and co-workers demonstrated that a nc-SiO_x:H layer with a nc-Si:H seed layer can facilitate a swift transition from an amorphous to a nanocrystalline phase, leading to increased PCE. It is worth mentioning that the world record cell with the PCE of 26.81 % is also based on doped nc-SiO_x:H selective layers. They pioneered a self-repairing nanocrystalline seeding technique, enabling doped contact layers to sprout and propagate upward from the pre-established nano seeds, creating pathways for "photogenerated carrier superhighways" between the

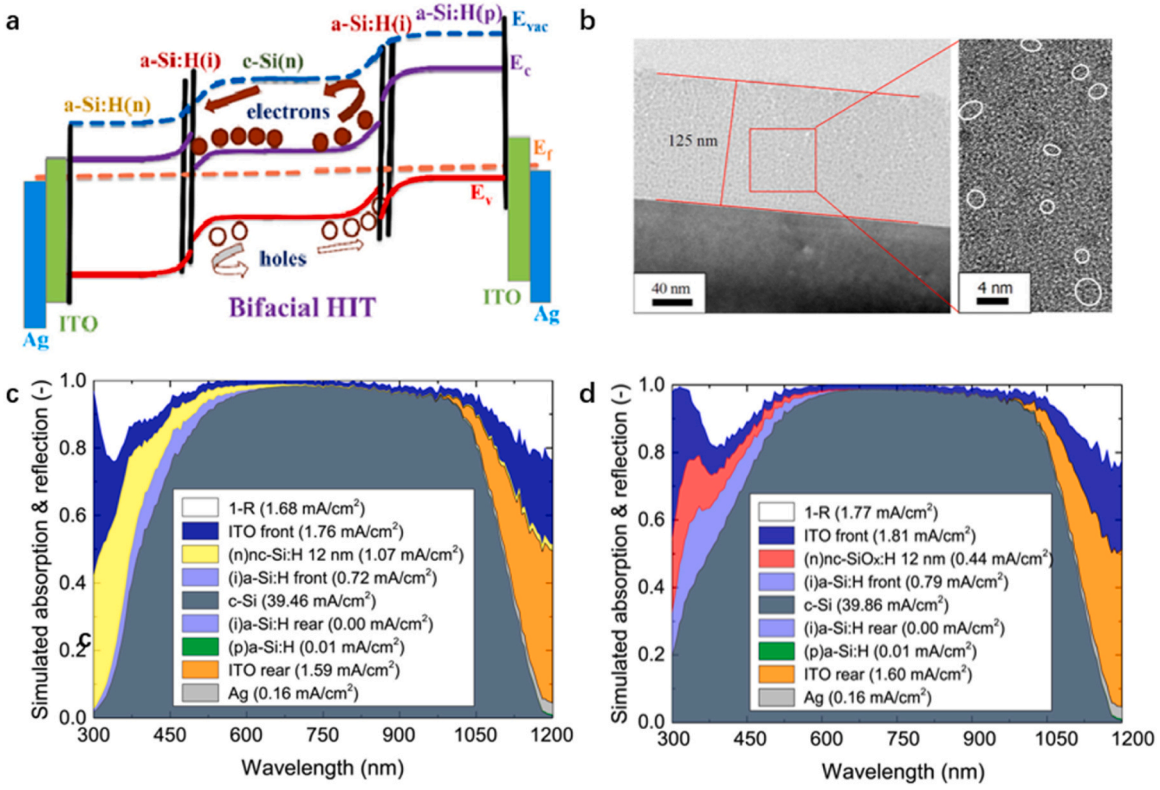

Fig. 4. a) Schematic diagrams of the band bending in HJT solar cells with doped a-Si:H as selective layers on both sides.Reproduced with permission from [65] Copyright 2018 Springer Nature. b) TEM and HRTEM image of nc-SiOx:H/a-SiOx:H multilayer film, where inset shows the nanocrystal phase embedded in silicon oxide matrix [96]. Simulated absorption and reflection spectra for HJT solar cells with c) doped (n)nc-Si:H and d) doped (n)nc-SiOx:H as the selective layer. Reproduced with permission from [97] Copyright 2018 Elsevier.

upper and lower layers[72].

In summary, the use of doped silicon-based materials as selective layers has demonstrated promising results for achieving high performance in HJT solar cells. However, their relatively low bandgap still leads to significant parasitic absorption, limiting further enhancements in PCE. Additionally, the doping process is environmentally unfriendly and expensive, requiring toxic doping sources and capital-intensive equipment. So far, there is debate on the optimal doping concentration in the a-Si layers to achieve the best balance between high conductivity and minimized recombination losses. High doping improves carrier transport but may increase defect density. As an alternative, a dopant-free approach is emerging, aiming to replace doped Si materials with wide bandgap materials to mitigate parasitic absorption losses. The selection and extraction of free charge carriers can be achieved without resorting to doping methods, as the energy band offset inherent to the material's work function allows for the same mechanism. A sufficiently high or low work function can maintain either an accumulation or inversion regime at the surface when illuminated, thereby enabling asymmetric electron or hole conduction. Also, these dopant-free materials can be produced using simple and cost-effective deposition techniques such as thermal evaporation and solution-processed methods, potentially reducing production costs

4.2. Dopant-free materials

4.2.1. Metal oxides

Transition metal oxides (TMOs) represent a significant category of dopant-free solutions with work functions spanning from 3.5 eV to 7 eV, primarily falling under the classification of wide bandgap semiconductors, as shown in Fig. 5a. These layers boast exceptional transparency, stability, and availability, providing a suitably aligned conduction or valence band offset concerning silicon. Additionally, TMO layers exhibit minimal parasitic losses. Compared to doped silicon-based materials, TMO selective layers offer advantages in terms of lower deposition costs and greater compatibility with industrial processes. TMOs, characterized by their high work function, function as hole-selective layers due to their n-type nature, which arises from the presence of oxygen vacancies in their atomic structure. Commonly utilized HTLs include MoO_x, WO_x, and VO_x[241–243]. These layers' elevated work functions result in hole accumulation near the surface, inducing band bending in the c-Si absorber and facilitating high hole conductivity. Materials such as TiO_x, HfO_x, ZnO, and TaO_x serve as ETLs, with their high electron conductivity promoting electron collection at the terminal[244–247]. Several research groups have proposed the formation of an interface dipole in conjunction with band bending as the mechanism for carrier collection[53,59]. For TMOs, their electronic characteristics, including electron affinity (E_A), work function (WF), and other factors, significantly influence the band alignment with c-Si and thus determine carrier selectivity[50]. The WF and conductivity of TMOs primarily depend on the number of oxygen deficiencies, which can be affected by factors such as substrates, fabrication techniques, and post-deposition treatments[248–251].

So far, the PCE of HJT solar cells utilizing TiO_x or MoO_x as the selective layer has steadily increased, while those utilizing other TMOs as the selective layers, such as WO_x, VO_x, ZnO, and TaO_x, have lagged. Therefore, the widely reported TiO_x and MoO_x will be discussed as illustrative examples. Regarding TiO_x as the ETL, theoretical simulations indicate that when the E_A of TiO_x falls within the range of 3.6–4.0 eV, the interfacial recombination rate tends to be low, potentially leading to high PCE in solar cells[256]. If the E_A of TiO_x is less than 3.6 eV, it can enhance the built-in electric field, but this may lead to increased recombination and compromise cell efficiency[253]. Conversely, if the E_A of TiO_x exceeds 4 eV, it can result in a higher energy barrier for electron transport. However, empirically reported E_A of TiO_x typically

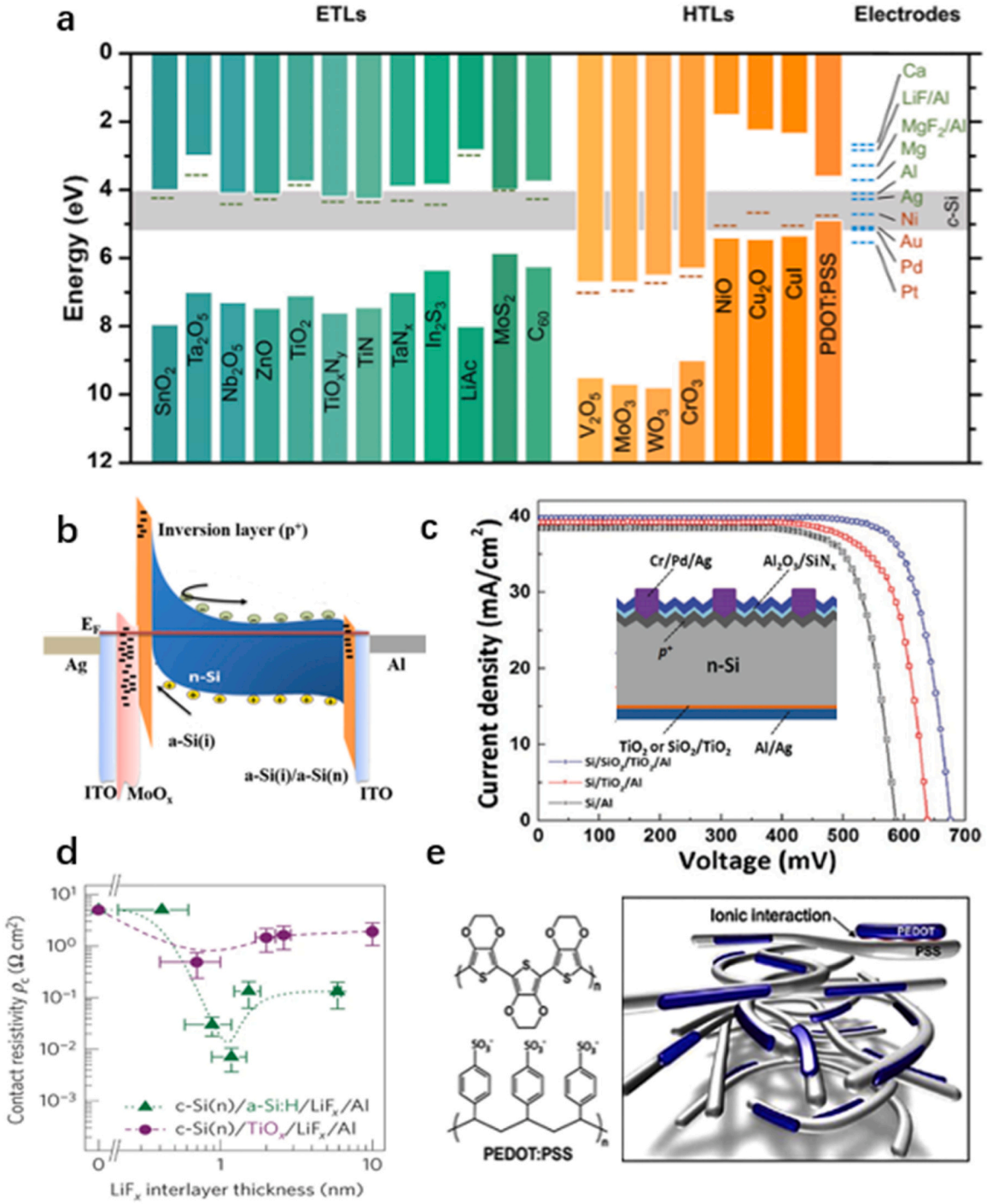

Fig. 5. a) Bandgap diagrams and WF positions (dashed lines) of typical dopant-free selective materials including metals, metal compounds, and organic materials, referenced to c-Si energy band edges (gray bar). Energy levels are indicative and vary with deposition methods, stoichiometry, and doping concentrations. Reproduced with permission from [50] Copyright 2022 John Wiley and Sons. b) The Band diagram demonstrated the carrier transport mechanism of the HJT solar cell based on MoOx as the selective layer. Reproduced with permission from [252] Copyright 2021 Elsevier. c) Structure and J-V curves of HJT solar cell featuring a TiOx or SiOx/TiOx stack selective contact. Reproduced with permission from [253] Copyright 2016 John Wiley and Sons. d) Contact resistance vs. LiFx thickness for heterocontacts with TiOx (purple) and a-Si:H (i) (green) interlayers. Reproduced with permission from [254] Copyright 2016 Springer Nature. e) Chemical molecular structure and morphology of PEDOT:PSS. Reproduced with permission from [255] Copyright 2017 The American Association for the Advancement of Science.

falls between 4.0 and 4.3 eV[257]. Wu and co-workers discovered that E_A of TiO_x varies with the Ti/O ratio, and a relatively high E_A can be achieved with a high oxygen content in the TiO_x film[258]. Zhu and co-workers found that annealing under continuous H_2 and Ar flux can create oxygen vacancies in TiO_x, the concentration of which can be utilized to adjust the E_A of TiO_x (ranging between 2.2 and 4.5 eV) and conductivity in a controlled manner[259]. Regarding MoO_x as the HTL, which exhibits WF range from 4.5 eV to 6.9 eV, theoretical calculations suggest that it needs a sufficiently high WF (>5.5 eV) to ensure effective field-effect passivation at the contact interface, reducing surface recombination and achieving optimal V_{oc} with limited requirements for chemical passivation[56,260]. The higher WF of MoO_x positions its Fermi energy level closer to the valence band of c-Si, causing the creation of a larger conduction band offset at the MoO_x/c-Si interface,

inducing more efficient hole inversion, as shown in Fig. 5**d**[51,252]. This phenomenon has been illustrated by Mehmood and co-workers, wherein adjusting the WF of MoO_x from 4.5 eV to 5.7 eV led to PCE of HJT solar cells increased from 1.62 % to 23.32 %[261]. Battaglia and co-workers discovered that subjecting evaporated MoO_x films deposited on gold substrates to UV-ozone exposure for 30 minutes can elevate its WF to as high as 6.6 eV[262]. Gregory and co-workers found that HF treatment could further increase the WF of MoO_x, as observed from UPS spectra[263].

In the context of device performance, as summarized in Table 2, for the first time, TiO_x deposited using a modified CVD process was applied on the front side of p-Si solar cells as ETL, resulting in a PCE of 7.1 % [264]. However, this was constrained by high carrier recombination on both sides and poor lateral conductivity of TiO_x. Later, Yang and co-workers achieved a breakthrough with TiO_x ETL by developing an ALD-deposited TiO_x-based contact, which provided excellent surface passivation and low contact resistivity simultaneously[253]. A low effective surface recombination velocity of 11 cm/s, equivalent to a J_0 of approximately 20 fA/cm^2, was achieved on n-Si passivated with a 5.5 nm ALD TiO_x layer[253]. Chao and co-workers integrated ALD-TiO_x into the structure of a-Si:H(i)/TiO_x/low-WF metal contact. This configuration successfully achieved high-quality passivation and a low contact resistivity, resulting in an 18.2 % efficient device. As a result, there was no longer a need for a heavily doped a-Si:H layer[265]. In 2016, Yang and co-workers made gradual advancements in solar cells with TiO_x as the ETL, achieving a PCE of 22.1 %[94,253,266]. The primary enhancement stemmed from enhancing the V_{oc} of the cell through the incorporation of an extremely thin thermally grown SiO_x layer, which enhanced surface passivation quality albeit with a minor rise in contact resistivity, as shown in Fig. 5**c**. Furthermore, these studies also highlighted the significant contribution of the capping Al electrode to electron selectivity. Indeed, while the a-Si:H/TiO_x stack demonstrated impressive surface passivation qualities, the illuminated J-V curve of the device featuring an a-Si:H/TiO_x contact displays an "S-shape," suggesting inadequate electron selectivity[267,268]. Besides Al, using a low WF material for capping, such as LiF, Ca, and Yb, has proven effective in enhancing the electron selectivity of TiO_x-based ETLs[241,269,270]. Through the integration of a partial TiO_x/LiF and TiO_x/Ca passivating contact on n-Si solar cells, remarkable efficiencies of 23.1 % and 21.8 % were attained, respectively[241,269]. Similarly, with Yb capping, a textured Si/a-Si:H/TiO_x/Yb hetero-contact exhibited a very low ρ_c (~1 mΩ•cm^2), leading to a noteworthy PCE of 19.2 %[270].

Compared to other TMOs, MoO_x is more widely reported as the HTL in HJT solar cells. In 2011, Park and co-workers presented a study where they achieved a 6.26 % efficiency in a-Si:H based thin film solar cells by employing thermally evaporated MoO_x film instead of a-SiC_x:H(p) films [271]. Following this, in 2014, Battaglia and co-workers integrated MoO_x films into HJT solar cells to replace the a-Si:H(p) layers, resulting in significant optical improvements[272]. This enhancement led to a total photocurrent increase of 2.4 mA/cm^2 and achieved a high efficiency of 18.8 %, V_{oc} of 711 mV, and J_{sc} of 39.4 mA/cm^2[272,273]. Later, Cho and co-workers investigated the interface properties and thermal stability of MoO_x films, achieving a PCE of 19.3 %, V_{oc} of 724 mV, and FF of 0.74[274]. HJT solar cells were fabricated using a 10 nm thick MoO_x film, resulting in a PCE of overpassing 20 % and an effective minority carrier lifetime of 2.3 ms[275]. Recently, Kumar and co-workers achieved a high PCE of 20 %, V_{oc} of 695 mV, FF of 0.74, and J_{sc} of 38.9 mA/cm^2[275,276]. Jinhun and co-workers reported a high V_{oc} of 730 mV, FF of 0.78, and efficiency of 21.3 % with a 3 nm thick MoO_x HTL[277]. More recently, Geissbuhler and co-workers achieved an efficiency of 22.5 % and FF of 80 % using a MoO_x HTL[278]. So far, the highest device PCE employing the MoO_x HTL in HJT solar cells is 23.83 %, as reported by Cao and co-workers[279]. They utilized a 4-nm thick MoO_x layer, deposited via thermal evaporation, positioned between an a-Si:H passivating layer and an tungsten-doped indium oxide (IWO) and MgF_2 stack. The exceptional device performance primarily stems from the superb passivation offered by the intrinsic a-Si:H layer, along with the high transparency and good selectivity of the thin MoO_x layer.

It is worth mentioning that the electronic characteristics of TMOs can be impacted by various factors during solar cell fabrication, including exposure to air, contact with reducing agents, and heating, all of which may influence the ultimate performance of the solar cell. Exposure to air, for instance, can lead to the reduction of metal oxides through reactions with hydrogen and water, or the adsorption of additional elements such as carbon and other metals[30,92]. For example, MoO_x as HTL can induce instability in HJT solar cells[262,280,281]. Before and after the contact annealing process, oxidation occurs, leading to a reduction in the WF of MoO_x and an increase in the ρ_c, consequently impairing the photoelectrical performance. The conditions of annealing and plasma processing, as well as the stability of the deposited MoO_x layer, may dictate the formation of an interfacial a-SiO_x layer within the a-Si:H(i)/MoO_x stack[282]. Moreover, unless a pre-annealing step of the a-Si:H layer before MoO_x deposition is implemented, degradation of the MoO_x film can transpire during annealing for screen-printed metallization, triggered by hydrogen effusion from the adjacent a-Si:H(i) layer, thereby detrimentally impacting hole extraction and transport from the c-Si wafer[283]. Herein, although TMOs as selective layers in HJT solar cells continuously achieved promising PCE results, there is the ongoing debate over how much efficiency can be sacrificed for improved stability. For example, MoO_x can be sensitive to environmental factors, which can lead to degradation of the device over time. More investigations are required to evaluate their stabilities. It's worth compromising slightly on efficiency if the passivating contacts significantly enhance stability, while others prioritize immediate gains in efficiency.

4.2.2. Other metal compounds

Besides TMOs, various other metal compounds such as halides, nitrides, sulfides, phosphides, and carbonates have been explored as dopant-free selective layers for HJT solar cells[348,371–379]. Among these materials, metal halides exhibit minimum parasitic absorption loss due to their large band gap, usually larger than 10 eV[379]. Several studies have demonstrated that metal halide films, deposited via thermal evaporation and thinner than 10 nm, exhibit crystalline structures, such as rock-salt or fluorite configurations. Schottky and Frenkel defects are frequently observed in these ionic solids, leading to the trapping of carriers and the formation of F- or H- centers, thus allowing for the generation of small-radius polarons[380]. Because these defects have a lower energy of formation at the surface compared to the bulk, there is a suggestion that the charge accumulation at the interface with other materials aids in charge transport[381,382]. Inspired by the organic semiconductors, many initial studies are based on LiF_x in HJT solar cell, which successfully demonstrated that LiF_x can reduce series resistance significantly as ETL[383,384]. The LiF_x, known for its extremely low work function of approximately 2.9 eV, can achieve very low contact resistances of around 1 mΩ•cm^2 and 7 mΩ•cm^2 on the c-Si/LiF_x and c-Si/a-Si:H(i)/LiF_x HJT structure, as shown in Fig. 5**d**[254]. A PCE of 19.4 % was achieved on HJT solar cells utilizing full-area LiF_x ETL[254]. This was subsequently improved to 20.7 % by implementing a TiO_x/LiF_x bilayer design with enhanced thermal stability[244]. In 2016, James and co-workers reported a PCE of 20.6 % by using a partially contacted LiF_x as ETL, attributed to its remarkably low contact resistivity[385]. In addition to the LiF_x, the MgF_x with low WF of around 3.5 eV is also widely investigated, where the c-Si/MgF_x and c-Si/a-Si:H(i)/MgF_x HJT demonstrated a low ρ_c value of approximately 35 mΩ•cm^2 and 76 mΩ•cm^2, respectively[376]. In 2016, Cuevas and co-workers achieved a PCE of 20.1 % by using MgF_x as the ETL in HJT solar cells[376]. Later on, Ballif and co-workers improved this PCE to 22.1 % by using Mg capping on top of MgF_x in the IBC device structure[386]. Moreover, there are also many studies focused on other metal halides, including KF_x, CaF_x, and CsF_x as the ETL, and CuI as the HTL, however their device

Table 2
Summary of device performance using metal oxides as selective contacts in chronological order.

Publication time	Device structure	Voc (V)	Jsc (mA/cm^2)	FF (%)	PCE (%)	Ref
2013	Ag/Al/ITO:Zr/a-Si:H/n-c-Si/Al	0.71	34.44	74.83	18.3	[284]
2014	Ag/ITO/MoO_x/a-Si:H(i)/n-c-Si/a-Si:H(i)/a-Si:H(n)/ITO/Ag	0.711	39.4	67.2	18.8	[272]
2014	Ag/MoO_3/PEDOT:PSS/n-c-Si/Liq/Al	0.63	29.2	74.9	13.8	[285]
2015	Ag/ITO/MoO_x/a-Si:H(i)/n-c-Si/a-Si:H(i)/a-Si:H(n)/ITO/Ag	0.725	38.6	80.36	22.5	[278]
2015	Ag/ITO/V_2O_x/n-c-Si/a-$SiC_{0.2}$:H(i)/a-Si:H(n)/a-SiC:H/Ti/Al	0.606	34.4	75.3	15.7	[242]
2016	SiN_x/SiO_2/n-c-Si/V_2O_x(Cs_2O_3)/Ag	0.61	38.85	70	16.59	[286]
2016	Ag/ZnO NW/p-c-Si/Al	0.52	48.31	36.46	9.17	[287]
2017	Ag/PEDOT:PSS/n-c-Si/TiO_x/Al	0.643	30.7	72.4	14.3	[288]
2017	Ag/ITO/V_2O_5/n-c-Si/a-$SiC_{0.2}$:H(I)/a-$Si_{0.2}$:H(n)/a-SiC:H/Ti/Al	0.605	34.5	74.7	15.6	[289]
2017	Ag/ITO/MoO_x/a-Si:H(i)/n-c-Si/a-Si:H(i)/BZO/Ag	0.599	38.12	72.7	16.6	[290]
2017	Ag/Al_2O_3/SiNx/p+/n-c-Si/SiO_2/TiO_2/Al	0.676	39.6	80.7	21.6	[267]
2017	Al/AZO/$Zn_{1-x}Mg_xO$/ZnO-NR/p-c-Si/Al	0.49	37	72	13.2	[291]
2017	Ag/ITO/WOx/a-Si:H(i)/n-c-Si/a-Si:H(i)/a-Si:H(n)/ITO/Ag	0.705	32	76	16.8	[292]
2017	Ag/ITO/a-Si:H(n)/a-Si:H(i)/n-c-Si/a-Si:H(i)/a-Si:H(p)/MoO_x/ITO/Ag	0.73	37.25	77.5	21.8	[277]
2017	Ag/ITO/MoO_x/a-Si:H(i)/n-c-Si/a-Si:H(i)/a-Si:H(n)/ITO/Ag	0.724	39.05	74.5	20.7	[293]
2017	Ag/PEDOT:PSS/n-c-Si/TiO_2/Al	0.62	31	75.96	14.6	[294]
2017	Ag/TiO_2/PDMS/PEDOT:PSS/n-c-Si/Al	0.632	31.98	76.74	15.51	[295]
2017	Ag/ITO/MoO_x/n-c-Si/MgO_x/Al	0.595	32.6	73.4	14.2	[51]
2018	ITO/MoO_x/n-Si/SiO_x/low-WFMs(Mg)	0.71	39.1	78.5	21.8	[296]
2018	Ag/p-(Cu_2O:N/CuO:N/CuO:Pd/CuO)/Ti/n-c-Si/Al	0.46	28.5	63	8.3	[297]
2018	Ag/PEDOT:PSS/n-c-Si/AZO/Al	0.641	27.6	78	13.6	[298]
2018	Ag/ITO/MoO_x/n-c-Si/a-Si:H(n)/GaP/ITO/Ag	0.598	34.3	69	14.1	[299]
2018	Ag/ITO/MoO_x/a-Si:H(i)/n-c-Si/a-Si:H(i)/a-Si:H(n)/ITO/Ag	0.71	36.75	75.9	20.8	[283]
2018	Ag/ITO/NiO:Cu/n-c-Si/n^+/Mg/Al	0.378	35.6	67.7	9.1	[300]
2018	Ag/ITO/ZnS/p-c-Si/WO_3/Ag	0.525	33.75	61.73	10.94	[301]
2018	Ag/ITO/NiO:Cu/SiO_x/n-c-Si/Mg	0.428	36.2	69.4	10.8	[302]
2018	PEDOT:PSS/MoO_x/Ag/PEDOT:PSS/SiNWs/n-c-Si/Al	0.622	33.5	78	16.3	[303]
2018	Ag/ITO/a-Si:H(p)/a-Si:H(i)/n-c-Si/a-Si:H(i)/TiO_x/Ca/Al	0.711	35.1	72.9	18.2	[265]
2018	Ag/TiO_2/SiNWs/n-c-Si/Al	0.553	18.4	60.3	6.15	[304]
2018	Ag/ITO/MoO_x/n-c-Si/a-$SiC_{(0.2)}$(i)/a-Si:H(n)/a-SiC:H(BRC)/Al	0.614	32.8	73.2	14.7	[305]
2018	Ag/ITO/a-Si:H(p)/a-Si:H(i)/n-c-Si/a-Si:H(i)/AZO/Al	0.672	38.23	71.95	18.46	[306]
2018	Ag/ITO/MoO_x/a-SiO_x:H/n-c-Si/a-SiO_x:H/a-Si:H(n)/ITO/Ag	0.675	31.7	77.4	16.6	[307]
2018	Ag/AZO/n-CdS/p-c-Si/MoO_3/Ag	0.543	28.75	68.13	10.64	[308]
2018	Ag/PEDOT:PSS/n-c-Si/SnO_2/Ag	0.593	33.16	72	14.16	[309]
2018	Ag/ITO/MoO_x/n-SiNWs/Cs_2CO_3/Al	0.631	38.1	70.2	16.9	[310]
2018	Ag/PEDOT:PSS/n-c-Si/a-Si:H(i)/Li-ZnO/Al	0.623	33.58	72.38	15.14	[311]
2018	Ag/ITO/MoOx/a-Si:H(i)/n-c-Si/a-Si:H(i)/a-Si:H(n)/ITO/Ag	0.69	38.88	74	20	[276]
2019	Ag/V_2O_x/Ag/V_2O_x/n-c-Si/Al_2O_3/TiO_2/Mg/Al	0.618	27.1	79.5	13.3	[312]
2019	Ag/ITO/a-Si:H(p)/a-Si:H(i)/n-c-Si/a-Si:H(i)/TiO_x/Yb/Ag	0.732	33.8	78.6	19.2	[270]
2019	ITO/V_2O_5/n-SiNWs/TiO_2/Al	0.49	35.7	72.7	12.7	[313]
2019	Ag/ITO/MoO_x/n-c-Si/LiF_x/Al	0.563	34.35	72.18	13.96	[314]
2019	Ag/AZO NRs/AZO seed layer/p-c-Si/Al	0.529	30	39.38	6.25	[315]
2019	Ag/PEDOT:PSS/n-c-Si/TiO2/LiF_x/Al	0.626	31.9	75.6	15.1	[316]
2019	Ag/PEDOT:PSS/n-c-Si/MgO_x/Al	0.623	33.8	73.9	15.5	[317]
2019	Ag/ITO/CdS/n-c-Si/MoO_x/Ag	0.483	35.45	71.62	12.29	[318]
2019	Ag/ITO/a-Si:H(p)/a-Si:H(i)/n-c-Si/a-Si:H(i)/SiO_x/SnO_2/Mg/Al	0.695	37.71	71.11	18.6	[319]
2019	Ag/ITO/s-MoO_x/n-c-Si/Ti/Pd/Ag	0.465	30.92	56.6	8.13	[320]
2019	Ag/ITO/MoO_x/a-Si:H(i)/n-c-Si/a-Si:H(i)/a-Si:H(n)/ITO/Ag	0.724	36	74.1	19.3	[274]
2019	Ag/MoO_x/n-c-Si/LiF_x/Al	0.587	31.64	58.18	10.81	[321]
2019	Ag/SiN_x:H/n^+/p-c-Si/MoO_x/Ag	0.632	36.21	80.89	18.49	[322]
2019	Ag/ITO/NiO_x/SiO_x/n-c-Si/SiO_x/LiF_x/Al	0.58	36.9	71.06	15.2	[323]
2019	Ag/PEDOT:PSS/n-c-Si/SiO_x/EDTA-SnO_2/Ag	0.562	28.8	71.2	11.52	[324]
2019	Ag/ITO/MoO_3/n-c-Si/n^{++}/Al	0.572	33.9	66.5	12.89	[325]
2019	Ag/ITO/MoO_x/a-Si:H(i)/n-c-Si/a-Si:H(i)/TiO_x/Yb/Ag	0.65	33.9	73.7	16.3	[326]
2020	Ag/ITO/MoO_x/a-Si:H(i)/n-c-Si/a-Si:H(i)/a-Si:H(n)/ITO/Ag	0.734	39.15	81.77	23.48	[327]
2020	Ag/ITO/Cu_2O:B/n-c-Si/Ag	0.37	36.5	40.6	5.48	[328]
2020	Ag/ITO/a-Si:H(n)/a-Si:H(i)/n-c-Si/a-Si:H(i)/MoO_x/Ag	0.713	37.5	78.92	21.1	[329]
2020	Ag/ITO/a-Si:H(p)/a-Si:H(i)/n-c-Si/a-Si:H(i)/MgO/Al	0.687	33.8	72.4	16.8	[330]
2020	Ag/ITO/MoO_x/n-c-Si/LiF_x/Al	0.574	34.89	72.55	14.53	[331]
2020	Ag/PEDOT:PSS/n-c-Si/TiO_2/Ag/Al	0.616	28.5	70.9	13.08	[332]
2020	Ag/MoO_x/a-Si:H(i)/n-c-Si/a-Si:H(i)/LiF/Al	0.666	41.6	73.2	20.3	[333]
2020	Ag/SiN_x/n^+/p-c-Si/SiO_x/MoO_x/Ag	0.603	36.45	72.14	15.86	[334]
2020	Ag/ITO/WO_x/a-Si:H(i)/n-c-Si/a-Si:H(i)/a-Si:H(n)/Ag	0.66	35.91	56.07	13.29	[335]
2020	Al/AZO/nc-SiO_x:H(n)/a-Si:H(i)/n-c-Si/a-Si:H(i)/MoO_x/Ag	0.678	33.6	73.5	16.7	[336]
2020	Ag/SiN_x/n^+/p-c-Si/UV-SiO_x/MoO_x/V_2O_x/ITO/Ag	0.626	38.5	82.8	20	[337]
2020	Ag/ITO/a-Si:H(p)/a-Si:H(i)/n-c-Si/LPD-TiO_2/Al	0.6	31.5	77.8	14.7	[338]
2020	Ag/ITO/In_2S_3/p-c-Si/MoO_x/Ag	0.461	36.93	62.94	10.72	[339]
2020	Ag/ITO/a-Si:H(p)/a-Si:H(i)/n-c-Si/a-Si:H(i)/ZnO/LiF_x/ITO/Al	0.727	37.6	78	21.3	[340]
2021	Ag/ITO/MoO_3/a-Si:H(i)/n-c-Si/a-Si:H(i)/a-Si:H(n)/ITO/Ag	0.716	37.5	74.01	19.86	[252]
2021	Ag/ITO/MoO_x/SiO_x/MoS_2-QD/n-c-Si/a-Si:H(i)/a-Si:H(n)/ITO/Ag	0.697	40.8	80.2	22.8	[341]
2021	Ag/SiN_x:H/n^+/p-c-Si/MoO_x/Ag	0.622	38.8	79	19.19	[342]
2021	Ag/ITO/a-Si:H(n)/a-Si:H(i)/p-c-Si/a-Si:H(i)/MoO_x/ITO/Ag	0.636	35.62	78.53	17.89	[343]
2021	Ag/ITO/a-Si:H(n)/a-Si:H(i)/n-c-Si/a-Si:H(i)/Cu_2O(p)/ITO/Ag	0.584	36.8	63.8	13.7	[344]
2021	Ag/ITO/a-Si:H(p)/a-Si:H(i)/n-c-Si/SiO_y/TiO_x/Mg/Al	0.537	27.64	59.96	8.89	[345]

(*continued on next page*)

Table 2 (*continued*)

Publication time	Device structure	Voc (V)	Jsc (mA/cm^2)	FF (%)	PCE (%)	Ref
2021	Ag/ITO/s-V_2O_x/n-c-Si/Ti/Pd/Ag	0.556	33.86	57.14	10.75	[346]
2021	Ag/MoO_x-CNT/n-c-Si/Ag	0.5	30.6	58	8.8	[347]
2021	Ag/ITO/n-ZnS/p-c-Si/WO_3/Ag	0.529	33.55	61.17	10.86	[348]
2021	Ag/TCO/MoO_x/a-Si:H(i)/n-c-Si/a-Si:H(i)/a-Si:H(n)/TCO/Ag	0.7	39	75	22	[349]
2021	Ag/SiN_x:H/n+/p-c-Si/SiO_x/MoO_x/SiO_x/Ag	0.650	39.8	83.34	21.6	[350]
2021	Ag/ITO/a-Si:H(p)/a-Si:H(i)/p-c-Si/a-Si:H(i)/SnO_2/Mg/Al	0.718	36.2	77.3	20.1	[351]
2022	Ag/SnO_2 NSs/SnO_2 TF/p-c-Si/Ag	0.312	20.28	48.84	3.09	[352]
2022	Al/Ag/MoO_x/Ag/MoO_x/n-Si/MoO_x/Mg/Al	0.554	32.25	49.25	8.8	[353]
2022	Ag/ITO/MoO_x/n-Si/Al	0.36	35.15	31.85	4.03	[354]
2022	Ag+Al/TCO/MoO_x/a-Si:H(p)/a-Si:H(i)/n-c-Si/a-Si:H(i)/a-Si:H(n)/TCO/Al	0.711	32.8	74.9	17.5	[355]
2022	Al/RbF_x/SiN_x/TiO_x/a-Si:H(i)/n-c-Si/a-Si:H(i)/MoO_x/Ag	0.709	40.5	79.6	22.9	[356]
2022	Ag/ITO/MoO_x/a-Si:H(i)/n-c-Si/a-Si:H(i)/a-Si:H(n)/ITO/Ag	0.708	37.38	74.59	19.75	[357]
2022	Au/rGO:ZnO-NRs/ZnO/p-c-Si/Al	0.357	6.67	55.2	14.12	[358]
2022	Cu/MgF_2/IWO/MoO_x/PTB/c-Si(n)/a-Si:H(i)/a-Si:H(n)/IWO/Ag	0.721	40.2	82.18	23.83	[359]
2023	Ag/SiN_x/n+/p-c-Si/$MoO_{(3-x)}$:Nb/Ag	0.615	39.68	75.344	18.37	[360]
2023	Ag/PEDOT:PSS/V_2O_x/n-c-Si	0.593	29.97	71.12	12.64	[361]
2023	Ag/ITO/$MoO_{(3-x)}$/n-c-Si/Al/Ag	0.517	39.43	49.6	10.17	[362]
2023	Ag/ITO/MoO_x/MoS_2-QDs/n-c-Si/a-Si:H(i)/a-Si:H(n)/ITO/Ag	0.698	40.8	81.1	23	[363]
2023	Ag/SiN_x/n+ layer/p-c-Si/V_2O_5/Ag	0.597	39.66	72.84	17.23	[364]
2023	Ag+Al/AZO:Me/a-Si:H(i)/n-c-Si/a-Si:H(i)/a-Si:H(p)/ITO/Ag	0.693	39.8	71	19.58	[365]
2023	Au/MoO_x + $SnCl_2$@SWCNTs/n-c-Si/Au	0.26	108	29	8.20	[366]
2023	Ag/SiN_x/n+/p-c-Si/Ta_2O_5/Ag	0.612	39.64	76.24	18.47	[367]
2023	p-Si/SiO_x(FGA)/L-MoO_x/Ag	0.633	40.47	84.38	21.75	[368]
2023	Ag/ITO/AZO/MoO_x/a-Si:H(i)/n-c-Si	0.73	41.29	77.4	23.32	[369]
2024	Ag/SiN_x:Al_2O_3(p)/n-Si/BaO_xF_y/LiF/Ca:Al/Al	0.626	39.2	83.5	20.5	[370]

performance is still comparatively low[254,374].

Although metal halides as selective layers are promising in low contact resistivity, their stability is an issue[22]. Many metal halides lack stability in air and demand uninterrupted metallization processes without vacuum interruption, restricting their viability for large-scale production. Considering this, metal nitrides emerge as an alternative, given their extensive application as copper diffusion barriers in microelectronics and as photoanodes for photo-electrochemical water splitting, boasting high stability and conductivity[387,388]. In 2018, tantalum nitride (TaN_x) deposited via ALD was reported for the first time as the ETL[389]. As a result, their device achieved a PCE of 20.1 % with moderate surface passivation and a low ρ_c. In 2019, TiN_x was first reported as the ETL, offering a low ρ_c of 16.4 mΩ•cm^2 and a manageable J_0 of approximately 500 fA/cm^2[378]. Combined with SiO_x as the passivation layer, their device achieved a PCE of 20 % with a simplified fabrication process and reduced cost. Currently, the number of investigations into metal nitrides as selective layers is still low. Further exploration of other transition metal nitrides, such as zirconium nitride (ZrN_x), hafnium nitride (HfN_x), and molybdenum nitride (MoN_x) could prove to be promising avenues for research. Moreover, a few studies also presented that metal carbonates including K_2CO_3, Rb_2CO_3, Cs_2CO_3, $CaCO_3$, $SrCO_3$ and $BaCO_3$, can be used as ETLs in solar cells[390–392]. Combined with VO_x as the HTL, the proof-of-concept DASH solar cell using Cs_2CO_3 as the ETL can achieve a PCE of 16.59 %, exhibiting a promising prospect[286]. Furthermore, other metal compounds such as CdS, ZnS, and GaP also show potential for application as the ETL [393–395]. However, their device performance lags far behind.

As summarized in Table 3, the use of other metal compounds as the dopant-free selective layer in HJT solar cells has garnered increasing research interest in recent years. While a few of them have already demonstrated considerable device performance, further systematic studies are needed in this area. There is still a vast family of metal compounds that can be explored to deliver better device performance in HJT solar cells, such as ternary and quaternary species[396,397].

4.2.3. Organic materials

Organic molecules present another category of materials viable for dopant-free selective layers in HJT solar cells. They offer simplicity in fabrication and a wide array of options due to their versatility in modifying functional groups[50]. Some organic materials exhibiting electron selectivity are C60, PCBM, N2200, poly(ethylene oxide) (PEO), pyrrolidine tris-acid (CPTA), polyethylenimine (PEI), 8-hydroxyquinolinolato lithium (Liq), and SAMs[417–422]. Sun and co-workers reported PCEs of 13.7 % and 14.9 % for using PCBM and N2200 as the ETL in HJT solar cells, respectively[423]. Their findings revealed that the interaction between c-Si and organic materials plays a pivotal role in achieving efficient charge collection. The molecular structure was observed to influence the physical distance between silicon and organic materials. The shorter distance between PCBM and c-Si facilitates a higher charge transfer rate. This increased rate contributes to the formation of a more robust rear surface field effect, thereby reducing surface recombination. In another study, they further altered the N2200 molecule to F-N2200 by replacing a hydrogen atom with a fluorine atom[424]. This substitution led to a reduced physical distance and denser intermolecular stacking between the organic materials and c-Si. Consequently, the solar cells based on F-N2200 achieved a higher PCE compared to those based on N2200. He and co-workers reported two narrow-bandgap conjugated polymers, PTB7-NBr and PTB7-NSO_3, as ETLs with different functional groups[425]. As a result, the electrical properties of PTB7-NBr resulted in a lower contact resistance of 6.7 ± 0.8 mΩ·cm^2 compared to PTB7-NSO_3 (50 ± 25 mΩ·cm^2), showing better device performance. Ye and co-workers reported the use of poly(ethylene oxide) (PEO) as ETL between the c-Si and electrodes. The presence of an interface dipole generated by PEO expanded the built-in voltage (V_{bi}), leading to the achievement of a PCE of 12.3 %[420]. It is noteworthy that, among these organic ETLs, the device incorporating PEI achieved one of the highest PCEs, reaching 19.5 %[421]. Furthermore, self-assembled monolayers (SAMs) have emerged as promising alternatives to conventional charge-selective contacts in the perovskite research community[426]. Typically, a SAM comprises three components: an anchoring group, a spacer (or bridge), and a functional group. The combination of these constituents enables the customization of molecule design to align with the energy levels, charge mobility, and wettability required for optimal performance in photovoltaic devices[427,428]. SAMs organize into ordered arrays that, based on their structure, exhibit a dipole moment capable of modulating the work function of the substrate, thereby facilitating charge extraction at the interfaces[429,430]. Most recently, in a pioneering study, Stefaan and co-workers introduced n-PACz SAMs, featuring carbazole and phosphonic acid groups, as potential candidates for use as ETLs in HJT solar cells[431]. By introducing 2PACz between amorphous silicon-passivated c-Si and Al, they achieved an electron-selective contact with a carrier lifetime of 4.4 ms, iV_{oc} of

Table 3
Summary of device performance using other metal compounds as selective contacts in chronological order.

Publication time	Device structure	Voc (V)	Jsc (mA/cm2)	FF (%)	PCE (%)	Ref
2013	Al/AZO/ZnS/p-c-Si/Al	0.319	29.11	39.31	3.66	[398]
2013	Al/AZO/ZnS/p-c-Si/Al	0.279	23.83	4.79	2.72	[394]
2013	In/SnSe/n-c-Si/Al	0.425	17.23	44	6.44	[399]
2014	Al/MoS_2/p-c-Si/Cr/Ag	0.41	22.36	57.26	5.23	[400]
2016	Ti/Ag/ITO/CdS/n-c-Si/Al	0.308	13.92	42.7	1.83	[401]
2017	ITO/a-Si:H(p)/p-$BaSi_2$/n-c-Si/Al	0.47	35.8	60	9.9	[402]
2017	Ag/HAZO/n-ZnS/p-c-Si/Al	0.517	31.05	55	8.83	[403]
2018	Ag/ITO/$BaSi_2$/n-c-Si/Al	0.47	35.8	60	9.9	[404]
2018	Ag/ITO/MoO_x/n-c-Si/a-Si:H(n)/GaP/ITO/Ag	0.598	34.3	69	14.1	[299]
2018	Ag/ITO/ZnS/p-c-Si/WO3/Ag	0.525	33.75	61.73	10.94	[301]
2018	Ag/ITO/a-Si:H (p)/a-Si:H(i)/p-c-Si/n^+/GaP/ITO/Ag	0.616	31.3	61	11.8	[405]
2019	Ag/PEDOT:PSS/n-c-Si/$Ba(OH)_2$/Ag/Al	0.64	38.5	74	18.2	[406]
2019	Ag/ITO/CdS/n-c-Si/MoO_x/Ag	0.483	35.45	71.62	12.29	[318]
2019	Ag/ITO/MoS_2/a-Si:H(i)/p-c-Si/a-Si:H(i)/μc-SiO_x:H(p)/ITO/Ag	0.222	31.13	54.35	3.76	[407]
2020	Cr/Pd/Ag/Al_2O_3/SiN_x/p^+/n-c-Si/TiN/Al/Ag	0.607	38.7	80.1	18.7	[408]
2020	Ag/ITO/MoO_x/MoS_2/a-Si:H(i)/n-c-Si/a-Si:H(i)/μc-SiO_x:H(n)/ITO/Ag	0.288	31.25	60.72	5.47	[409]
2021	Ag/SiN_x/Al_2O_3/p^+/n-c-Si/a-Si:H(i)/LiAc/Ag	0.644	39	79	19.8	[410]
2021	Ag/ITO/n-ZnS/p-c-Si/WO_3/Ag	0.529	33.55	61.17	10.86	[348]
2021	Ag/ITO/a-Si:H (p)/a-Si:H(i)/n-c-Si/a-Si:H(i)/LiF_x/ITO/Ag	0.69	33.32	74.62	17.16	[411]
2022	Au/ZnO·SnO_2/p-c-Si/CuSCN/Au	0.592	19.54	35.43	4.1	[412]
2022	Ag/ITO/a-SiNx:H/a-Si:H(i)/n-c-Si/a-Si:H(i)/LiF/Ti/Al	0.717	41.83	78.68	23.61	[413]
2023	Ag/ITO/a-Si:H (p)/a-Si:H(i)/n-c-Si/a-Si:H(i)/LiF/Ti/Al	0.716	38.35	80.65	22.14	[414]
2023	Ag/SiN_x/MoS_2/SiO_x/n-Si/p-c-Si/Al	0.602	35.43	67.89	14.6	[415]
2023	Ag/SiN_x/a-Si:H (n)/c-Si(p)/Al^{3+}-I_2:CuI/Ag	0.619	39.7	74.28	18.28	[416]

729 mV and a contact resistivity of 65 mΩ·cm^2, resulting in a PCE of 21.4 % with a V_{oc} of 725 mV and a FF of 79.2 %.On the other hand, organic materials such as PEDOT:PSS, P3HT, and TAPC have been studied as HTLs, with PEDOT:PSS being the most extensively researched [95]. As shown in Fig. 5e, PEDOT:PSS is a hole-conducting polymer wherein the conductive constituents of PEDOT are effectively dispersed within the water-soluble insulating polymer matrix of PSS[432]. The PEDOT molecule, with a molecular weight (MW) of approximately 1–2.5 kDa, is hydrophobic, whereas the PSS molecule (MW ~400 kDa) is hydrophilic. These molecules adhere to each other through Coulomb attraction, forming PEDOT:PSS molecules[255]. As HTL in HJT solar cells, the conductivity of PEDOT:PSS significantly influences the device performance. The pristine PEDOT:PSS solution exhibits a conductivity below 1 S cm^{-1}, which can be enhanced to approximately 1000 S cm^{-1} through the addition of cosolvents such as dimethyl sulfoxide (DMSO) or ethylene glycol (EG). Furthermore, secondary treatment methods can further increase the conductivity of PEDOT:PSS to several thousand S cm^{-1} by separating the conductive PEDOT from the insulating PSS component[433–436]. For instance, Shirai and co-workers demonstrated that the addition of p-toluenesulfonic acid to PEDOT:PSS promotes phase separation between PEDOT and PSS, leading to enhanced conductivity of the PEDOT:PSS film[433]. Consequently, the PCE of HJT solar cells improved from 12 % to 14 %. Leung and co-workers integrated silver nanowires into the PEDOT:PSS film, which significantly reduced the sheet resistance of the film and boosted the PCE of the HJT solar cell to 15 %[437]. In addition to the conductivity, the WF of PEDOT:PSS also affects the device performance of HJT solar cells. As reported, there are typically two methods to enhance the WF of PEDOT:PSS films, including modifying the PEDOT:PSS solution by incorporating foreign materials and depositing high-WF materials onto the PEDOT:PSS film as bilayer[285,438–440]. Sun and co-workers added perfluorinated ionomer (PFI) into the PEDOT:PSS film, which increased the WF of the film by 0.2 eV, resulting in a PCE enhancement by about 20 %[441]. In another investigation, they found that the deposition of an organic molecule, 1,4,5,8,9,11-hexaazatriphenylene hexacarbonitrile (HAT-CN), onto PEDOT:PSS films increased the work function of PEDOT:PSS from 5.0 eV to 5.4 eV. [G7–361] Sturm and co-workers inserted P3HT film between Si and PEDOT:PSS. This integration served to impede the transfer of electrons to the PEDOT:PSS film, effectively reducing the dark current[442]. On the other hand, Yu and co-workers introduced an organic compound known as 1,1-bis[(di-4-tolylamino)phenyl]cyclohexane (TAPC) between Si and PEDOT:PSS. This resulted in an enhancement of carrier lifetime, leading to an improved PCE of 13 %[443]. Likewise, the insertion of an electron-blocking material, N,N'-bis(3-methylphenyl)-N,N'-diphenylbenzidine, between Si and PEDOT:PSS demonstrated similar effects to those observed with P3HT or TAPC[444]. To date, the highest reported PCE for HJT solar cells based on PEDOT:PSS is 20.6 % by Zielke and co-workers, attributed to the use of modified PEDOT:PSS dispersion and optimal pre-treated c-Si surfaces[445].

As summarized in Table 4, significant advancements have been achieved in selective layers based on organic materials for HJT solar cells. So far, there is a disagreement about the balance between sophisticated methods like atomic layer deposition (ALD) for creating high-quality passivation layers versus simpler, more scalable techniques (e.g., sputtering or chemical vapor deposition) that might be less effective but easier for mass production. Given that many organic selective layers can be produced using straightforward solution-based or evaporation techniques, this suggests a cost-effective pathway for HJT solar cell fabrication. However, the issue of device stability remains unresolved. According to current research findings, degradation can be attributed to the inherent instability of organic materials and contact interfaces. Unlike conventional Si solar cells, which typically offer a twenty-five-year guarantee in commercial production, organic materials are more susceptible to environmental factors such as heat, light, moisture, and oxygen. For instance, PEDOT:PSS films are notably

Table 4
Summary of device performance using organic materials as selective contacts in chronological order.

Publication time	Device structure	Voc (V)	Jsc (mA/cm2)	FF (%)	PCE (%)	Ref
2008	Au/DOPNA/p-c-Si/Al	0.29	4.83	33	5.74	[447]
2012	Ag/PEDOT:PSS/P3HT/n-c-Si/Al	0.4	30	48	6.3	[448]
2012	Ag/PEDOT:PSS+Zonly/n-c-Si/Al	0.541	29.2	71.8	11.34	[449]
2012	Ag/GO/PEDOT:PSS/n-c-Si/Al	0.52	27.99	0.63	9.27	[450]
2012	Ag/PEDOT:PSS:GO/n-c-Si/Al	0.548	28.9	67.5	10.7	[451]
2013	Ag/PEDOT:PSS:MeOH:EG/n-c-Si/Al	0.548	28.79	71.1	11.23	[452]
2013	Ag/PEDOT:PSS/TAPC/n-c-Si/Al	0.54	34.81	67.08	12.54	[453]
2014	SiN_x/Al/Al_2O_3/n^+/n-c-Si/SiO_x/PEDOT:PSS/Al	0.668	41.1	83	22.8	[454]
2014	Ag/MoO_3/PEDOT:PSS/n-c-Si/Liq/Al	0.63	29.2	74.9	13.8	[285]
2014	Ag/PEDOT:PSS/SiO_x/n-c-Si/Ti/Ag	0.5	33.74	64.73	11	[455]
2015	GO/AgNWs/PEDOT:PSS/n-c-Si/Al	0.601	28.4	78.4	13.3	[456]
2015	Ag/PEDOT:PSS/n-c-Si/n^+/Ag	0.564	32.1	75.2	13.63	[457]
2015	TiO_2/Ag/PEDOT:PSS/n-c-Si/InGa	0.62	34.3	73	15.5	[433]
2016	Ag/PEDOT:PSS/n-c-Si/PFN/Al	0.582	29.57	77.56	13.35	[458]
2016	Al/C_{60}/p-c-Si/Al	0.5	25.09	67	8.4	[459]
2016	MoO_3/Ag/PEDOT:PSS/SiOx/n-c-Si/a-Si:H(i)/a-Si:H(n)/Al	0.532	34.9	66.97	12.43	[460]
2016	Ag/PEDOT:PSS/n-c-Si/InGa	0.53	35.6	67	12.5	[461]
2016	Ag/PEDOT:PSS/TAPC/p-PFO/n-c-Si/Al	0.553	32.41	70.13	12.56	[462]
2016	Ag/GOPs/PEDOT:PSS/n-c-Si/Al	0.64	30.2	72.8	14.1	[463]
2016	Ag/PEDOT:PSS/n-c-Si/PEO/Al	0.563	28.65	76.22	12.29	[420]
2016	Ag/Nafion/PEDOT:PSS/n-c-Si/InGa	0.604	32.7	70.6	14	[464]
2016	Cu/PEDOT:PSS/n-c-Si/Al	0.49	34	59	9.1	[465]
2016	Ag/PEDOT:PSS/n-c-Si/Al	0.58	28.57	69.2	11.46	[466]
2016	Ag/PEDOT:PSS+Au NP/n-c-Si/Al	0.622	27.7	74.6	12.85	[467]
2016	Glass/ITO/PEDOT:PSS/LPD-TiO_2/n-c-Si/Al	0.63	34.15	65	14.7	[468]
2016	CuI/Ag/PEDOT:PSS/SiO_x/n-c-Si/InGa	0.656	28	78.1	14.3	[373]
2016	Ag/PEDOT:PSS/n-c-Si/a-Si:H/a-SiC:H/Ti/Al	0.56	30.54	49.7	8.5	[469]
2016	Au/Graphene/GQDs/SiO_2/n-c-Si/InGa	0.58	33.93	63	12.35	[470]
2016	Ag/PEDOT:PSS/n-c-Si/n^+/Al	0.472	33.37	56.52	9.37	[471]
2017	Ag/PEDOT:PSS/n-c-Si/a-Si:H(i)/a-Si:H(n)/Al	0.634	35.4	72.22	16.21	[472]
2017	Ag/PEDOT:PSS/n-c-Si/TiO_x/Al	0.643	30.7	72.4	14.3	[288]
2017	Ag/DEP/PEDOT:PSS/n-c-Si/a-Si:H(i)/a-Si:H(n)/Al	0.634	36.5	70	16.2	[473]
2017	Ag/PEDOT:PSS/n-c-Si/F-N2200/Al	0.635	31.1	73.3	14.5	[424]
2017	Ag/PEDOT:PSS/n-c-Si/PCBM/Al	0.646	31.37	74.25	14.9	[423]
2017	Ag/PEDOT:PSS-CNPs/n-c-Si/Al	0.614	26.34	73.93	11.95	[474]
2017	Ag/PEDOT:PSS/P(VDF-TrFE)/n-c-Si/Ti/Au	0.583	30.8	65.4	11.73	[475]
2017	Ag/PEDOT:PSS/SiO_x/n-c-Si/a-Si:H(i)/a-Si:H(n)/ITO/Ti/Ag	0.663	31.9	70	14.8	[476]
2017	Ag/PEDOT:PSS/n-c-Si/TiO_2/Al	0.62	31	75.96	14.6	[294]
2017	CuI/Ag/PEDOT:PSS/n-c-Si/PTB7-NBr/Al	0.638	32.8	76.5	16	[425]
2018	Ag/AgNW/PEDOT:PSS/n-c-Si/Al	0.56	27.07	72.15	11.07	[477]
2018	Ag/SiNx/a-Si:H(n)/p-c-Si/PEDOT:PSS/Ag	0.656	38.7	79	20.2	[478]
2018	Ag/PEDOT:PSS/n-c-Si/AZO/Al	0.641	27.6	78	13.6	[298]
2018	Ag/PEDOT:PSS/n-c-Si/Al	0.628	28.9	74.5	13.6	[479]
2018	Ag/PEDOT:PSS/n-c-Si/SiO_x/Mg/Al	0.61	33.4	73.5	15	[480]
2018	Ag/PEDOT:PSS/SiO_x/n-c-Si/InGa	0.607	33.72	65.01	13.31	[481]
2018	Ag/HC-PEDOT:PSS/HW-PEDOT:PSS/n-c-Si/Ga-In	0.64	26.27	75.5	12.69	[482]
2017	TAPC/Ag/PEDOT:PSS/n-c-Si/Ag/$Ba(OH)_2$/Al	0.623	27.4	73.3	12.5	[483]
2018	Au/MnTPPCl/n-c-Si/Al	0.438	6.28	33.6	4.62	[484]
2018	Ag/HC-PEDOT:PSS/HA-PEDOT:PSS/n-c-Si/CPTA/Al	0.632	34.7	76.3	16.73	[417]
2018	Ag/AgNW/PEDOT:PSS/SiO_x/n-c-Si/Al	0.622	31.05	78	15.1	[437]
2018	Ag/PEDOT:PSS/n-c-Si/QH/Al	0.635	27.16	77.07	13.29	[485]
2018	Ag/PEDOT:PSS/n-c-Si/rubrene:DMSO/Ag	0.609	28.2	69.1	11.9	[486]
2018	Ag/PEDOT:PSS/n-c-Si/SnO_2/Ag	0.593	33.16	72	14.16	[309]
2018	Ag/PEDOT:PSS/n-c-Si/a-Si:H(i)/Li-ZnO/Al	0.623	33.58	72.38	15.14	[311]
2019	Ag/IWO/a-Si:H(n)/a-Si:H(i)/n-c-Si/PEDOT:PSS/Ag	0.633	36.6	70.2	16.3	[487]
2019	Ag/PEDOT:PSS/n-c-Si/MgO_x/Al	0.623	33.8	73.9	15.5	[317]
2019	Ag/PEDOT:PSS/n-c-Si/TiO_2/LiF_x/Al	0.626	31.9	75.6	15.1	[316]
2019	Ag/PEDOT:PSS/n-c-Si/SiO_x/EDTA-SnO_2/Ag	0.562	28.8	71.2	11.52	[324]
2019	Al/SiN_x/AlO_x/p-c-Si/PEDOT:PSS/Ag	0.66	38.5	80	20.4	[488]
2020	Ag/PEDOT:PSS/n-c-Si/TiO_2/Ag/Al	0.616	28.5	70.9	13.08	[332]
2020	Ag/SiO_x/F-SWCNT/n-c-Si/InGa	0.599	31.2	70.9	13.3	[489]
2020	Ag/ITO/a-Si:H(p)/a-Si:H(i)/n-c-Si/a-Si:H(i)/b-PEI/Al	0.72	37	72.9	19.4	[418]
2020	Ag/PEDOT:PSS/n-c-Si/PCBM/Al	0.618	31.75	66.49	13.12	[490]
2020	Al/Graphene/nc-SiO_x(p)/a-Si:H(i)/n-c-Si/a-Si:H(i)/nc-SiO_x(n)/AZO/Al	0.612	25.3	55.8	8.65	[491]
2020	Ag/PEDOT:PSS-MoO_x/n-c-Si/PC_{61}BM/Al	0.627	32.41	68.01	13.82	[492]
2020	Ag/PEDOT:PSS-CNT/n-c-Si/Al	0.589	25.3	60.79	9.05	[493]
2021	Ag/PEDOT:PSS/SiNWs/n-c-Si/PCBM/Mg/Al	0.65	34.8	80.1	18.12	[494]
2021	Ag/PEDOT:PSS+ITO-NPs/n-c-Si/InGa	0.589	33.66	60.54	12.01	[495]
2021	Au/TTBTP/n-c-Si/Al	0.68	8.06	43.3	2.38	[496]
2021	Ag/PEDOT:PSS+GOPs/n-c-Si/TiN/Al	0.66	33	69.03	15.01	[497]
2021	Ag/PEDOT:PSS/n-c-Si/Al	0.521	32.1	66.2	11.1	[498]
2021	Ag/PEDOT:PSS/MWCNTs&PDA/n-c-Si/PC_{61}BM/Al	0.637	34.76	56.41	12.49	[499]
2021	Ag/GO/PEDOT:PSS/n-c-Si/In:Ga	0.648	28.89	73.5	13.76	[500]
2022	Ag/HQ-PEDOT:PSS/BQ/n-c-Si/LiF/Al	0.618	27.7	61.8	10.6	[501]

(*continued on next page*)

Table 4 (*continued*)

Publication time	Device structure	Voc (V)	Jsc (mA/cm2)	FF (%)	PCE (%)	Ref
2021	Au/PEDOT:PSS/n-c-Si/In-Ga	0.515	24.16	44.12	5.49	[502]
2021	Ag/PEDOT:PSS/n-Si/$PC_{61}BM$/Al	0.645	32.81	63.56	13.44	[503]
2022	Ag/PEDOT:(PSS+IBTEO)/n-c-SiNWs/PCBM/Mg/Al	0.649	34.8	80.5	18.2	[504]
2022	Ag/(P/Se-WO_x):(PEDOT:PSS)/n-c-Si/$PC_{61}BM$/Al	0.633	33.51	6564	13.64	[505]
2022	Ag/ITO/a-Si:H(n)/a-Si:H(i)/n-c-Si/GO:Nafion/Ag	0.670	40	80.6	21.6	[506]
2022	Al/MoS_2/h-BN/p-c-Si/Ag	0.61	32.2	62	11.83	[507]
2022	Ag/ITO/a–Si:H(n)/a–Si:H(i)/n-c-Si/MXene:Nafion/eAg	0.556	38.64	66.18	14.21	[508]
2023	Ag/doped-PEDOT:PSS/n-c-Si/Al	0.64	33.88	64.33	14.46	[509]
2023	Ag/TsOH-SWCNT/SiO_x/n-c-Si/In/Ga	0.623	35.5	80	17.7	[510]
2023	Ag/ITO/V_2O_5/n-c-Si/PAMAM/Al	0.6	31.7	76.2	14.5	[511]
2023	Ag/PEDOT:PSS/V_2O_x/n-c-Si	0.593	29.97	71.12	12.64	[361]
2023	Ag/PEDOT:PSS/n-c-Si/Al	0.497	7.71	67.8	5.53	[512]
2023	Ag/PEDOT:PSS/p-c-Si/ZnO/Ag	0.56	25.99	67.1	9.77	[513]
2023	Ag/PEDOT:PSS/SiO_x/n-c-Si/In:Ga	0.522	28.75	69.45	10.42	[514]
2023	Ag/PEDOT:PSS/PEDOT:PSS-Nafion/n-c-Si/In:Ga	0.69	29.65	70.77	12.33	[515]
2023	Ag/PEDOT:PSS/n-c-Si/In:Ga	0.556	24.26	65.87	8.89	[516]
2023	Al/2PACz/a-Si:H(i)/c-Si(n)/a-Si:H(i)/a-Si:H(p)/ITO/Ag grid	0.725	37.3	79.2	21.4	[431]
2024	Ag/PEDOT:PSS-Nafion/PEDOT:PSS-TX/n-Si/SiO_2/n^+-poly-Si/Ag	0.636	31.1	69.1	13.7	[517]
2024	Ag/PEDOT:PSS/n-Si/In:Ga	0.541	32.13	61.96	10.78	[518]

vulnerable to degradation from UV light and oxygen exposure[446]. When exposed to oxygen, sulfur atoms within the thiophene rings transform into insulating sulfoxide and sulfone structures. This oxidation process is expedited by UV light, exacerbating the degradation. As a result, the increased resistivity of the film imposes limitations on device efficiency. Further research dedicated to investigating the stability of organic materials in this domain is warranted.

5. Conclusion

In conclusion, HJT solar cells represent a promising avenue for overcoming the limitations of homojunction SSCs, such as high carrier recombination at the rear surface and the need for heavy bulk doping, to get us closer to the fundamental efficiency limit of silicon solar cells. By incorporating passivating selective contacts on both sides of the c-Si wafer, HJT technology offers improved surface passivation and reduced recombination rates, leading to higher V_{oc} and enhanced PCE. Recent advancements in passivating selective contacts for HJT SSCs have shown remarkable progress, as evidenced by the increasing number of publications and the steady improvement in PCE. Innovative approaches, such as the a-SiO_x:H(i) passivation layers, DASH structure, and the integration of SAMs, have broadened the scope of materials available for passivating selective contacts. The comprehensive survey presented in this paper provides valuable insights into the fundamental mechanisms, material modifications, and performance evaluations of passivating selective contacts for HJT SSCs. By systematically exploring the evolution of selective layers and highlighting recent advancements, this study contributes to the ongoing development of HJT technology.

Herein, in the context of passivating selective contacts in HJT solar cells, we also outline current challenges in the field and possible directions for future research:

1) Addressing the instability of passivating selective contacts and their compatibility with adjacent layers is crucial for advancing solar cell technology. This issue often arises due to interfacial reactions or processing constraints that can compromise device performance and longevity. For newly developed selective layers, such as those based on TMOs and organic materials, while they show promise for high PCE, there is a pressing need for comprehensive evaluations of their long-term stability. These materials can be sensitive to environmental factors, which can lead to degradation over time. To mitigate the risk of air contamination, which can adversely affect these sensitive materials, it is essential to employ thin-film deposition techniques that operate in controlled, inert environments. Moreover, incorporating interlayers that have demonstrated both thermodynamic stability and suitable band alignment can help address compatibility issues. These interlayers act as buffers, preventing undesirable reactions between the passivating layers and adjacent layers. They also ensure proper charge transport and minimize energy losses at interfaces [50].
2) There remains a critical need to develop passivating selective contacts with optimized electronic properties to enhance the performance of solar cells. Specifically, the challenge lies in achieving sufficiently low EA for the electron-selective contact and high WF for the hole-selective contact. These properties are essential for ensuring efficient charge separation and collection at the respective electrodes. To address these challenges, advanced doping strategies are one promising approach. Doping can modify the electronic properties of the materials, potentially lowering the EA for electron-selective contacts or increasing the WF for hole-selective contacts. This involves introducing dopants that can fine-tune the energy levels within the material to better match the requirements for efficient charge extraction. Another approach is the chemical potential tuning of relevant elements, such as oxygen. By adjusting the concentration of these elements or their chemical states within the contact materials, it is possible to optimize the electronic band structure and improve the contact properties. This strategy may involve sophisticated techniques such as controlled oxidation or alloying, which require further development to fully realize their potential. In addition to these strategies, the exploration of new materials is crucial. Ternary and quaternary metal compounds offer a rich field of possibilities, as their complex compositions can provide tailored band alignments and high electrical conductivities. For example, materials combining multiple metal elements may exhibit synergistic effects that enhance their electronic properties beyond those of binary compounds. To fully leverage these advanced materials, more in-depth investigation is needed. This includes studying their fundamental properties, processing techniques, and interactions with other layers in the solar cell structure. Comprehensive research into these materials could lead to the discovery of new candidates that offer improved performance and stability. Overall, continued development in these areas—advanced doping techniques, chemical potential tuning, and exploration of complex metal compounds—will be essential for achieving optimal passivating selective contacts. These advancements will contribute to higher efficiency and more reliable solar cell technologies, addressing some of the current limitations in the field.
3) A thorough understanding of the charge transport mechanism in passivating selective contacts is still lacking, which limits the optimization of these materials for high-performance solar cells. For example, selective materials such as lithium fluoride (LiFx) are known for their promising passivating properties. However, the

mechanism by which carriers traverse through such materials—especially when the material thickness exceeds 10 nm—is not yet fully understood[381]. In particular, the role of tunneling in these processes remains unclear and requires more detailed investigation. The current theoretical models, including those that involve tunneling, often fall short of explaining how carriers can effectively move through thicker layers of these materials. Tunneling mechanisms, while useful for very thin layers, may not fully account for the observed behavior in thicker films. This discrepancy suggests that additional factors or mechanisms might be at play that have not been fully accounted for in existing models. Therefore, it is crucial to conduct a meticulous examination of carrier transport mechanisms under various conditions to bridge this knowledge gap. This includes studying how different factors, such as material thickness, temperature, and applied electric fields, influence carrier movement. Advanced experimental techniques, such as time-resolved spectroscopy or depth-resolved measurements, could provide insights into the dynamics of carrier transport in these materials. By gaining a deeper understanding of these mechanisms, researchers can better exploit the intrinsic properties of passivating selective materials. This knowledge will enable the design of innovative contact structures that optimize carrier selectivity and enhance overall device performance. For instance, insights into how carriers navigate through different thicknesses of passivating layers could lead to the development of multilayer structures that improve charge extraction efficiency and minimize losses. In summary, advancing our comprehension of charge transport mechanisms is essential for pushing the boundaries of passivating selective contact technology. By exploring new theoretical and experimental approaches, we can unlock the full potential of these materials.

Given these ongoing advancements, the potential for HJT solar cells to surpass a PCE of 28 % is within reach. Continued research and development in passivating selective contacts will be instrumental in achieving this milestone. By addressing current limitations and leveraging new technologies, researchers and manufacturers are poised to significantly improve the efficiency and performance of HJT solar cells, making them a leading choice for high-performance photovoltaic applications.

CRediT authorship contribution statement

Tingshu Shi: Writing – review & editing, Writing – original draft, Methodology, Investigation, Data curation, Conceptualization. **Yu Zhang:** Writing – review & editing, Writing – original draft, Visualization, Validation, Supervision, Software, Resources, Project administration, Methodology, Investigation, Formal analysis, Data curation, Conceptualization. **Hoex Bram:** Writing – review & editing, Writing – original draft, Visualization, Validation, Supervision. **Leiping Duan:** Writing – review & editing, Writing – original draft, Visualization, Validation, Methodology, Data curation. **Zeguo Tang:** Writing – review & editing, Writing – original draft, Supervision, Investigation, Funding acquisition.

Declaration of Competing Interest

The authors declare no conflict of interest.

Data availability

Data will be made available on request.

Acknowledgement

This work has been supported by the National Key Research and Development Programs—Intergovernmental International Cooperation in Science and Technology Innovation Project (grant No. 2022YFE0118400), Natural Science Foundation of Top Talent of SZTU (No. GDRC202111), and Shenzhen Key Laboratory of Applied Technologies of Super-Diamond and Functional Crystals (ZDSYS20230626091303007).

References

[1] H. Yang, R. Deshmukh, S. Suh, Global transcontinental power pools for low-carbon electricity, Nat. Commun. 14 (2023) 8350, https://doi.org/10.1038/s41467-023-43723-z.
[2] H. Liang, F. You, Reshoring silicon photovoltaics manufacturing contributes to decarbonization and climate change mitigation, Nat. Commun. 14 (2023) 1274, https://doi.org/10.1038/s41467-023-36827-z.
[3] L. Liu, G. He, M. Wu, G. Liu, H. Zhang, Y. Chen, J. Shen, S. Li, Climate change impacts on planned supply–demand match in global wind and solar energy systems, Nat. Energy 8 (2023) 870–880, https://doi.org/10.1038/s41560-023-01304-w.
[4] L. Kruitwagen, K.T. Story, J. Friedrich, L. Byers, S. Skillman, C. Hepburn, A global inventory of photovoltaic solar energy generating units, Nature 598 (2021) 604–610, https://doi.org/10.1038/s41586-021-03957-7.
[5] International Technology Roadmap for Photovoltaic (ITRPV) 14th Edition, ⟨https://www.vdma.org/international-technology-roadmap-photovoltaic⟩, 2023.
[6] J.P. Helveston, G. He, M.R. Davidson, Quantifying the cost savings of global solar photovoltaic supply chains, Nature 612 (2022) 83–87, https://doi.org/10.1038/s41586-022-05316-6.
[7] S. Chu, A. Majumdar, Opportunities and challenges for a sustainable energy future, Nature 488 (2012) 294–303, https://doi.org/10.1038/nature11475.
[8] C. Ballif, F.-J. Haug, M. Boccard, P.J. Verlinden, G. Hahn, Status and perspectives of crystalline silicon photovoltaics in research and industry, Nat. Rev. Mater. 7 (2022) 597–616, https://doi.org/10.1038/s41578-022-00423-2.
[9] Z. Sun, X. Chen, Y. He, J. Li, J. Wang, H. Yan, Y. Zhang, 2022, , Toward Efficiency Limits of Crystalline Silicon Solar Cells: Recent Progress in High-Efficiency Silicon Heterojunction Solar Cells 122200015 10.1002/aenm.202200015.
[10] B. Kafle, A. Richter, Tunnel oxide passivated contact (TOPCon) solar cells, Photovolt. Sol. Energy (2024) 55–69.
[11] Y. Fan, P. Han, P. Liang, Y. Xing, X. Mao, S. Hu, Investigation of the forming process and characteristics of Al-BSF in silicon solar cells, 2013 Int. Conf. Mater. Renew. Energy Environ. (2013) 57–61.
[12] N. Chen, A. Ebong, Towards 20% efficient industrial Al-BSF silicon solar cell with multiple busbars and fine gridlines, Sol. Energy Mater. Sol. Cells 146 (2016) 107–113, https://doi.org/10.1016/j.solmat.2015.11.020.
[13] A. Blakers, Development of the PERC Solar Cell, IEEE J. Photovolt. 9 (2019) 629–635, https://doi.org/10.1109/JPHOTOV.2019.2899460.
[14] J. Zhao, A. Wang, M.A. Green, 24·5% Efficiency silicon PERT cells on MCZ substrates and 24·7% efficiency PERL cells on FZ substrates, Prog. Photovolt.: Res. Appl. 7 (1999) 471–474, https://doi.org/10.1002/(SICI)1099-159X(199911/12)7:6<471::AID-PIP298>3.0.CO;2-7.
[15] T. Dullweber, M. Stöhr, C. Kruse, F. Haase, M. Rudolph, B. Beier, P. Jäger, V. Mertens, R. Peibst, R. Brendel, Evolutionary PERC+ solar cell efficiency projection towards 24% evaluating shadow-mask-deposited poly-Si fingers below the Ag front contact as next improvement step, Sol. Energy Mater. Sol. Cells 212 (2020) 110586, https://doi.org/10.1016/j.solmat.2020.110586.
[16] D.K. Ghosh, S. Bose, G. Das, S. Acharyya, A. Nandi, S. Mukhopadhyay, A. Sengupta, Fundamentals, present status and future perspective of TOPCon solar cells: a comprehensive review, Surf. Interfaces 30 (2022) 101917, https://doi.org/10.1016/j.surfin.2022.101917.
[17] H. Ullah, S. Czapp, S. Szultka, H. Tariq, U.B. Qasim, H. Imran, Crystalline Silicon (c-Si)-Based Tunnel Oxide Passivated Contact (TOPCon) Solar Cells: A Review, Energies 16 (2023), https://doi.org/10.3390/en16020715.
[18] S.W. Glunz, B. Steinhauser, J.-I. Polzin, C. Luderer, B. Grübel, T. Niewelt, A.M.O. M. Okasha, M. Bories, H. Nagel, K. Krieg, F. Feldmann, A. Richter, M. Bivour, M. Hermle, Silicon-based passivating contacts: the TOPCon route, Prog. Photovolt.: Res. Appl. 31 (2023) 341–359, https://doi.org/10.1002/pip.3522.
[19] M.J. Kerr, A. Cuevas, P. Campbell, Limiting efficiency of crystalline silicon solar cells due to Coulomb-enhanced Auger recombination, Prog. Photovolt.: Res. Appl. 11 (2003) 97–104, https://doi.org/10.1002/pip.464.
[20] R.B. Fair, The effect of strain-induced band-gap narrowing on high concentration phosphorus diffusion in silicon, J. Appl. Phys. 50 (2008) 860–868, https://doi.org/10.1063/1.326001.
[21] S. De Wolf, A. Descoeudres, Z.C. Holman, C. Ballif, 2012, , High-efficiency Silicon Heterojunction Solar Cells: A Review 27–24, 10.1515/green-2011-0018.
[22] Y. Liu, Y. Li, Y. Wu, G. Yang, L. Mazzarella, P. Procel-Moya, A.C. Tamboli, K. Weber, M. Boccard, O. Isabella, X. Yang, B. Sun, High-efficiency silicon heterojunction solar cells: materials, devices and applications, Mater. Sci. Eng.: R: Rep. 142 (2020) 100579, https://doi.org/10.1016/j.mser.2020.100579.
[23] W. Fuhs, K. Niemann, J. Stuke, Heterojunctions of amorphous silicon and silicon single crystals, AIP Conf. Proc. 20 (1974) 345–350, https://doi.org/10.1063/1.2945985.
[24] T. Sawada, N. Terada, S. Tsuge, T. Baba, T. Takahama, K. Wakisaka, S. Tsuda, S. Nakano, High-efficiency a-Si/c-Si heterojunction solar cell, Proc. 1994 IEEE 1st World Conf. Photovolt. Energy Convers. - WCPEC (A Jt. Conf. PVSC, PVSEC PSEC) vol.1212 (1994) 1219–1226.

[25] M. Taguchi, A. Terakawa, E. Maruyama, M. Tanaka, Obtaining a higher Voc in HIT cells, Prog. Photovolt.: Res. Appl. 13 (2005) 481–488, https://doi.org/10.1002/pip.646.

[26] J. Haschke, O. Dupré, M. Boccard, C. Ballif, Silicon heterojunction solar cells: recent technological development and practical aspects - from lab to industry, Sol. Energy Mater. Sol. Cells 187 (2018) 140–153, https://doi.org/10.1016/j.solmat.2018.07.018.

[27] N. Jensen, R.M. Hausner, R.B. Bergmann, J.H. Werner, U. Rau, Optimization and characterization of amorphous/crystalline silicon heterojunction solar cells, Prog. Photovolt.: Res. Appl. 10 (2002) 1–13, https://doi.org/10.1002/pip.398.

[28] K. Masuko, M. Shigematsu, T. Hashiguchi, D. Fujishima, M. Kai, N. Yoshimura, T. Yamaguchi, Y. Ichihashi, T. Mishima, N. Matsubara, T. Yamanishi, T. Takahama, M. Taguchi, E. Maruyama, S. Okamoto, Achievement of more than 25% conversion efficiency with crystalline silicon heterojunction solar cell, IEEE J. Photovolt. 4 (2014) 1433–1435, https://doi.org/10.1109/JPHOTOV.2014.2352151.

[29] C. Xing, C. Jiang, W. Gu, X. Lou, K. Gao, Y. Song, B. Shao, K. Li, X. Wang, D. Xu, X. Zhang, Y. Wang, X. Yang, B. Sun, SrFx-based electron-selective contact with high tolerance to thickness for crystalline silicon solar cells enabling efficiency over 21%, Prog. Photovolt.: Res. Appl. 32 (2024) 35–44, https://doi.org/10.1002/pip.3733.

[30] J. Ibarra Michel, J. Dréon, M. Boccard, J. Bullock, B. Macco, Carrier-selective contacts using metal compounds for crystalline silicon solar cells, Prog. Photovolt.: Res. Appl. 31 (2023) 380–413, https://doi.org/10.1002/pip.3552.

[31] Best Research-Cell Efficiency Chart, https://www.nrel.gov/pv/cell-efficiency.html, 2024.

[32] LONGi sets new world-record for silicon solar cell efficiency, Launching 2nd Generation Ultra-Efficient BC-Based Module, ⟨https://www.longi.com/en/news/longi-hi-mo9-bc-world-record/⟩, (accessed 08 May).

[33] W. Long, S. Yin, F. Peng, M. Yang, L. Fang, X. Ru, M. Qu, H. Lin, X. Xu, On the limiting efficiency for silicon heterojunction solar cells, Sol. Energy Mater. Sol. Cells 231 (2021) 111291, https://doi.org/10.1016/j.solmat.2021.111291.

[34] Q. Su, H. Lin, G. Wang, H. Tang, C. Xue, Z. Li, X. Xu, P. Gao, Theoretical limiting-efficiency assessment on advanced crystalline silicon solar cells with Auger ideality factor and wafer thickness modifications, Prog. Photovolt.: Res. Appl. N./a (2024), https://doi.org/10.1002/pip.3790.

[35] H. Lin, G. Wang, Q. Su, C. Han, C. Xue, S. Yin, L. Fang, X. Xu, P. Gao, Unveiling the mechanism of attaining high fill factor in silicon solar cells, Prog. Photovolt.: Res. Appl. 32 (2024) 359–371, https://doi.org/10.1002/pip.3775.

[36] W. Li, Z. Xu, Y. Yan, J. Zhou, Q. Huang, S. Xu, X. Zhang, Y. Zhao, G. Hou, Passivating contacts for crystalline silicon solar cells: an overview of the current advances and future perspectives, Adv. Energy Mater. 14 (2024) 2304338, https://doi.org/10.1002/aenm.202304338.

[37] S. Olibet, E. Vallat-Sauvain, C. Ballif, Model for a-Si:H/c-Si interface recombination based on the amphoteric nature of silicon dangling bonds, Phys. Rev. B 76 (2007) 035326, https://doi.org/10.1103/PhysRevB.76.035326.

[38] S.R. Dhariwal, M. Smirty, On the sensitivity of open-circuit voltage and fill factor on dangling bond density and Fermi level position in amorphous silicon p–i–n solar cell, Sol. Energy Mater. Sol. Cells 90 (2006) 1254–1272, https://doi.org/10.1016/j.solmat.2005.08.001.

[39] J. Panigrahi, V.K. Komarala, Progress on the intrinsic a-Si:H films for interface passivation of silicon heterojunction solar cells: a review, J. Non-Cryst. Solids 574 (2021) 121166, https://doi.org/10.1016/j.jnoncrysol.2021.121166.

[40] B. Hoex, Material properties of AlOx for silicon surface passivation. Surface Passivation of Industrial Crystalline Silicon Solar Cells, Institution of Engineering and Technology, 2018, pp. 27–40.

[41] A.G. Aberle, Surface passivation of crystalline silicon solar cells: a review, Prog. Photovolt.: Res. Appl. 8 (2000) 473–487, https://doi.org/10.1002/1099-159X(200009/10)8:5<473::AID-PIP337>3.0.CO;2-D.

[42] R. Corkish, M.A. Green, M.E. Watt, S.R. Wenham, Applied photovoltaics, Routledge, 2013.

[43] S. Acharyya, S. Sadhukhan, T. Panda, D.K. Ghosh, N.C. Mandal, A. Nandi, S. Bose, G. Das, S. Maity, P. Chaudhuri, H. Saha, D. Banerjee, Dopant-free materials for carrier-selective passivating contact solar cells: a review, Surf. Interfaces 28 (2022) 101687, https://doi.org/10.1016/j.surfin.2021.101687.

[44] G. Nogay, J.P. Seif, Y. Riesen, A. Tomasi, Q. Jeangros, N. Wyrsch, F.J. Haug, S. D. Wolf, C. Ballif, Nanocrystalline silicon carrier collectors for silicon heterojunction solar cells and impact on low-temperature device characteristics, IEEE J. Photovolt. 6 (2016) 1654–1662, https://doi.org/10.1109/JPHOTOV.2016.2604574.

[45] A.G. e Aber, S. Glunz, W. Warta, Field effect passivation of high efficiency silicon solar cells, Sol. Energy Mater. Sol. Cells 29 (1993) 175–182, https://doi.org/10.1016/0927-0248(93)90075-E.

[46] S.Y. Herasimenka, W.J. Dauksher, S.G. Bowden, 750 mV open circuit voltage measured on 50 μm thick silicon heterojunction solar cell, Appl. Phys. Lett. 103 (2013) 053511.

[47] R.T. Tung, The physics and chemistry of the Schottky barrier height, Appl. Phys. Rev. 1 (2014) 011304, https://doi.org/10.1063/1.4858400.

[48] U. Würfel, A. Cuevas, P. Würfel, Charge carrier separation in solar cells, IEEE J. Photovolt. 5 (2015) 461–469, https://doi.org/10.1109/JPHOTOV.2014.2363550.

[49] R. Brendel, R. Peibst, Contact selectivity and efficiency in crystalline silicon photovoltaics, IEEE J. Photovolt. 6 (2016) 1413–1420, https://doi.org/10.1109/JPHOTOV.2016.2598267.

[50] Y. Wang, S.-T. Zhang, L. Li, X. Yang, L. Lu, D. Li, Dopant-free passivating contacts for crystalline silicon solar cells: progress and prospects, EcoMat 5 (2023) e12292, https://doi.org/10.1002/eom2.12292.

[51] J. Yu, Y. Fu, L. Zhu, Z. Yang, X. Yang, L. Ding, Y. Zeng, B. Yan, J. Tang, P. Gao, J. Ye, Heterojunction solar cells with asymmetrically carrier-selective contact structure of molybdenum-oxide/silicon/magnesium-oxide, Sol. Energy 159 (2018) 704–709, https://doi.org/10.1016/j.solener.2017.11.047.

[52] G. Behera, Vikram, A. Kumar, K. Balasubramaniam, A. Alam, First-principles study of the surface passivation effect in the Si/MoOx interface, J. Phys. Chem. C. 125 (2021) 11513–11523, https://doi.org/10.1021/acs.jpcc.1c00208.

[53] T.G. Allen, J. Bullock, X. Yang, A. Javey, S. De Wolf, Passivating contacts for crystalline silicon solar cells, Nat. Energy 4 (2019) 914–928, https://doi.org/10.1038/s41560-019-0463-6.

[54] V.N. Sheremet, Metrological aspects of measuring resistance of ohmic contacts, Radioelectron. Commun. Syst. 53 (2010) 119–128, https://doi.org/10.3103/S0735272710030015.

[55] S. Guo, G. Gregory, A.M. Gabor, W.V. Schoenfeld, K.O. Davis, Detailed investigation of TLM contact resistance measurements on crystalline silicon solar cells, Sol. Energy 151 (2017) 163–172, https://doi.org/10.1016/j.solener.2017.05.015.

[56] J. Bullock, A. Cuevas, T. Allen, C. Battaglia, Molybdenum oxide MoOx: a versatile hole contact for silicon solar cells, Appl. Phys. Lett. 105 (2014) 232109, https://doi.org/10.1063/1.4903467.

[57] R.H. Cox, H. Strack, Ohmic contacts for GaAs devices, Solid-State Electron. 10 (1967) 1213–1218, https://doi.org/10.1016/0038-1101(67)90063-9.

[58] G. Du, L. Li, H. Zhu, L. Lu, X. Zhou, Z. Gu, S.-T. Zhang, X. Yang, J. Wang, L. Yang, X. Chen, D. Li, High-performance hole-selective V2OX/SiOX/NiOX contact for crystalline silicon solar cells, EcoMat 4 (2022) e12175, https://doi.org/10.1002/eom2.12175.

[59] J. Melskens, B.W.H. v.d. Loo, B. Macco, L.E. Black, S. Smit, W.M.M. Kessels, Passivating contacts for crystalline silicon solar cells: from concepts and materials to prospects, IEEE J. Photovolt. 8 (2018) 373–388, https://doi.org/10.1109/JPHOTOV.2018.2797106.

[60] A. Onno, C. Chen, P. Koswatta, M. Boccard, Z.C. Holman, Passivation, conductivity, and selectivity in solar cell contacts: Concepts and simulations based on a unified partial-resistances framework, J. Appl. Phys. 126 (2019) 183103, https://doi.org/10.1063/1.5117201.

[61] J. Schmidt, R. Peibst, R. Brendel, Surface passivation of crystalline silicon solar cells: present and future, Sol. Energy Mater. Sol. Cells 187 (2018) 39–54, https://doi.org/10.1016/j.solmat.2018.06.047.

[62] J. Schmidt, A. Merkle, R. Brendel, B. Hoex, M.C.Mv de Sanden, W.M.M. Kessels, Surface passivation of high-efficiency silicon solar cells by atomic-layer-deposited Al2O3, Prog. Photovolt.: Res. Appl. 16 (2008) 461–466, https://doi.org/10.1002/pip.823.

[63] R.S. Bonilla, B. Hoex, P. Hamer, P.R. Wilshaw, Dielectric surface passivation for silicon solar cells: A review, 214 (2017) 1700293. https://doi.org/https://doi.org/10.1002/pssa.201700293.

[64] S. De Wolf, M. Kondo, Abruptness of a-Si:H/c-Si interface revealed by carrier lifetime measurements, Appl. Phys. Lett. 90 (2007) 042111, https://doi.org/10.1063/1.2432297.

[65] V. Kanneboina, Detailed review on c-Si/a-Si:H heterojunction solar cells in perspective of experimental and simulation, Microelectron. Eng. 265 (2022) 111884, https://doi.org/10.1016/j.mee.2022.111884.

[66] S. Olibet, E. Vallat-Sauvain, L. Fesquet, C. Monachon, A. Hessler-Wyser, J. Damon-Lacoste, S. De Wolf, C. Ballif, Properties of interfaces in amorphous/crystalline silicon heterojunctions, Phys. Status Solidi (a) 207 (2010) 651–656, https://doi.org/10.1002/pssa.200982845.

[67] X. Fan, M. Rabelo, Y. Hu, M.Q. Khokhar, Y. Kim, J. Yi, Factors affecting the performance of hjt silicon solar cells in the intrinsic and emitter layers: a review, Trans. Electr. Electron. Mater. 24 (2023) 123–131, https://doi.org/10.1007/s42341-022-00427-3.

[68] D. Hegemann, B. Hanselmann, N. Blanchard, M. Amberg, Plasma-substrate interaction during plasma deposition on polymers, Contrib. Plasma Phys. 54 (2014) 162–169, https://doi.org/10.1002/ctpp.201310064.

[69] U.K. Das, M.Z. Burrows, M. Lu, S. Bowden, R.W. Birkmire, Surface passivation and heterojunction cells on Si (100) and (111) wafers using dc and rf plasma deposited Si:H thin films, Appl. Phys. Lett. 92 (2008) 063504, https://doi.org/10.1063/1.2857465.

[70] Y.-H. Chu, C.-C. Lee, T.-H. Chang, S.-Y. Chang, J.-Y. Chang, T. Li, I.C. Chen, Investigation of hydrogenated amorphous silicon as passivation layer by high density plasma, Thin Solid Films 570 (2014) 591–594, https://doi.org/10.1016/j.tsf.2014.03.064.

[71] H. Sai, P.-W. Chen, H.-J. Hsu, T. Matsui, S. Nunomura, K. Matsubara, Impact of intrinsic amorphous silicon bilayers in silicon heterojunction solar cells, J. Appl. Phys. 124 (2018) 103102, https://doi.org/10.1063/1.5045155.

[72] Y. Li, X. Ru, M. Yang, Y. Zheng, S. Yin, C. Hong, F. Peng, M. Qu, C. Xue, J. Lu, L. Fang, C. Su, D. Chen, J. Xu, C. Yan, Z. Li, X. Xu, Z. Shao, Flexible silicon solar cells with high power-to-weight ratios, Nature 626 (2024) 105–110, https://doi.org/10.1038/s41586-023-06948-y.

[73] A. Descoeudres, L. Barraud, R. Bartlome, G. Choong, S. De Wolf, F. Zicarelli, C. Ballif, The silane depletion fraction as an indicator for the amorphous/crystalline silicon interface passivation quality, Appl. Phys. Lett. 97 (2010) 183505, https://doi.org/10.1063/1.3511737.

[74] A.B. Morales-Vilches, E.-C. Wang, T. Henschel, M. Kubicki, A. Cruz, S. Janke, L. Korte, R. Schlatmann, B. Stannowski, Improved surface passivation by wet texturing, ozone-based cleaning, and plasma-enhanced chemical vapor deposition

processes for high-efficiency silicon heterojunction solar cells, Phys. Status Solidi (a) 217 (2020) 1900518, https://doi.org/10.1002/pssa.201900518.
[75] S. De Wolf, M. Kondo, Nature of doped a-Si:H/c-Si interface recombination, J. Appl. Phys. 105 (2009) 103707, https://doi.org/10.1063/1.3129578.
[76] S. De Wolf, M. Kondo, Boron-doped a-Si:H/c-Si interface passivation: degradation mechanism, Appl. Phys. Lett. 91 (2007) 112109, https://doi.org/10.1063/1.2783972.
[77] L. Bodlak, J. Temmler, A. Moldovan, J. Rentsch, Improved passivation for SHJ utilizing dual intrinsic a-Si:H layers on an inline PECVD tool, AIP Conf. Proc. 2147 (2019) 050001, https://doi.org/10.1063/1.5123850.
[78] Z. Sun, X. Chen, Y. He, J. Li, J. Wang, H. Yan, Y. Zhang, Toward efficiency limits of crystalline silicon solar cells: recent progress in high-efficiency silicon heterojunction solar cells, Adv. Energy Mater. 12 (2022) 2200015, https://doi.org/10.1002/aenm.202200015.
[79] L. Zhao, H. Diao, X. Zeng, C. Zhou, H. Li, W. Wang, Comparative study of the surface passivation on crystalline silicon by silicon thin films with different structures, Phys. B: Condens. Matter 405 (2010) 61–64, https://doi.org/10.1016/j.physb.2009.08.024.
[80] Z. Mrazkova, I.P. Sobkowicz, M. Foldyna, K. Postava, I. Florea, J. Pištora, P. Roca i Cabarrocas, Optical properties and performance of pyramidal texture silicon heterojunction solar cells: key role of vertex angles, Prog. Photovolt.: Res. Appl. 26 (2018) 369–376, https://doi.org/10.1002/pip.2994.
[81] M. Boccard, Z.C. Holman, Amorphous silicon carbide passivating layers for crystalline-silicon-based heterojunction solar cells, J. Appl. Phys. 118 (2015) 065704, https://doi.org/10.1063/1.4928203.
[82] Z. Yu, I. Pereyra, M.N.P. Carreno, Wide optical band gap window layers for solar cells, Sol. Energy Mater. Sol. Cells 66 (2001) 155–162, https://doi.org/10.1016/S0927-0248(00)00168-9.
[83] P.M. Kaminski, A. Abbas, K. Bass, G. Claudio, Passivation of silicon wafers by Silicon Carbide (SiCx) thin film grown by sputtering, Energy Procedia 10 (2011) 71–75, https://doi.org/10.1016/j.egypro.2011.10.155.
[84] E. Donercark, S.H. Sedani, I. Kabaçelik, A. Salimi, R. Turan, Interface and material properties of wide band gap a-SiCx:H thin films for solar cell applications, Renew. Energy 183 (2022) 781–790, https://doi.org/10.1016/j.renene.2021.11.065.
[85] C. Ehling, D. Treptow, G. Bilger, F. Einsele, M.B. Schubert, Electronic surface passivation of crystalline silicon solar cells by a-SiC:H, 2010 35th IEEE Photovolt. Spec. Conf. (2010) 001368–001373.
[86] H. Fujiwara, T. Kaneko, M. Kondo, Application of hydrogenated amorphous silicon oxide layers to c-Si heterojunction solar cells, Appl. Phys. Lett. 91 (2007) 133508, https://doi.org/10.1063/1.2790815.
[87] J. Ge, M. Tang, J. Wong, R. Stangl, Z. Zhang, T. Dippell, M. Doerr, O. Hohn, M. Huber, P. Wohlfart, A.G. Aberle, T. Mueller, Investigation of wide process temperature window for amorphous silicon suboxide thin-film passivation deposited by inductively coupled PECVD, IEEE J. Photovolt. 5 (2015) 705–710, https://doi.org/10.1109/JPHOTOV.2015.2397593.
[88] S.M. Iftiquar, The roles of deposition pressure and rf power in opto-electronic properties of a-SiO:H films, J. Phys. D: Appl. Phys. 31 (1998) 1630, https://doi.org/10.1088/0022-3727/31/14/004.
[89] K. Jiang, W. Liu, Y. Yang, Z. Yan, S. Huang, Z. Li, X. Li, L. Zhang, Z. Liu, Functions of oxygen atoms in hydrogenated amorphous silicon oxide layers for rear-emitter silicon heterojunction solar cells, J. Mater. Sci.: Mater. Electron. 33 (2022) 416–426, https://doi.org/10.1007/s10854-021-07315-1.
[90] K. Jiang, Y. Yang, Z. Yan, S. Huang, X. Li, Z. Li, Y. Zhou, L. Zhang, F. Meng, Z. Liu, W. Liu, Balance of efficiency and stability of silicon heterojunction solar cells, Sol. Energy Mater. Sol. Cells 243 (2022) 111801, https://doi.org/10.1016/j.solmat.2022.111801.
[91] B. Zhang, Y. Zhang, R. Cong, Y. Li, W. Yu, G. Fu, Superior silicon surface passivation in HIT solar cells by optimizing a-SiOx:H thin films: a compact intrinsic passivation layer, Sol. Energy 155 (2017) 670–678, https://doi.org/10.1016/j.solener.2017.06.066.
[92] L.G. Gerling, C. Voz, R. Alcubilla, J. Puigdollers, Origin of passivation in hole-selective transition metal oxides for crystalline silicon heterojunction solar cells, J. Mater. Res. 32 (2017) 260–268, https://doi.org/10.1557/jmr.2016.453.
[93] B. Liao, B. Hoex, A.G. Aberle, D. Chi, C.S. Bhatia, Excellent c-Si surface passivation by low-temperature atomic layer deposited titanium oxide, Appl. Phys. Lett. 104 (2014) 253903, https://doi.org/10.1063/1.4885096.
[94] X. Yang, P. Zheng, Q. Bi, K. Weber, Silicon heterojunction solar cells with electron selective TiOx contact, Sol. Energy Mater. Sol. Cells 150 (2016) 32–38, https://doi.org/10.1016/j.solmat.2016.01.020.
[95] B. Bilal, H. Najeeb-ud-Din, Fundamentals of and recent advances in carrier selective passivating contacts for silicon solar cells, J. Electron. Mater. 50 (2021) 3761–3772, https://doi.org/10.1007/s11664-021-08933-5.
[96] D. Gao, Y. Li, B. Zhang, X. Wang, W. Lu, H. Liu, R. Cong, W. Yu, G. Fu, Structural and photoluminescence properties of nc-SiOx:H/a-SiOx:H multilayer films deposited at low temperature by VHF-PECVD technique, J. Inorg. Organomet. Polym. Mater. 29 (2019) 806–812, https://doi.org/10.1007/s10904-018-01055-2.
[97] L. Mazzarella, A.B. Morales-Vilches, L. Korte, R. Schlatmann, B. Stannowski, Ultra-thin nanocrystalline n-type silicon oxide front contact layers for rear-emitter silicon heterojunction solar cells, Sol. Energy Mater. Sol. Cells 179 (2018) 386–391, https://doi.org/10.1016/j.solmat.2018.01.034.
[98] V. Kanneboina, R. Madaka, P. Agarwal, Stepwise tuning of the doping and thickness of a-Si:H(p) emitter layer to improve the performance of c-Si(n)/a-Si:H (p) heterojunction solar cells, J. Mater. Sci.: Mater. Electron. 32 (2021) 4457–4465, https://doi.org/10.1007/s10854-020-05187-5.
[99] V. Kanneboina, P. Agarwal, Spectroscopic ellipsometry investigation to study the microstructure evolution in boron-doped amorphous silicon films as a result of hydrogen dilution, SN Appl. Sci. 3 (2021) 500, https://doi.org/10.1007/s42452-021-04495-7.
[100] M.A. Green, E.D. Dunlop, M. Yoshita, N. Kopidakis, K. Bothe, G. Siefer, X. Hao, Solar cell efficiency tables (Version 63), Prog. Photovolt.: Res. Appl. 32 (2024) 3–13, https://doi.org/10.1002/pip.3750.
[101] Z.C. Holman, A. Descoeudres, L. Barraud, F.Z. Fernandez, J.P. Seif, S.D. Wolf, C. Ballif, Current losses at the front of silicon heterojunction solar cells, IEEE J. Photovolt. 2 (2012) 7–15, https://doi.org/10.1109/JPHOTOV.2011.2174967.
[102] D.P. Pham, S. Kim, S. Kim, S. Lee, A.H.T. Le, J. Park, J. Yi, Ultra-thin stack of n-type hydrogenated microcrystalline silicon and silicon oxide front contact layer for rear-emitter silicon heterojunction solar cells, Mater. Sci. Semicond. Process. 96 (2019) 1–7, https://doi.org/10.1016/j.mssp.2019.02.017.
[103] A.N. Fioretti, M. Boccard, R. Monnard, C. Ballif, Low-Temperature p-type microcrystalline silicon as carrier selective contact for silicon heterojunction solar cells, IEEE J. Photovolt. 9 (2019) 1158–1165, https://doi.org/10.1109/JPHOTOV.2019.2917550.
[104] C.W. Peng, C. Lei, T. Ruan, J. Zhong, M. Yang, W. Long, C. Yu, Y. Li, X. Xu, High Phosphorus-doped seed layer in microcrystalline silicon oxide front contact layers for silicon heterojunction solar cells, IEEE 46th Photovolt. Spec. Conf. (PVSC) 2019 (2019) 2550–2553.
[105] O. Gabriel, S. Kirner, M. Klingsporn, F. Friedrich, B. Stannowski, R. Schlatmann, On the plasma chemistry during plasma enhanced chemical vapor deposition of microcrystalline silicon oxides, Plasma Process. Polym. 12 (2015) 82–91, https://doi.org/10.1002/ppap.201400114.
[106] D. Das, K. Bhattacharya, Characterization of the Si:H network during transformation from amorphous to micro- and nanocrystalline structures, J. Appl. Phys. 100 (2006) 103701, https://doi.org/10.1063/1.2384812.
[107] S. Yeop Myong, H. Kew Lee, E. Yoon, K. Su Lim, Highly conductive boron-doped nanocrystalline silicon-carbide film prepared by low-hydrogen-dilution photo-CVD method using ethylene as a carbon source, J. Non-Cryst. Solids 298 (2002) 131–136, https://doi.org/10.1016/S0022-3093(02)00916-X.
[108] C.-D. Sen, J.-I. Son, H.-H. Kim, H.-S. Yun, N.-H. Cho, Variation of the nanostructural feature of nc-SiC:H thin films with post-deposition thermal annealing, Thin Solid Films 571 (2014) 238–244, https://doi.org/10.1016/j.tsf.2014.10.002.
[109] M. Sharma, J. Panigrahi, V.K. Komarala, Nanocrystalline silicon thin film growth and application for silicon heterojunction solar cells: a short review, Nanoscale Adv. 3 (2021) 3373–3383, https://doi.org/10.1039/D0NA00791A.
[110] Y. Zhang, R. Cong, W. Zhao, Y. Li, C. Jin, W. Yu, G. Fu, Improved hetero-interface passivation by microcrystalline silicon oxide emitter in silicon heterojunction solar cells, Sci. Bull. 61 (2016) 787–793, https://doi.org/10.1007/s11434-016-1065-3.
[111] J.P. Seif, A. Descoeudres, G. Nogay, S. Hänni, S.Md Nicolas, N. Holm, J. Geissbühler, A. Hessler-Wyser, M. Duchamp, R.E. Dunin-Borkowski, M. Ledinsky, S.D. Wolf, C. Ballif, Strategies for doped nanocrystalline silicon integration in silicon heterojunction solar cells, IEEE J. Photovolt. 6 (2016) 1132–1140, https://doi.org/10.1109/JPHOTOV.2016.2571619.
[112] M. Köhler, A. Zamchiy, M. Pomaska, A. Lambertz, F. Lentz, W. Duan, V. Smirnov, F. Finger, U. Rau, K. Ding, Development of a Transparent Passivated Contact as a Front Side Contact for Silicon Heterojunction Solar Cells, 2018 IEEE 7th World Conference on Photovoltaic Energy Conversion (WCPEC) (A Joint Conference of 45th IEEE PVSC, 28th PVSEC & 34th EU PVSEC), 2018, pp. 3468-3472.
[113] M. Pomaska, W. Beyer, E. Neumann, F. Finger, K. Ding, Impact of microcrystalline silicon carbide growth using hot-wire chemical vapor deposition on crystalline silicon surface passivation, Thin Solid Films 595 (2015) 217–220, https://doi.org/10.1016/j.tsf.2015.05.057.
[114] J.-S. Cho, E. Jang, D. Lim, S. Ahn, J. Yoo, A. Cho, J.H. Park, K. Kim, B.-H. Choi, Wide-bandgap nanocrystalline silicon-carbon alloys for photovoltaic applications, Sol. Energy Mater. Sol. Cells 182 (2018) 220–227, https://doi.org/10.1016/j.solmat.2018.03.035.
[115] O. Madani Ghahfarokhi, K. von Maydell, C. Agert, Enhanced passivation at amorphous/crystalline silicon interface and suppressed Schottky barrier by deposition of microcrystalline silicon emitter layer in silicon heterojunction solar cells, Appl. Phys. Lett. 104 (2014) 113901, https://doi.org/10.1063/1.4868726.
[116] P. Roca i Cabarrocas, N. Layadi, T. Heitz, B. Drévillon, I. Solomon, Substrate selectivity in the formation of microcrystalline silicon: mechanisms and technological consequences, Appl. Phys. Lett. 66 (1995) 3609–3611, https://doi.org/10.1063/1.113803.
[117] M. Boccard, R. Monnard, L. Antognini, C. Ballif, Silicon oxide treatment to promote crystallinity of p-type microcrystalline layers for silicon heterojunction solar cells, AIP Conf. Proc. 1999 (2018) 040003, https://doi.org/10.1063/1.5049266.
[118] E. Centurioni, D. Iencinella, R. Rizzoli, F. Zignani, Silicon heterojunction solar cell: a new buffer Layer concept with low-temperature epitaxial silicon, IEEE Trans. Electron Devices 51 (2004) 1818–1824, https://doi.org/10.1109/TED.2004.836801.
[119] Y. Xu, Z. Hu, H. Diao, Y. Cai, S. Zhang, X. Zeng, H. Hao, X. Liao, E. Fortunato, R. Martins, Heterojunction solar cells with n-type nanocrystalline silicon emitters on p-type c-Si wafers, J. Non-Cryst. Solids 352 (2006) 1972–1975, https://doi.org/10.1016/j.jnoncrysol.2006.02.028.
[120] Y. Veschetti, J.C. Muller, J. Damon-Lacoste, P. Roca i Cabarrocas, A. S. Gudovskikh, J.P. Kleider, P.J. Ribeyron, E. Rolland, Optimisation of amorphous and polymorphous thin silicon layers for the formation of the front-side of

heterojunction solar cells on p-type crystalline silicon substrates, Thin Solid Films 511-512 (2006) 543–547, https://doi.org/10.1016/j.tsf.2005.12.166.
[121] C. Banerjee, K.L. Narayanan, K. Haga, J. Sritharathikhun, S. Miyajima, A. Yamada, M. Konagai, Fabrication of Microcrystalline Cubic Silicon Carbide/Crystalline Silicon Heterojunction Solar Cell by Hot Wire Chemical Vapor Deposition, Jpn. J. Appl. Phys. 46 (2007) 1, https://doi.org/10.1143/JJAP.46.1.
[122] S.-K. Kim, J.C. Lee, S.-J. Park, Y.-J. Kim, K.H. Yoon, Effect of hydrogen dilution on intrinsic a-Si:H layer between emitter and Si wafer in silicon heterojunction solar cell, Sol. Energy Mater. Sol. Cells 92 (2008) 298–301, https://doi.org/10.1016/j.solmat.2007.09.007.
[123] D. Song, E.-C. Cho, G. Conibeer, C. Flynn, Y. Huang, M.A. Green, Structural, electrical and photovoltaic characterization of Si nanocrystals embedded SiC matrix and Si nanocrystals/c-Si heterojunction devices, Sol. Energy Mater. Sol. Cells 92 (2008) 474–481, https://doi.org/10.1016/j.solmat.2007.11.002.
[124] C. Banerjee, J. Sritharathikhun, A. Yamada, M. Konagai, Fabrication of heterojunction solar cells by using microcrystalline hydrogenated silicon oxide film as an emitter, J. Phys. D: Appl. Phys. 41 (2008) 185107, https://doi.org/10.1088/0022-3727/41/18/185107.
[125] J. Sritharathikhun, H. Yamamoto, S. Miyajima, A. Yamada, M. Konagai, Optimization of amorphous silicon oxide buffer layer for high-efficiency p-type hydrogenated microcrystalline silicon oxide/n-type crystalline silicon heterojunction solar cells, Jpn. J. Appl. Phys. 47 (2008) 8452, https://doi.org/10.1143/JJAP.47.8452.
[126] L. Korte, E. Conrad, H. Angermann, R. Stangl, M. Schmidt, Advances in a-Si:H/c-Si heterojunction solar cell fabrication and characterization, Sol. Energy Mater. Sol. Cells 93 (2009) 905–910, https://doi.org/10.1016/j.solmat.2008.10.020.
[127] B.-R. Wu, D.-S. Wuu, M.-S. Wan, W.-H. Huang, H.-Y. Mao, R.-H. Horng, Fabrication of nc-Si/c-Si solar cells using hot-wire chemical vapor deposition and laser annealing, Sol. Energy Mater. Sol. Cells 93 (2009) 993–995, https://doi.org/10.1016/j.solmat.2008.11.027.
[128] B.R. Wu, D.S. Wuu, M.S. Wan, H.Y. Mao, R.H. Horng, Fabrication of selective-emitter silicon heterojunction solar cells using hot-wire chemical vapor deposition and laser doping, Thin Solid Films 517 (2009) 4749–4752, https://doi.org/10.1016/j.tsf.2009.03.119.
[129] Y.-W. Ok, M.-G. Kang, D. Kim, J.C. Lee, K.H. Yoon, Understanding of a-Si:H(p)/c-Si(n) heterojunction solar cell through analysis of cells with point-contacted p/n junction, Curr. Appl. Phys. 9 (2009) 1186–1190, https://doi.org/10.1016/j.cap.2009.01.010.
[130] Z. Jiang, Y. Dou, Y. Zhang, Y. Zhou, F. Liu, M. Zhu, Effect of chemical polish etching and post annealing on the performance of silicon heterojunction solar cells, J. Semicond. 30 (2009) 084010, https://doi.org/10.1088/1674-4926/30/8/084010.
[131] J. Sritharathikhun, F. Jiang, S. Miyajima, A. Yamada, M. Konagai, Optimization of p-type hydrogenated microcrystalline silicon oxide window layer for high-efficiency crystalline silicon heterojunction solar cells, Jpn. J. Appl. Phys. 48 (2009) 101603, https://doi.org/10.1143/JJAP.48.101603.
[132] S. Miyajima, J. Irikawa, A. Yamada, M. Konagai, High-quality nanocrystalline cubic silicon carbide emitter for crystalline silicon heterojunction solar cells, Appl. Phys. Lett. 97 (2010) 023504, https://doi.org/10.1063/1.3460917.
[133] V.A. Dao, Y. Lee, S. Kim, Y. Kim, N. Lakshminarayan, J. Yi, Interface Characterization and Electrical Transport Mechanisms in a-Si:H/c-Si Heterojunction Solar Cells, H312, J. Electrochem. Soc. 158 (2011), https://doi.org/10.1149/1.3534202.
[134] A. Favier, D. Muñoz, S. Martín de Nicolás, P.J. Ribeyron, Boron-doped zinc oxide layers grown by metal-organic CVD for silicon heterojunction solar cells applications, Sol. Energy Mater. Sol. Cells 95 (2011) 1057–1061, https://doi.org/10.1016/j.solmat.2010.11.013.
[135] S. Rattanapan, T. Watahiki, S. Miyajima, M. Konagai, Improvement of rear surface passivation quality in p-type silicon heterojunction solar cells using boron-doped microcrystalline silicon oxide, Jpn. J. Appl. Phys. 50 (2011) 082301, https://doi.org/10.1143/JJAP.50.082301.
[136] J.-C. Hsiao, C.-H. Chen, C.-C. Lin, D.-C. Wu, P. Yu, Effect of hydrogen dilution on the intrinsic a-Si:H film of the heterojunction silicon-based solar cell, J. Electrochem. Soc. 158 (2011) H876, https://doi.org/10.1149/1.3607981.
[137] C.-S. Liu, C.-Y. Wu, I.-W. Chen, H.-C. Lee, L.-S. Hong, High-rate deposition of a-Si:H thin layers for high-performance silicon heterojunction solar cells, Prog. Photovolt.: Res. Appl. 21 (2013) 326–331, https://doi.org/10.1002/pip.1189.
[138] S.Q. Xiao, S. Xu, H.P. Zhou, D.Y. Wei, S.Y. Huang, L.X. Xu, C.C. Sern, Y.N. Guo, S. Khan, Amorphous/crystalline silicon heterojunction solar cells via remote inductively coupled plasma processing, Appl. Phys. Lett. 100 (2012) 233902, https://doi.org/10.1063/1.4721642.
[139] L. Barraud, Z.C. Holman, N. Badel, P. Reiss, A. Descoeudres, C. Battaglia, S. De Wolf, C. Ballif, Hydrogen-doped indium oxide/indium tin oxide bilayers for high-efficiency silicon heterojunction solar cells, Sol. Energy Mater. Sol. Cells 115 (2013) 151–156, https://doi.org/10.1016/j.solmat.2013.03.024.
[140] D. Zhang, I.A. Digdaya, R. Santbergen, R.A.C.M.M. van Swaaij, P. Bronsveld, M. Zeman, J.A.M. van Roosmalen, A.W. Weeber, Design and fabrication of a SiOx/ITO double-layer anti-reflective coating for heterojunction silicon solar cells, Sol. Energy Mater. Sol. Cells 117 (2013) 132–138, https://doi.org/10.1016/j.solmat.2013.05.044.
[141] S.Q. Hussain, W.-K. Oh, S. Ahn, A.H.T. Le, S. Kim, Y. Lee, J. Yi, RF magnetron sputtered indium tin oxide films with high transmittance and work function for a-Si:H/c-Si heterojunction solar cells, Vacuum 101 (2014) 18–21, https://doi.org/10.1016/j.vacuum.2013.07.004.
[142] J.-C. Hsiao, C.-H. Chen, H.-J. Yang, C.-L. Wu, C.-M. Fan, C.-F. Huang, C.-C. Lin, P. Yu, J.-C. Hwang, Highly textured ZnO:B films grown by low pressure chemical vapor deposition for efficiency enhancement of heterojunction silicon-based solar cells, J. Taiwan Inst. Chem. Eng. 44 (2013) 758–761, https://doi.org/10.1016/j.jtice.2013.01.027.
[143] S.Q. Hussain, S. Kim, S. Ahn, N. Balaji, Y. Lee, J.H. Lee, J. Yi, Influence of high work function ITO:Zr films for the barrier height modification in a-Si:H/c-Si heterojunction solar cells, Sol. Energy Mater. Sol. Cells 122 (2014) 130–135, https://doi.org/10.1016/j.solmat.2013.11.031.
[144] S. Kim, J. Jung, Y.-J. Lee, S. Ahn, S.Q. Hussain, J. Park, B.-S. Song, S. Han, V. A. Dao, J. Lee, J. Yi, Role of double ITO/In2O3 layer for high efficiency amorphous/crystalline silicon heterojunction solar cells, Mater. Res. Bull. 58 (2014) 83–87, https://doi.org/10.1016/j.materresbull.2014.05.003.
[145] Z. Wu, L. Zhang, R. Chen, W. Liu, Z. Li, F. Meng, Z. Liu, Improved amorphous/crystalline silicon interface passivation for silicon heterojunction solar cells by hot-wire atomic hydrogen during doped a-Si:H deposition, Appl. Surf. Sci. 475 (2019) 504–509, https://doi.org/10.1016/j.apsusc.2018.12.239.
[146] Y. Lee, H. Kim, S.M. Iftiquar, S. Kim, S. Kim, S. Ahn, Y.-J. Lee, V.A. Dao, J. Yi, Study of stacked-emitter layer for high efficiency amorphous/crystalline silicon heterojunction solar cells, J. Appl. Phys. 116 (2014) 244506, https://doi.org/10.1063/1.4905013.
[147] Y.S. Cho, C.H. Hsu, S.Y. Lien, D.S. Wuu, P. Han, C.F. Chen, J.H. Wang, Effect of plasma radical composition in intrinsic a-si:h on performances of heterojunction solar cells, IEEE Trans. Plasma Sci. 42 (2014) 3786–3791, https://doi.org/10.1109/TPS.2014.2333514.
[148] O. Madani Ghahfarokhi, K. Chakanga, S. Geissendoerfer, O. Sergeev, K. von Maydell, C. Agert, DC-sputtered ZnO:Al as transparent conductive oxide for silicon heterojunction solar cells with μc-Si:H emitter, Prog. Photovolt.: Res. Appl. 23 (2015) 1340–1352, https://doi.org/10.1002/pip.2570.
[149] S. Kim, V.A. Dao, C. Shin, N. Balaji, J. Yi, Influence of n-doped μc-Si:H back surface field layer with micro growth in crystalline-amorphous silicon heterojunction solar cells, J. Nanosci. Nanotechnol. 14 (2014) 9258–9262, https://doi.org/10.1166/jnn.2014.10123.
[150] H. Zhang, K. Nakada, S. Miyajima, M. Konagai, High-performance a-Si1–xOx:H/c-Si heterojunction solar cells realized by the a-Si:H/a-Si1–xOx:H stack buffer layer, Phys. Status Solidi (RRL) – Rapid Res. Lett. 9 (2015) 225–229, https://doi.org/10.1002/pssr.201409546.
[151] M. Morales-Masis, S.M.D. Nicolas, J. Holovsky, S.D. Wolf, C. Ballif, Low-temperature high-mobility amorphous IZO for silicon heterojunction solar cells, IEEE J. Photovolt. 5 (2015) 1340–1347, https://doi.org/10.1109/JPHOTOV.2015.2450993.
[152] F. Meng, L. Shen, J. Shi, L. Zhang, J. Liu, Y. Liu, Z. Liu, Role of the buffer at the interface of intrinsic a-Si:H and p-type a-Si:H on amorphous/crystalline silicon heterojunction solar cells, Appl. Phys. Lett. 107 (2015) 223901, https://doi.org/10.1063/1.4936196.
[153] J. Yu, J. Bian, W. Duan, Y. Liu, J. Shi, F. Meng, Z. Liu, Tungsten doped indium oxide film: Ready for bifacial copper metallization of silicon heterojunction solar cell, Sol. Energy Mater. Sol. Cells 144 (2016) 359–363, https://doi.org/10.1016/j.solmat.2015.09.033.
[154] X. Zeng, X. Wen, X. Sun, W. Liao, Y. Wen, Boron-doped zinc oxide thin films grown by metal organic chemical vapor deposition for bifacial a-Si:H/c-Si heterojunction solar cells, Thin Solid Films 605 (2016) 257–262, https://doi.org/10.1016/j.tsf.2015.11.023.
[155] N. Kim, H.-D. Um, I. Choi, K.-H. Kim, K. Seo, 18.4%-efficient heterojunction Si solar cells using optimized ITO/Top electrode, ACS Appl. Mater. Interfaces 8 (2016) 11412–11417, https://doi.org/10.1021/acsami.6b00981.
[156] A. Richter, F. Lentz, M. Meier, F. Finger, K. Ding, Light management in planar silicon heterojunction solar cells via nanocrystalline silicon oxide films and nano-imprint textures, Phys. Status Solidi (a) 213 (2016) 1976–1982, https://doi.org/10.1002/pssa.201533024.
[157] S. Kim, S.M. Iftiquar, D. Lee, H. Lee, J. Kim, J. Jung, D. Oh, V.A. Dao, J. Yi, Improvement in front-contact resistance and interface passivation of heterojunction amorphous/crystalline silicon solar cell by hydrogen-diluted stacked emitter, IEEE J. Photovolt. 6 (2016) 837–845, https://doi.org/10.1109/JPHOTOV.2016.2553779.
[158] W. Liu, L. Zhang, R. Chen, F. Meng, W. Guo, J. Bao, Z. Liu, Underdense a-Si:H film capped by a dense film as the passivation layer of a silicon heterojunction solar cell, J. Appl. Phys. 120 (2016) 175301, https://doi.org/10.1063/1.4966941.
[159] M. Smeets, K. Bittkau, F. Lentz, A. Richter, K. Ding, R. Carius, U. Rau, U. W. Paetzold, Post passivation light trapping back contacts for silicon heterojunction solar cells, Nanoscale 8 (2016) 18726–18733, https://doi.org/10.1039/C6NR04960E.
[160] G. Nogay, J. Stuckelberger, P. Wyss, Q. Jeangros, C. Allebé, X. Niquille, F. Debrot, M. Despeisse, F.-J. Haug, P. Löper, C. Ballif, Silicon-rich silicon carbide hole-selective rear contacts for crystalline-silicon-based solar cells, ACS Appl. Mater. Interfaces 8 (2016) 35660–35667, https://doi.org/10.1021/acsami.6b12714.
[161] L. Mazzarella, S. Kirner, O. Gabriel, S.S. Schmidt, L. Korte, B. Stannowski, B. Rech, R. Schlatmann, Nanocrystalline silicon emitter optimization for Si-HJ solar cells: Substrate selectivity and CO2 plasma treatment effect, Phys. Status Solidi (a) 214 (2017) 1532958, https://doi.org/10.1002/pssa.201532958.
[162] M. Agarwal, A. Pawar, N. Wadibhasme, R. Dusane, Controlling the c-Si/a-Si:H interface in silicon heterojunction solar cells fabricated by HWCVD, Sol. Energy 144 (2017) 417–423, https://doi.org/10.1016/j.solener.2017.01.039.
[163] S. Li, Z. Shi, Z. Tang, X. Li, Study on the hydrogen doped indium oxide for silicon heterojunction solar cell application, J. Alloy. Compd. 705 (2017) 198–204, https://doi.org/10.1016/j.jallcom.2017.02.133.
[164] G. Dong, Y. Zhou, H. Zhang, F. Liu, G. Li, M. Zhu, Passivation of high aspect ratio silicon nanowires by using catalytic chemical vapor deposition for radial

heterojunction solar cell application, RSC Adv. 7 (2017) 45101–45106, https://doi.org/10.1039/C7RA08343B.
[165] M. Pomaska, A. Richter, F. Lentz, T. Niermann, F. Finger, U. Rau, K. Ding, Wide gap microcrystalline silicon carbide emitter for amorphous silicon oxide passivated heterojunction solar cells, Jpn. J. Appl. Phys. 56 (2017) 022302, https://doi.org/10.7567/JJAP.56.022302.
[166] Y. Kuang, B. Macco, B. Karasulu, C.K. Ande, P.C.P. Bronsveld, M.A. Verheijen, Y. Wu, W.M.M. Kessels, R.E.I. Schropp, Towards the implementation of atomic layer deposited In2O3:H in silicon heterojunction solar cells, Sol. Energy Mater. Sol. Cells 163 (2017) 43–50, https://doi.org/10.1016/j.solmat.2017.01.011.
[167] T. Krajangsang, S. Inthisang, J. Sritharathikhun, A. Hongsingthong, A. Limmanee, S. Kittisontirak, P. Chinnavornrungsee, R. Phatthanakun, K. Sriprapha, An intrinsic amorphous silicon oxide and amorphous silicon stack passivation layer for crystalline silicon heterojunction solar cells, Thin Solid Films 628 (2017) 107–111, https://doi.org/10.1016/j.tsf.2017.03.010.
[168] H. Zhang, K. Nakada, M. Konagai, Effects of epitaxial growth on the optimum condition of intrinsic amorphous silicon oxide buffer layers for silicon heterojunction solar cells, Thin Solid Films 628 (2017) 214–220, https://doi.org/10.1016/j.tsf.2017.03.040.
[169] D.-W. Kang, P. Sichanugrist, H. Zhang, M. Konagai, Wide-bandgap p-type microcrystalline silicon oxycarbide using additional trimethylboron for silicon heterojunction solar cells, Prog. Photovolt.: Res. Appl. 25 (2017) 384–389, https://doi.org/10.1002/pip.2875.
[170] M. Gao, Y. Wan, Y. Li, B. Han, W. Song, F. Xu, L. Zhao, Z. Ma, Effective passivation and tunneling hybrid a-SiOx(In) layer in ITO/n-Si heterojunction photovoltaic device, ACS Appl. Mater. Interfaces 9 (2017) 17565–17575, https://doi.org/10.1021/acsami.7b01447.
[171] J. Yu, J. Zhou, J. Bian, L. Zhang, Y. Liu, J. Shi, F. Meng, J. Liu, Z. Liu, Improved opto-electronic properties of silicon heterojunction solar cells with SiOx/Tungsten-doped indium oxide double anti-reflective coatings, Jpn. J. Appl. Phys. 56 (2017) 08MB09, https://doi.org/10.7567/JJAP.56.08MB09.
[172] X. Yang, J. Chen, W. Liu, F. Li, Y. Sun, Single-side heterojunction solar cell with microcrystalline silicon oxide emitter and diffused back surface field, Phys. Status Solidi (a) 214 (2017) 1700193, https://doi.org/10.1002/pssa.201700193.
[173] G. Nogay, J. Stuckelberger, P. Wyss, E. Rucavado, C. Allebé, T. Koida, M. Morales-Masis, M. Despeisse, F.-J. Haug, P. Löper, C. Ballif, Interplay of annealing temperature and doping in hole selective rear contacts based on silicon-rich silicon-carbide thin films, Sol. Energy Mater. Sol. Cells 173 (2017) 18–24, https://doi.org/10.1016/j.solmat.2017.06.039.
[174] W. Liu, L. Zhang, S. Cong, R. Chen, Z. Wu, F. Meng, Q. Shi, Z. Liu, Controllable a-Si:H/c-Si interface passivation by residual SiH4 molecules in H2 plasma, Sol. Energy Mater. Sol. Cells 174 (2018) 233–239, https://doi.org/10.1016/j.solmat.2017.09.009.
[175] L. Mazzarella, A.B. Morales-Vilches, M. Hendrichs, S. Kirner, L. Korte, R. Schlatmann, B. Stannowski, Nanocrystalline n-type silicon oxide front contacts for silicon heterojunction solar cells: photocurrent enhancement on planar and textured substrates, IEEE J. Photovolt. 8 (2018) 70–78, https://doi.org/10.1109/JPHOTOV.2017.2770164.
[176] S. Li, Z. Tang, J. Xue, J. Gao, Z. Shi, X. Li, Comparative study on front emitter and rear emitter n-type silicon heterojunction solar cells: the role of folded electrical fields, Vacuum 149 (2018) 313–318, https://doi.org/10.1016/j.vacuum.2017.12.041.
[177] I. Mack, J. Stuckelberger, P. Wyss, G. Nogay, Q. Jeangros, J. Horzel, C. Allebé, M. Despeisse, F.J. Haug, A. Ingenito, P. Löper, C. Ballif, Properties of mixed phase silicon-oxide-based passivating contacts for silicon solar cells, Sol. Energy Mater. Sol. Cells 181 (2018) 9–14, https://doi.org/10.1016/j.solmat.2017.12.030.
[178] M. Gao, D. Chen, B. Han, W. Song, M. Zhou, X. Song, F. Xu, L. Zhao, Y. Li, Z. Ma, Bifunctional Hybrid a-SiOx(Mo) layer for hole-selective and interface passivation of highly efficient MoOx/a-SiOx(Mo)/n-Si heterojunction photovoltaic device, ACS Appl. Mater. Interfaces 10 (2018) 27454–27464, https://doi.org/10.1021/acsami.8b07001.
[179] D. Meza, A. Cruz, A.B. Morales-Vilches, L. Korte, B. Stannowski, Aluminum-doped zinc oxide as front electrode for rear emitter silicon heterojunction solar cells with high efficiency, Appl. Sci. 9 (2019), https://doi.org/10.3390/app9050862.
[180] L.L. Senaud, G. Christmann, A. Descoeudres, J. Geissbühler, L. Barraud, N. Badel, C. Allebé, S. Nicolay, M. Despeisse, B. Paviet-Salomon, C. Ballif, Aluminium-doped zinc oxide rear reflectors for high-efficiency silicon heterojunction solar cells, IEEE J. Photovolt. 9 (2019) 1217–1224, https://doi.org/10.1109/JPHOTOV.2019.2926860.
[181] H. Li, W. Duan, A. Lambertz, J. Hüpkes, K. Ding, U. Rau, O. Astakhov, Influence of room temperature sputtered al-doped zinc oxide on passivation quality in silicon heterojunction solar cells, IEEE J. Photovolt. 9 (2019) 1485–1491, https://doi.org/10.1109/JPHOTOV.2019.2933185.
[182] H. Park, Y. Lee, S.J. Park, S. Bae, S. Kim, D. Oh, J. Park, Y. Kim, H. Guim, Y. Kang, H.-S. Lee, D. Kim, J. Yi, Tunnel oxide passivating electron contacts for high-efficiency n-type silicon solar cells with amorphous silicon passivating hole contacts, Prog. Photovolt.: Res. Appl. 27 (2019) 1104–1114, https://doi.org/10.1002/pip.3190.
[183] C. Han, L. Mazzarella, Y. Zhao, G. Yang, P. Procel, M. Tijssen, A. Montes, L. Spitaleri, A. Gulino, X. Zhang, O. Isabella, M. Zeman, High-mobility hydrogenated fluorine-doped indium oxide film for passivating contacts c-Si solar cells, ACS Appl. Mater. Interfaces 11 (2019) 45586–45595, https://doi.org/10.1021/acsami.9b14709.
[184] H. Li, S. Yin, G. Dong, G. Cui, C. Lei, Y. Li, X. Xu, L. Feng, J. Zhang, C. Yu, Effect of humidity on optical and electrical properties of Zr-doped In2O3 and a new structure for transparent electrode of silicon heterojunction solar cell, Sol. Energy 196 (2020) 125–131, https://doi.org/10.1016/j.solener.2019.12.017.
[185] M. Köhler, M. Pomaska, A. Zamchiy, A. Lambertz, W. Duan, F. Lentz, S. Li, V. Smirnov, T. Kirchartz, F. Finger, U. Rau, K. Ding, Optimization of transparent passivating contact for crystalline silicon solar cells, IEEE J. Photovolt. 10 (2020) 46–53, https://doi.org/10.1109/JPHOTOV.2019.2947131.
[186] Z. Zhou, Y. Zhang, X. Chen, S. Li, Y. Zhao, X. Zhang, Innovative wide-spectrum Mg and Ga-codoped ZnO transparent conductive films grown via reactive plasma deposition for si heterojunction solar cells, ACS Appl. Energy Mater. 3 (2020) 1574–1584, https://doi.org/10.1021/acsaem.9b02064.
[187] N. Selmane, A. Cheknane, H.S. Hilal, Optimization of Al-doped ZnO transparent conducting oxide and emitter layers for enhanced performance of Si heterojunction solar cells, J. Electron. Mater. 49 (2020) 2179–2190, https://doi.org/10.1007/s11664-019-07917-w.
[188] Y. Zhao, L. Mazzarella, P. Procel, C. Han, G. Yang, A. Weeber, M. Zeman, O. Isabella, Doped hydrogenated nanocrystalline silicon oxide layers for high-efficiency c-Si heterojunction solar cells, Prog. Photovolt.: Res. Appl. 28 (2020) 425–435, https://doi.org/10.1002/pip.3256.
[189] C. Lei, C.-W. Peng, J. Zhong, H. Li, M. Yang, K. Zheng, X. Qu, L. wu, C. Yu, Y. Li, X. Xu, Phosphorus treatment to promote crystallinity of the microcrystalline silicon front contact layers for highly efficient heterojunction solar cells, Sol. Energy Mater. Sol. Cells 209 (2020) 110439, https://doi.org/10.1016/j.solmat.2020.110439.
[190] D. Qiu, W. Duan, A. Lambertz, K. Bittkau, P. Steuter, Y. Liu, A. Gad, M. Pomaska, U. Rau, K. Ding, Front contact optimization for rear-junction SHJ solar cells with ultra-thin n-type nanocrystalline silicon oxide, Sol. Energy Mater. Sol. Cells 209 (2020) 110471, https://doi.org/10.1016/j.solmat.2020.110471.
[191] S. Lee, D.P. Pham, Y. Kim, E.-C. Cho, J. Park, J. Yi, Influence of the Carrier Selective Front Contact Layer and Defect State of a-Si:H/c-Si Interface on the Rear Emitter Silicon Heterojunction Solar Cells, Energies 13 (2020), https://doi.org/10.3390/en13112948.
[192] M.Q. Khokhar, S.Q. Hussain, D.P. Pham, H. Park, I. Sultana, A. Razaq, G. T. Chavan, Y. Kim, E.C. Cho, J. Yi, ITO: Zr bi-layers deposited by reactive O2 and Ar plasma with high work function for silicon heterojunction solar cells, Curr. Appl. Phys. 20 (2020) 994–1000, https://doi.org/10.1016/j.cap.2020.06.006.
[193] P. Wyss, J. Stuckelberger, G. Nogay, J. Horzel, Q. Jeangros, I. Mack, M. Lehmann, X. Niquille, C. Allebé, M. Despeisse, F.J. Haug, A. Ingenito, P. Löper, C. Ballif, A mixed-phase SiOx hole selective junction compatible with high temperatures used in industrial solar cell manufacturing, IEEE J. Photovolt. 10 (2020) 1262–1269, https://doi.org/10.1109/JPHOTOV.2020.3006979.
[194] J. Schube, L. Tutsch, T. Fellmeth, F. Feldmann, M. Weil, A. Harter, J.-I. Polzin, M. Bivour, R. Keding, S.W. Glunz, Intense pulsed light in back end processing of solar cells with passivating contacts based on amorphous or polycrystalline silicon layers, Sol. Energy Mater. Sol. Cells 216 (2020) 110711, https://doi.org/10.1016/j.solmat.2020.110711.
[195] J. Sutter, D. Eisenhauer, P. Wagner, A.B. Morales Vilches, B. Rech, B. Stannowski, C. Becker, Tailored nanostructures for light management in silicon heterojunction solar cells, Sol. RRL 4 (2020) 2000484, https://doi.org/10.1002/solr.202000484.
[196] Y. Liu, M. Pomaska, W. Duan, D. Qiu, S. Li, A. Lambertz, A. Gad, U. Breuer, F. Finger, U. Rau, K. Ding, Phosphorus catalytic doping on intrinsic silicon thin films for the application in silicon heterojunction solar cells, ACS Appl. Mater. Interfaces 12 (2020) 56615–56621, https://doi.org/10.1021/acsami.0c17416.
[197] Y. Zhao, P. Procel, C. Han, L. Mazzarella, G. Yang, A. Weeber, M. Zeman, O. Isabella, Design and optimization of hole collectors based on nc-SiOx:H for high-efficiency silicon heterojunction solar cells, Sol. Energy Mater. Sol. Cells 219 (2021) 110779, https://doi.org/10.1016/j.solmat.2020.110779.
[198] Z. Yao, W. Duan, P. Steuter, J. Hüpkes, A. Lambertz, K. Bittkau, M. Pomaska, D. Qiu, K. Qiu, Z. Wu, H. Shen, U. Rau, K. Ding, Influence of oxygen on sputtered titanium-doped indium oxide thin films and their application in silicon heterojunction solar cells, Sol. RRL 5 (2021) 2000501, https://doi.org/10.1002/solr.202000501.
[199] H. Umishio, H. Sai, T. Koida, T. Matsui, Nanocrystalline-silicon hole contact layers enabling efficiency improvement of silicon heterojunction solar cells: Impact of nanostructure evolution on solar cell performance, Prog. Photovolt.: Res. Appl. 29 (2021) 344–356, https://doi.org/10.1002/pip.3368.
[200] Z. Wu, W. Duan, A. Lambertz, D. Qiu, M. Pomaska, Z. Yao, U. Rau, L. Zhang, Z. Liu, K. Ding, Low-resistivity p-type a-Si:H/AZO hole contact in high-efficiency silicon heterojunction solar cells, Appl. Surf. Sci. 542 (2021) 148749, https://doi.org/10.1016/j.apsusc.2020.148749.
[201] H. Sai, H.-J. Hsu, P.-W. Chen, P.-L. Chen, T. Matsui, Intrinsic amorphous silicon bilayers for effective surface passivation in silicon heterojunction solar cells: a comparative study of interfacial layers, Phys. Status Solidi (a) 218 (2021) 2000743, https://doi.org/10.1002/pssa.202000743.
[202] S. Li, M. Pomaska, A. Lambertz, W. Duan, K. Bittkau, D. Qiu, Z. Yao, M. Luysberg, P. Steuter, M. Köhler, K. Qiu, R. Hong, H. Shen, F. Finger, T. Kirchartz, U. Rau, K. Ding, Transparent-conductive-oxide-free front contacts for high-efficiency silicon heterojunction solar cells, Joule 5 (2021) 1535–1547, https://doi.org/10.1016/j.joule.2021.04.004.
[203] D.P. Pham, S. Lee, Y. Kim, J. Yi, Band-offset reduction for effective hole carrier collection in bifacial silicon heterojunction solar cells, J. Phys. Chem. Solids 154 (2021) 110059, https://doi.org/10.1016/j.jpcs.2021.110059.
[204] P. Wagner, A. Cruz, J.C. Stang, L. Korte, Low-resistance hole contact stacks for interdigitated rear-contact silicon heterojunction solar cells, IEEE J. Photovolt. 11 (2021) 914–925, https://doi.org/10.1109/JPHOTOV.2021.3074031.
[205] C. Han, Y. Zhao, L. Mazzarella, R. Santbergen, A. Montes, P. Procel, G. Yang, X. Zhang, M. Zeman, O. Isabella, Room-temperature sputtered tungsten-doped

indium oxide for improved current in silicon heterojunction solar cells, Sol. Energy Mater. Sol. Cells 227 (2021) 111082, https://doi.org/10.1016/j.solmat.2021.111082.
[206] D. Qiu, W. Duan, A. Lambertz, Z. Wu, K. Bittkau, K. Qiu, Z. Yao, U. Rau, K. Ding, Function analysis of the phosphine gas flow for n-type nanocrystalline silicon oxide layer in silicon heterojunction solar cells, ACS Appl. Energy Mater. 4 (2021) 7544–7551, https://doi.org/10.1021/acsaem.1c00654.
[207] W. Huang, J. Shi, Y. Liu, Z. Wu, F. Meng, Z. Liu, High-performance Ti and W co-doped indium oxide films for silicon heterojunction solar cells prepared by reactive plasma deposition, J. Power Sources 506 (2021) 230101, https://doi.org/10.1016/j.jpowsour.2021.230101.
[208] J. Zhou, B. Zhang, J. Chen, H. Ren, Q. Huang, X. Zhang, G. Hou, Y. Zhao, Performance improvement of planar silicon heterojunction solar cells via sandwich-like p-type emitters, Appl. Phys. A 127 (2021) 735, https://doi.org/10.1007/s00339-021-04883-1.
[209] H. Sai, H. Umishio, T. Matsui, Very thin (56 μm) silicon heterojunction solar cells with an efficiency of 23.3% and an open-circuit voltage of 754 mV, Sol. RRL 5 (2021) 2100634, https://doi.org/10.1002/solr.202100634.
[210] M.Q. Khokhar, S.Q. Hussain, S. Chowdhury, M.A. Zahid, D.P. Pham, S. Jeong, S. Kim, S. Kim, E.-C. Cho, J. Yi, High-efficiency hybrid solar cell with a nanocrystalline silicon oxide layer as an electron-selective contact, Energy Convers. Manag. 252 (2022) 115033, https://doi.org/10.1016/j.enconman.2021.115033.
[211] Y. Yang, W. Liu, L. Zhang, S. Huang, X. Li, K. Jiang, Z. Li, Z. Yan, S. Lan, X. Wu, Z. Ma, Y. Zhou, Z. Liu, N-type nc-SiOx:H film enables efficient and stable silicon heterojunction solar cells in sodium environment, Mater. Lett. 309 (2022) 131360, https://doi.org/10.1016/j.matlet.2021.131360.
[212] A. Cruz, D. Erfurt, P. Wagner, A.B. Morales-Vilches, F. Ruske, R. Schlatmann, B. Stannowski, Optoelectrical analysis of TCO+Silicon oxide double layers at the front and rear side of silicon heterojunction solar cells, Sol. Energy Mater. Sol. Cells 236 (2022) 111493, https://doi.org/10.1016/j.solmat.2021.111493.
[213] Y. Zhao, L. Mazzarella, P. Procel, C. Han, F.D. Tichelaar, G. Yang, A. Weeber, M. Zeman, O. Isabella, Ultra-thin electron collectors based on nc-Si:H for high-efficiency silicon heterojunction solar cells, Prog. Photovolt.: Res. Appl. 30 (2022) 809–822, https://doi.org/10.1002/pip.3502.
[214] D.P. Pham, J. Yi, Dopant-grading proposal for polysilicon passivating contact in crystalline silicon solar cells, J. Power Sources 522 (2022) 231005, https://doi.org/10.1016/j.jpowsour.2022.231005.
[215] M.A. Zahid, M.Q. Khokhar, S. Park, S.Q. Hussain, Y. Kim, J. Yi, Influence of Al2O3/IZO double-layer antireflective coating on the front side of rear emitter silicon heterojunction solar cell, Vacuum 200 (2022) 110967, https://doi.org/10.1016/j.vacuum.2022.110967.
[216] C. Han, R. Santbergen, M. van Duffelen, P. Procel, Y. Zhao, G. Yang, X. Zhang, M. Zeman, L. Mazzarella, O. Isabella, Towards bifacial silicon heterojunction solar cells with reduced TCO use, Prog. Photovolt.: Res. Appl. 30 (2022) 750–762, https://doi.org/10.1002/pip.3550.
[217] E. Donercark, S. Guler, E. Hande Ciftpinar, I. Kabacelik, M. Koc, A. Cigdem Ercelebi, R. Turan, Impact of oxygen partial pressure during Indium Tin Oxide sputtering on the performance of silicon heterojunction solar cells, Mater. Sci. Eng.: B 281 (2022) 115750, https://doi.org/10.1016/j.mseb.2022.115750.
[218] G. Dong, J. Li, Y. Zhao, X. Ran, C.-W. Peng, D. He, C. Jin, Q. Wang, H. Jiang, Y. Zhang, X. Cao, C. Yu, Highly efficient silicon heterojunction solar cells with ZnO:Al transparent electrode and transition metal doped indium oxide interfacial layer, Prog. Photovolt.: Res. Appl. 31 (2023) 931–938, https://doi.org/10.1002/pip.3697.
[219] D. Qiu, W. Duan, A. Lambertz, A. Eberst, K. Bittkau, U. Rau, K. Ding, Transparent conductive oxide sputtering damage on contact passivation in silicon heterojunction solar cells with hydrogenated nanocrystalline silicon, Sol. RRL 6 (2022) 2200651, https://doi.org/10.1002/solr.202200651.
[220] D.P. Pham, D. Oh, V.-A. Dao, Y. Kim, J. Yi, Enhanced energy conversion performance of silicon solar cells by quantum-confinement effect of polysilicon oxide, Appl. Mater. Today 29 (2022) 101604, https://doi.org/10.1016/j.apmt.2022.101604.
[221] H. Du, T. Wang, Y. Zeng, Z. Yang, W. Yang, M. Liao, J. Sheng, J. Ye, Improved contact quality for silver-free silicon heterojunction solar cells by phosphoric acid treatment, Sol. Energy 252 (2023) 1–7, https://doi.org/10.1016/j.solener.2023.01.048.
[222] Z. Yan, J. Shi, S. Chen, J. Du, L. Zhang, Q. Yuan, C. Song, K. Jiang, Y. Yang, A. Han, Z. Liu, F. Meng, Ga-doped ZnO rear transparent contact enables high efficiency silicon heterojunction solar cells, Sol. Energy Mater. Sol. Cells 253 (2023) 112244, https://doi.org/10.1016/j.solmat.2023.112244.
[223] A. Soman, U.K. Das, S.S. Hegedus, Interface engineering by intermediate hydrogen plasma treatment using Dc-PECVD for silicon heterojunction solar cells, ACS Appl. Electron. Mater. 5 (2023) 803–811, https://doi.org/10.1021/acsaelm.2c01336.
[224] Q. Tang, W. Duan, A. Lambertz, K. Bittkau, M.A. Yaqin, Y. Zhao, K. Zhang, Q. Yang, D. Qiu, F. Gunkel, M. Weber, U. Rau, K. Ding, > 85% indium reduction for high-efficiency silicon heterojunction solar cells with aluminum-doped zinc oxide contacts, Sol. Energy Mater. Sol. Cells 251 (2023) 112120, https://doi.org/10.1016/j.solmat.2022.112120.
[225] Q. Qiu, Y. Bai, J. Li, C. Guo, H. Chen, H. Zhang, J. Shi, W. Liu, T. Chen, J. Liao, J. Yu, ZnO-Doped In2O3 Front Transparent Contact Enables >24.0% Silicon Heterojunction Solar Cells, Energy Technol. 11 (2023) 2201310, https://doi.org/10.1002/ente.202201310.
[226] H.T. Gebrewold, K. Bittkau, K. Qiu, U. Rau, K. Ding, Understanding silicon heterojunction solar cells with nc-SiC/SiO2 as an alternate transparent passivating front contact and computational design optimization, Sol. RRL 7 (2023) 2201051, https://doi.org/10.1002/solr.202201051.
[227] L. Liu, L. Jia, Y. Huang, Y. Zhang, W. Yu, High-performance vertical graphene nanowall/silicon Schottky junction solar cells with Nafion doping and plasma etching, J. Alloy. Compd. 939 (2023) 168765, https://doi.org/10.1016/j.jallcom.2023.168765.
[228] Z. Luo, C. Yang, X. Chen, W. Ma, S. Li, K. Fu, Improving open-circuit voltage and short-circuit current of high-efficiency silicon-based planar heterojunction solar cells by combining V2O5 with PEDOT:PSS, J. Mater. 9 (2023) 438–446, https://doi.org/10.1016/j.jmat.2022.12.008.
[229] M. Kumar, S. Kumar, 24.13% efficient TiO2/i–a–Si:H/p–c–Si heterojunction solar cell by AFORS-HET numerical simulation, Opt. Quantum Electron. 55 (2023) 441, https://doi.org/10.1007/s11082-023-04716-w.
[230] H. Lin, M. Yang, X. Ru, G. Wang, S. Yin, F. Peng, C. Hong, M. Qu, J. Lu, L. Fang, C. Han, P. Procel, O. Isabella, P. Gao, Z. Li, X. Xu, Silicon heterojunction solar cells with up to 26.81% efficiency achieved by electrically optimized nanocrystalline-silicon hole contact layers, Nat. Energy 8 (2023) 789–799, https://doi.org/10.1038/s41560-023-01255-2.
[231] J. Shang, Q. Wang, S. Zhou, Y. Zhou, Y. Zhou, F. Liu, High mobility hafnium and hydrogen Co-doped indium oxide transparent conductive films and application in high efficiency silicon heterojunction solar cell, J. Alloy. Compd. 952 (2023) 169919, https://doi.org/10.1016/j.jallcom.2023.169919.
[232] L. Wen, L. Zhao, G. Wang, X. Jia, X. Xu, S. Qu, X. Li, X. Zhang, K. Xin, J. Xiao, W. Wang, Beyond 25% efficient crystalline silicon heterojunction solar cells with hydrogenated amorphous silicon oxide stacked passivation layers for rear emitter, Sol. Energy Mater. Sol. Cells 258 (2023) 112429, https://doi.org/10.1016/j.solmat.2023.112429.
[233] D. Kocak, K. Tsoi, D. Turkay, M. Koc, E. Donercark, H. Budunoglu, S. Yerci, Silica aerogel as rear reflector in silicon heterojunction solar cells for improved infrared response, Sol. Energy Mater. Sol. Cells 258 (2023) 112430, https://doi.org/10.1016/j.solmat.2023.112430.
[234] M. Boccard, L. Antognini, J. Cattin, J. Dréon, W. Lin, V. Paratte, D. Turkay, C. Ballif, Loss analysis of a 24.4%-efficient front-junction silicon heterojunction solar cell and opportunity for localized contacts, IEEE J. Photovolt. 13 (2023) 663–671, https://doi.org/10.1109/JPHOTOV.2023.3291050.
[235] T. Koida, T. Matsui, H. Sai, Amorphous SnO2 as earth-abundant stable transparent conductive oxide and its application to si heterojunction solar cells, Sol. RRL 7 (2023) 2300381, https://doi.org/10.1002/solr.202300381.
[236] X. Huang, Y. Zhou, W. Guo, F. Liu, D. Zhao, R. Life, H. Huang, Z. Hao, Y. Zhou, Zr-doped indium oxide films for silicon heterojunction solar cells, Sol. Energy Mater. Sol. Cells 260 (2023) 112480, https://doi.org/10.1016/j.solmat.2023.112480.
[237] Z. Wang, Z. Liu, H. Lin, F. Ye, P. Gao, Hot wire Oxidation–Sublimation derived work function tunable WOx thin films for building hole-selective contacts, Mater. Today Energy 38 (2023) 101439, https://doi.org/10.1016/j.mtener.2023.101439.
[238] X. Wu, C. Sen, H. Wang, X. Wang, Y. Wu, M.U. Khan, L. Mao, F. Jiang, T. Xu, G. Zhang, B. Hoex, Addressing sodium ion-related degradation in SHJ cells by the application of nano-scale barrier layers, Sol. Energy Mater. Sol. Cells 264 (2024) 112604, https://doi.org/10.1016/j.solmat.2023.112604.
[239] Z. Yan, J. Shi, S. Chen, S. Huang, Y. Luo, J. Ren, J. Du, Z. Li, G. Wang, A. Han, D. Zhao, X. Yu, H. Huang, R. Li, H. Fu, B. Fan, L. Zhang, W. Liu, Z. Liu, F. Meng, Gallium-doped zinc oxide/tungsten-doped indium oxide stacks with enhanced lateral transport capability for efficient and low-cost silicon heterojunction solar cells, Sol. RRL 8 (2024) 2301029, https://doi.org/10.1002/solr.202301029.
[240] W. Duan, G. Mains, H.T. Gebrewold, K. Bittkau, A. Lambertz, B. Xu, V. Lauterbach, A. Eberst, N. Nicholson, L. Korte, M.A. Yaqin, K. Zhang, Q. Yang, U. Rau, K. Ding, Enhancing the selectivity and transparency of the electron contact in silicon heterojunction solar cells by phosphorus catalytic doping, Adv. Funct. Mater. 34 (2024) 2310552, https://doi.org/10.1002/adfm.202310552.
[241] J. Bullock, Y. Wan, M. Hettick, X. Zhaoran, S.P. Phang, D. Yan, H. Wang, W. Ji, C. Samundsett, Z. Hameiri, D. Macdonald, A. Cuevas, A. Javey, Dopant-free partial rear contacts enabling 23% silicon solar cells, Adv. Energy Mater. 9 (2019) 1803367, https://doi.org/10.1002/aenm.201803367.
[242] L.G. Gerling, S. Mahato, A. Morales-Vilches, G. Masmitja, P. Ortega, C. Voz, R. Alcubilla, J. Puigdollers, Transition metal oxides as hole-selective contacts in silicon heterojunctions solar cells, Sol. Energy Mater. Sol. Cells 145 (2016) 109–115, https://doi.org/10.1016/j.solmat.2015.08.028.
[243] G. Masmitjà, P. Ortega, J. Puigdollers, L.G. Gerling, I. Martín, C. Voz, R. Alcubilla, Interdigitated back-contacted crystalline silicon solar cells with low-temperature dopant-free selective contacts, J. Mater. Chem. A 6 (2018) 3977–3985, https://doi.org/10.1039/C7TA11308K.
[244] J. Bullock, Y. Wan, Z. Xu, S. Essig, M. Hettick, H. Wang, W. Ji, M. Boccard, A. Cuevas, C. Ballif, A. Javey, Stable dopant-free asymmetric heterocontact silicon solar cells with efficiencies above 20%, ACS Energy Lett. 3 (2018) 508–513, https://doi.org/10.1021/acsenergylett.7b01279.
[245] H. Imran, T.M. Abdolkader, N.Z. Butt, Carrier-selective NiO/Si and TiO2/Si contacts for silicon heterojunction solar cells, IEEE Trans. Electron Devices 63 (2016) 3584–3590.
[246] A. Tyagi, K. Ghosh, A. Kottantharayil, S. Lodha, Performance evaluation of passivated silicon carrier-selective contact solar cell, IEEE Trans. Electron Devices 65 (2018) 176–183, https://doi.org/10.1109/TED.2017.2771816.
[247] C. Yu, S. Xu, J. Yao, S. Han, Recent advances in and new perspectives on crystalline silicon solar cells with carrier-selective passivation contacts, Crystals 8 (2018), https://doi.org/10.3390/cryst8110430.
[248] M.T. Greiner, L. Chai, M.G. Helander, W.-M. Tang, Z.-H. Lu, Transition metal oxide work functions: the influence of cation oxidation state and oxygen

vacancies, Adv. Funct. Mater. 22 (2012) 4557–4568, https://doi.org/10.1002/adfm.201200615.
[249] M.T. Greiner, M.G. Helander, W.-M. Tang, Z.-B. Wang, J. Qiu, Z.-H. Lu, Universal energy-level alignment of molecules on metal oxides, Nat. Mater. 11 (2012) 76–81, https://doi.org/10.1038/nmat3159.
[250] S.-Y. Lin, Y.-C. Chen, C.-M. Wang, P.-T. Hsieh, S.-C. Shih, Post-annealing effect upon optical properties of electron beam evaporated molybdenum oxide thin films, Appl. Surf. Sci. 255 (2009) 3868–3874, https://doi.org/10.1016/j.apsusc.2008.10.069.
[251] M. Mews, L. Korte, B. Rech, Oxygen vacancies in tungsten oxide and their influence on tungsten oxide/silicon heterojunction solar cells, Sol. Energy Mater. Sol. Cells 158 (2016) 77–83, https://doi.org/10.1016/j.solmat.2016.05.042.
[252] M. Kumar, E.-C. Cho, M.F. Prodanov, C. Kang, A.K. Srivastava, J. Yi, MoOx work function, interface structure, and thermal stability analysis of ITO/MoOx/a-Si(i) stacks for hole-selective silicon heterojunction solar cells, Appl. Surf. Sci. 553 (2021) 149552, https://doi.org/10.1016/j.apsusc.2021.149552.
[253] X. Yang, Q. Bi, H. Ali, K. Davis, W.V. Schoenfeld, K. Weber, High-performance TiO2-based electron-selective contacts for crystalline silicon solar cells, Adv. Mater. 28 (2016) 5891–5897, https://doi.org/10.1002/adma.201600926.
[254] J. Bullock, M. Hettick, J. Geissbühler, A.J. Ong, T. Allen, Carolin M. Sutter-Fella, T. Chen, H. Ota, E.W. Schaler, S. De Wolf, C. Ballif, A. Cuevas, A. Javey, Efficient silicon solar cells with dopant-free asymmetric heterocontacts, Nat. Energy 1 (2016) 15031, https://doi.org/10.1038/nenergy.2015.31.
[255] Y. Wang, C. Zhu, R. Pfattner, H. Yan, L. Jin, S. Chen, F. Molina-Lopez, F. Lissel, J. Liu, N.I. Rabiah, Z. Chen, J.W. Chung, C. Linder, M.F. Toney, B. Murmann, Z. Bao, A highly stretchable, transparent, and conductive polymer, Science Advances 3 e1602076. https://doi.org/10.1126/sciadv.1602076.
[256] H. Mehmood, H. Nasser, T. Tauqeer, R. Turan, Simulation of silicon heterostructure solar cell featuring dopant-free carrier-selective molybdenum oxide and titanium oxide contacts, Renew. Energy 143 (2019) 359–367, https://doi.org/10.1016/j.renene.2019.05.007.
[257] X. Yin, C. Battaglia, Y. Lin, K. Chen, M. Hettick, M. Zheng, C.-Y. Chen, D. Kiriya, A. Javey, 19.2% efficient InP heterojunction solar cell with electron-selective TiO2 contact, ACS Photonics 1 (2014) 1245–1250, https://doi.org/10.1021/ph500153c.
[258] H. Wu, L.S. Wang, Electronic structure of titanium oxide clusters: TiOy (y = 1−3) and (TiO2)n (n = 1−4), J. Chem. Phys. 107 (1997) 8221–8228, https://doi.org/10.1063/1.475026.
[259] W.-D. Zhu, C.-W. Wang, J.-B. Chen, D.-S. Li, F. Zhou, H.-L. Zhang, Enhanced field emission from hydrogenated TiO2 nanotube arrays, Nanotechnology 23 (2012) 455204, https://doi.org/10.1088/0957-4484/23/45/455204.
[260] R.A. Vijayan, S. Masilamani, S. Kailasam, K. Shivam, B. Deenadhayalan, M. Varadharajaperumal, Study of surface passivation and charge transport barriers in DASH solar cell, IEEE J. Photovolt. 9 (2019) 1208–1216, https://doi.org/10.1109/JPHOTOV.2019.2926624.
[261] H. Mehmood, H. Nasser, E. Özkol, T. Tauqeer, S. Hussain, R. Turan, Physical device simulation of partial dopant-free asymmetric silicon heterostructure solar cell (P-DASH) based on hole-selective Molybdenum oxide (MoOx) with Crystalline Silicon (cSi), 2017 Int. Conf. Eng. Technol. (ICET) (2017) 1–6.
[262] C. Battaglia, X. Yin, M. Zheng, I.D. Sharp, T. Chen, S. McDonnell, A. Azcatl, C. Carraro, B. Ma, R. Maboudian, R.M. Wallace, A. Javey, Hole Selective MoOx Contact for Silicon Solar Cells, Nano Lett. 14 (2014) 967–971, https://doi.org/10.1021/nl404389u.
[263] G. Gregory, M. Wilson, H. Ali, K.O. Davis, Thermally stable molybdenum oxide hole-selective contacts deposited using spatial atomic layer deposition, 2018 IEEE 7th World Conf. Photovolt. Energy Convers. (WCPEC) (A Jt. Conf. 45th IEEE PVSC, 28th PVSEC 34th EU PVSEC) (2018) 2006–2009.
[264] S. Avasthi, W.E. McClain, G. Man, A. Kahn, J. Schwartz, J.C. Sturm, Hole-blocking titanium-oxide/silicon heterojunction and its application to photovoltaics, Appl. Phys. Lett. 102 (2013) 203901, https://doi.org/10.1063/1.4803446.
[265] J. Cho, J. Melskens, M. Debucquoy, M. Recamán Payo, S. Jambaldinni, T. Bearda, I. Gordon, J. Szlufcik, W.M.M. Kessels, J. Poortmans, Passivating electron-selective contacts for silicon solar cells based on an a-Si:H/TiOx stack and a low work function metal, Prog. Photovolt.: Res. Appl. 26 (2018) 835–845, https://doi.org/10.1002/pip.3023.
[266] X. Yang, K. Weber, Z. Hameiri, S. De Wolf, Industrially feasible, dopant-free, carrier-selective contacts for high-efficiency silicon solar cells, Prog. Photovolt. Res. Appl. 25 (2017) 896–904, https://doi.org/10.1002/pip.2901.
[267] H. Ali, X. Yang, K. Weber, W.V. Schoenfeld, K.O. Davis, Transmission electron microscopy studies of electron-selective titanium oxide contacts in silicon solar cells, Microsc. Microanal. 23 (2017) 900–904, https://doi.org/10.1017/S1431927617012417.
[268] M. Boccard, X. Yang, K. Weber, Z.C. Holman, Passivation and carrier selectivity of TiO2 contacts combined with different passivation layers and electrodes for silicon solar cells, 2016 IEEE 43rd Photovolt. Spec. Conf. (PVSC) (2016) 2403–2407.
[269] T.G. Allen, J. Bullock, Q. Jeangros, C. Samundsett, Y. Wan, J. Cui, A. Hessler-Wyser, S. De Wolf, A. Javey, A. Cuevas, A low resistance calcium/reduced titania passivated contact for high efficiency crystalline silicon solar cells, Adv. Energy Mater. 7 (2017) 1602606, https://doi.org/10.1002/aenm.201602606.
[270] J. Cho, J. Melskens, M.R. Payo, M. Debucquoy, H.S. Radhakrishnan, I. Gordon, J. Szlufcik, W.M.M. Kessels, J. Poortmans, Performance and thermal stability of an a-Si:H/TiOx/Yb stack as an electron-selective contact in silicon heterojunction solar cells, ACS Appl. Energy Mater. 2 (2019) 1393–1404, https://doi.org/10.1021/acsaem.8b01969.
[271] S. Il Park, S. Jae Baik, J.-S. Im, L. Fang, J.-W. Jeon, K. Su Lim, Towards a high efficiency amorphous silicon solar cell using molybdenum oxide as a window layer instead of conventional p-type amorphous silicon carbide, Appl. Phys. Lett. 99 (2011) 063504, https://doi.org/10.1063/1.3624591.
[272] C. Battaglia, S.M. de Nicolás, S. De Wolf, X. Yin, M. Zheng, C. Ballif, A. Javey, Silicon heterojunction solar cell with passivated hole selective MoOx contact, Appl. Phys. Lett. 104 (2014) 113902, https://doi.org/10.1063/1.4868880.
[273] C. Battaglia, S.Md Nicolás, Sd Wolf, X. Yin, M. Zheng, C. Ballif, A. Javey, Hole selective MoOx contact for silicon heterojunction solar cells, 2014 IEEE 40th Photovolt. Spec. Conf. (PVSC) (2014) 0968–0970.
[274] J. Cho, N. Nawal, A. Hadipour, M. Recaman Payo, A. van der Heide, H. S. Radhakrishnan, M. Debucquoy, I. Gordon, J. Szlufcik, J. Poortmans, Interface analysis and intrinsic thermal stability of MoOx based hole-selective contacts for silicon heterojunction solar cells, Sol. Energy Mater. Sol. Cells 201 (2019) 110074, https://doi.org/10.1016/j.solmat.2019.110074.
[275] S.Q. Hussain, K. Mallem, Y.J. Kim, A.H. Tuan Le, M.Q. Khokhar, S. Kim, S. Dutta, S. Sanyal, Y. Kim, J. Park, Y. Lee, Young H. Cho, Eun C. Cho, J. Yi, Ambient annealing influence on surface passivation and stoichiometric analysis of molybdenum oxide layer for carrier selective contact solar cells, Mater. Sci. Semicond. Process. 91 (2019) 267–274, https://doi.org/10.1016/j.mssp.2018.11.028.
[276] K. Mallem, Y.J. Kim, S.Q. Hussain, S. Dutta, A.H.T. Le, M. Ju, J. Park, Y.H. Cho, Y. Kim, E.-C. Cho, J. Yi, Molybdenum oxide: a superior hole extraction layer for replacing p-type hydrogenated amorphous silicon with high efficiency heterojunction Si solar cells, Mater. Res. Bull. 110 (2019) 90–96, https://doi.org/10.1016/j.materresbull.2018.10.018.
[277] J. Shi, L. Shen, Y. Liu, J. Yu, J. Liu, L. Zhang, Y. Liu, J. Bian, Z. Liu, F. Meng, MoOx modified ITO/a-Si:H(p) contact for silicon heterojunction solar cell application, Mater. Res. Bull. 97 (2018) 176–181, https://doi.org/10.1016/j.materresbull.2017.09.005.
[278] J. Geissbühler, J. Werner, S. Martin de Nicolas, L. Barraud, A. Hessler-Wyser, M. Despeisse, S. Nicolay, A. Tomasi, B. Niesen, S. De Wolf, C. Ballif, 22.5% efficient silicon heterojunction solar cell with molybdenum oxide hole collector, Appl. Phys. Lett. 107 (2015) 081601, https://doi.org/10.1063/1.4928747.
[279] L. Cao, P. Procel, A. Alcañiz, J. Yan, F. Tichelaar, E. Özkol, Y. Zhao, C. Han, G. Yang, Z. Yao, M. Zeman, R. Santbergen, L. Mazzarella, O. Isabella, 2023, , Achieving 23.83% conversion efficiency in silicon heterojunction solar cell with ultra-thin MoOx hole collector layer via tailoring (i)a-Si:H/MoOx interface 311245–1254, 10.1002/pip.3638.
[280] I. Irfan, A. James Turinske, Z. Bao, Y. Gao, Work function recovery of air exposed molybdenum oxide thin films, Appl. Phys. Lett. 101 (2012) 093305, https://doi.org/10.1063/1.4748978.
[281] J. Meyer, A. Shu, M. Kröger, A. Kahn, Effect of contamination on the electronic structure and hole-injection properties of MoO3/organic semiconductor interfaces, Appl. Phys. Lett. 96 (2010) 133308, https://doi.org/10.1063/1.3374333.
[282] T. Zhang, C.-Y. Lee, Y. Wan, S. Lim, B. Hoex, Investigation of the thermal stability of MoOx as hole-selective contacts for Si solar cells, J. Appl. Phys. 124 (2018), https://doi.org/10.1063/1.5041774.
[283] S. Essig, J. Dréon, E. Rucavado, M. Mews, T. Koida, M. Boccard, J. Werner, J. Geissbühler, P. Löper, M. Morales-Masis, L. Korte, S. De Wolf, C. Ballif, Toward annealing-stable molybdenum-oxide-based hole-selective contacts for silicon photovoltaics, Sol. RRL 2 (2018) 1700227, https://doi.org/10.1002/solr.201700227.
[284] S.Q. Hussain, S. Kim, S. Ahn, H. Park, A.H.T. Le, S. Lee, Y. Lee, J.H. Lee, J. Yi, RF magnetron sputtered ITO:Zr thin films for the high efficiency a-Si:H/c-Si heterojunction solar cells, Met. Mater. Int. 20 (2014) 565–569, https://doi.org/10.1007/s12540-014-3001-x.
[285] R. Liu, S.-T. Lee, B. Sun, 13.8% efficiency hybrid Si/organic heterojunction solar cells with MoO3 film as antireflection and inversion induced layer, Adv. Mater. 26 (2014) 6007–6012, https://doi.org/10.1002/adma.201402076.
[286] W. Wu, J. Bao, X. Jia, Z. Liu, L. Cai, B. Liu, J. Song, H. Shen, Dopant-free back contact silicon heterojunction solar cells employing transition metal oxide emitters, Phys. Status Solidi (RRL) – Rapid Res. Lett. 10 (2016) 662–667, https://doi.org/10.1002/pssr.201600254.
[287] I.Y.-y Bu, S. Chen, Improved crystalline silicon solar cells by light harvesting zinc oxide nanowire arrays, Optik 127 (2016) 10355–10359, https://doi.org/10.1016/j.ijleo.2016.08.056.
[288] Y. Liu, J. Zhang, H. Wu, W. Cui, R. Wang, K. Ding, S.-T. Lee, B. Sun, Low-temperature synthesis TiOx passivation layer for organic-silicon heterojunction solar cell with a high open-circuit voltage, Nano Energy 34 (2017) 257–263, https://doi.org/10.1016/j.nanoen.2017.02.024.
[289] O. Almora, L.G. Gerling, C. Voz, R. Alcubilla, J. Puigdollers, G. Garcia-Belmonte, Superior performance of V2O5 as hole selective contact over other transition metal oxides in silicon heterojunction solar cells, Sol. Energy Mater. Sol. Cells 168 (2017) 221–226, https://doi.org/10.1016/j.solmat.2017.04.042.
[290] F. Wang, S. Zhao, B. Liu, Y. Li, Q. Ren, R. Du, N. Wang, C. Wei, X. Chen, G. Wang, B. Yan, Y. Zhao, X. Zhang, Silicon solar cells with bifacial metal oxides carrier selective layers, Nano Energy 39 (2017) 437–443, https://doi.org/10.1016/j.nanoen.2017.07.014.
[291] R. Pietruszka, B.S. Witkowski, E. Zielony, K. Gwozdz, E. Placzek-Popko, M. Godlewski, ZnO/Si heterojunction solar cell fabricated by atomic layer deposition and hydrothermal methods, Sol. Energy 155 (2017) 1282–1288, https://doi.org/10.1016/j.solener.2017.07.071.

[292] M. Mews, A. Lemaire, L. Korte, Sputtered tungsten oxide as hole contact for silicon heterojunction solar cells, IEEE J. Photovolt. 7 (2017) 1209–1215, https://doi.org/10.1109/JPHOTOV.2017.2714193.
[293] D. Sacchetto, Q. Jeangros, G. Christmann, L. Barraud, A. Descoeudres, J. Geissbühler, M. Despeisse, A. Hessler-Wyser, S. Nicolay, C. Ballif, ITO/MoOx/a-Si:H(i) hole-selective contacts for silicon heterojunction solar cells: degradation mechanisms and cell integration, IEEE J. Photovolt. 7 (2017) 1584–1590, https://doi.org/10.1109/JPHOTOV.2017.2756066.
[294] J. He, Z. Ling, P. Gao, J. Ye, TiO2 films from the low-temperature oxidation of Ti as passivating-contact layers for Si heterojunction solar cells, Sol. RRL 1 (2017) 1700154, https://doi.org/10.1002/solr.201700154.
[295] Z. Liu, Z. Yang, S. Wu, J. Zhu, W. Guo, J. Sheng, J. Ye, Y. Cui, Photoinduced field-effect passivation from negative carrier accumulation for high-efficiency silicon/organic heterojunction solar cells, ACS Nano 11 (2017) 12687–12695, https://doi.org/10.1021/acsnano.7b07222.
[296] Z. Yang, P. Gao, J. Sheng, H. Tong, C. Quan, X. Yang, K.W.A. Chee, B. Yan, Y. Zeng, J. Ye, Principles of dopant-free electron-selective contacts based on tunnel oxide/low work-function metal stacks and their applications in heterojunction solar cells, Nano Energy 46 (2018) 133–140, https://doi.org/10.1016/j.nanoen.2018.01.043.
[297] S. Masudy-Panah, S. Zhuk, H.R. Tan, X. Gong, G.K. Dalapati, Palladium nanostructure incorporated cupric oxide thin film with strong optical absorption, compatible charge collection and low recombination loss for low cost solar cell applications, Nano Energy 46 (2018) 158–167, https://doi.org/10.1016/j.nanoen.2018.01.050.
[298] P. Liu, P. Gao, X. Liu, H. Wang, J. He, X. Yang, Y. Zeng, B. Yan, J. Fang, J. Ye, High-performance organic-silicon heterojunction solar cells by using Al-doped ZnO as cathode interlayer, Sol. RRL 2 (2018) 1700223, https://doi.org/10.1002/solr.201700223.
[299] C. Zhang, E. Vadiee, R.R. King, C.B. Honsberg, Carrier-selective contact GaP/Si solar cells grown by molecular beam epitaxy, J. Mater. Res. 33 (2018) 414–423, https://doi.org/10.1557/jmr.2018.14.
[300] X. Yang, J. Guo, Y. Zhang, W. Liu, Y. Sun, Hole-selective NiO:Cu contact for NiO/Si heterojunction solar cells, J. Alloy. Compd. 747 (2018) 563–570, https://doi.org/10.1016/j.jallcom.2018.03.067.
[301] K. Qiu, Q. Xie, D. Qiu, L. Cai, W. Wu, W. Lin, Z. Yao, B. Ai, Z. Liang, H. Shen, Power-loss analysis of a dopant-free ZnS/p-Si heterojunction solar cell with WO3 as hole-selective contact, Sol. Energy 165 (2018) 35–42, https://doi.org/10.1016/j.solener.2018.02.076.
[302] X. Yang, W. Liu, J. Chen, Y. Sun, On the annealing-induced enhancement of the interface properties of NiO:Cu/wet-SiOx/n-Si tunnelling junction solar cells, Appl. Phys. Lett. 112 (2018) 173904, https://doi.org/10.1063/1.5026135.
[303] Z. Xia, P. Gao, T. Sun, H. Wu, Y. Tan, T. Song, S.-T. Lee, B. Sun, Buried MoOx/Ag electrode enables high-efficiency organic/silicon heterojunction solar cells with a high fill factor, ACS Appl. Mater. Interfaces 10 (2018) 13767–13773, https://doi.org/10.1021/acsami.8b02403.
[304] D. Banerjee, J.A. Benavides, X. Guo, S.G. Cloutier, Tailored interfaces of the bulk silicon nanowire/TiO2 heterojunction promoting enhanced photovoltaic performances, ACS Omega 3 (2018) 5064–5070, https://doi.org/10.1021/acsomega.8b00522.
[305] R. García-Hernansanz, E. García-Hemme, D. Montero, J. Olea, A. del Prado, I. Mártil, C. Voz, L.G. Gerling, J. Puigdollers, R. Alcubilla, Transport mechanisms in silicon heterojunction solar cells with molybdenum oxide as a hole transport layer, Sol. Energy Mater. Sol. Cells 185 (2018) 61–65, https://doi.org/10.1016/j.solmat.2018.05.019.
[306] J. Ding, Y. Zhou, G. Dong, M. Liu, D. Yu, F. Liu, Solution-processed ZnO as the efficient passivation and electron selective layer of silicon solar cells, Prog. Photovolt.: Res. Appl. 26 (2018) 974–980, https://doi.org/10.1002/pip.3044.
[307] F. Menchini, L. Serenelli, L. Martini, M. Izzi, G. Stracci, P. Mangiapane, E. Salza, M. Tucci, Transparent hole-collecting and buffer layers for heterojunction solar cells based on n-type-doped silicon, Appl. Phys. A 124 (2018) 489, https://doi.org/10.1007/s00339-018-1903-z.
[308] B. Gao, Y. Zhao, L. Cai, P. Liu, Z. Liang, H. Shen, Fabrication of cadmium sulfide/p type silicon heterojunction solar cells under 300 °C with more than 10% efficiency, Sol. Energy 173 (2018) 635–639, https://doi.org/10.1016/j.solener.2018.06.016.
[309] L. Chen, Z. Gao, Y. Zheng, M. Cui, H. Yan, D. Wei, S. Dou, J. Ji, E. Jia, N. Sang, K. Liu, X. Ding, Y. Li, M. Li, 14.1% efficiency hybrid planar-Si/organic heterojunction solar cells with SnO2 insertion layer, Sol. Energy 174 (2018) 549–555, https://doi.org/10.1016/j.solener.2018.09.035.
[310] F. Wang, Y. Zhang, M. Yang, L. Yang, Y. Sui, J. Yang, Y. Zhao, X. Zhang, Realization of 16.9% efficiency on nanowires heterojunction solar cells with dopant-free contact for bifacial polarities, Adv. Funct. Mater. 28 (2018) 1805001, https://doi.org/10.1002/adfm.201805001.
[311] Z. Wang, Y. Yang, L. Zhang, H. Lin, Z. Zhang, D. Wang, S. Peng, D. He, J. Ye, P. Gao, Modulation-doped ZnO as high performance electron-selective layer for efficient silicon heterojunction solar cells, Nano Energy 54 (2018) 99–105, https://doi.org/10.1016/j.nanoen.2018.10.010.
[312] H.T. Nguyen, E. Ros, T. Tom, J. Bertomeu, J.M. Asensi, J. Andreu, I.M. Garcia, P. Ortega, M. Garín, J. Puigdollers, C. Voz, R. Alcubilla, Influence of a gold seed in transparent V2Ox/Ag/V2Ox selective contacts for dopant-free silicon solar cells, IEEE J. Photovolt. 9 (2019) 72–77, https://doi.org/10.1109/JPHOTOV.2018.2875876.
[313] G. Ma, R. Du, Y.-n Cai, C. Shen, X. Gao, Y. Zhang, F. Liu, W. Shi, W. Du, Y. Zhang, Improved power conversion efficiency of silicon nanowire solar cells based on transition metal oxides, Sol. Energy Mater. Sol. Cells 193 (2019) 163–168, https://doi.org/10.1016/j.solmat.2019.01.010.
[314] K. Singh, M. Nayak, S. Mudgal, S. Singh, V.K. Komarala, Effect of textured silicon pyramids size and chemical polishing on the performance of carrier-selective contact heterojunction solar cells, Sol. Energy 183 (2019) 469–475, https://doi.org/10.1016/j.solener.2019.03.059.
[315] J.R. Sharma, G. Das, A.B. Roy, S. Bose, S. Mukhopadhyay, Design analysis of heterojunction solar cells with aligned AZO nanorods embedded in p-type Si wafer, Silicon 12 (2020) 305–316, https://doi.org/10.1007/s12633-019-00134-4.
[316] J. He, M.A. Hossain, H. Lin, W. Wang, S.K. Karuturi, B. Hoex, J. Ye, P. Gao, J. Bullock, Y. Wan, 15% efficiency ultrathin silicon solar cells with fluorine-doped titanium oxide and chemically tailored poly(3,4-ethylenedioxythiophene):poly(styrenesulfonate) as asymmetric heterocontact, ACS Nano 13 (2019) 6356–6362, https://doi.org/10.1021/acsnano.9b01754.
[317] J. Yu, M. Liao, D. Yan, Y. Wan, H. Lin, Z. Wang, P. Gao, Y. Zeng, B. Yan, J. Ye, Activating and optimizing evaporation-processed magnesium oxide passivating contact for silicon solar cells, Nano Energy 62 (2019) 181–188, https://doi.org/10.1016/j.nanoen.2019.05.015.
[318] L. Cai, W. Wang, L. Jin, Z. Yao, W. Lin, L. Meng, B. Ai, Z. Liang, Y. Huang, F. Zhang, P.P. Altermatt, H. Shen, 12.29% low temperature–processed dopant-free CdS/p-Si heterojunction solar cells, Adv. Mater. Interfaces 6 (2019) 1900367, https://doi.org/10.1002/admi.201900367.
[319] M. Liu, Y. Zhou, G. Dong, W. Wang, J. Wang, C. Liu, F. Liu, D. Yu, SnO2/Mg combination electron selective transport layer for Si heterojunction solar cells, Sol. Energy Mater. Sol. Cells 200 (2019) 109996, https://doi.org/10.1016/j.solmat.2019.109996.
[320] C. Lu, Rusli, A.B. Prakoso, Z. Li, Investigation of solution processed molybdenum oxide as selective contacts for silicon solar cells application, Mater. Chem. Phys. 236 (2019) 121779, https://doi.org/10.1016/j.matchemphys.2019.121779.
[321] H. Dai, L. Yang, S. He, < 50-μm thin crystalline silicon heterojunction solar cells with dopant-free carrier-selective contacts, Nano Energy 64 (2019) 103930, https://doi.org/10.1016/j.nanoen.2019.103930.
[322] S. Cao, J. Li, Y. Lin, T. Pan, G. Du, J. Zhang, L. Yang, X. Chen, L. Lu, N. Min, M. Yin, D. Li, Interfacial behavior and stability analysis of p-type crystalline silicon solar cells based on hole-selective MoOX/metal contacts, Sol. RRL 3 (2019) 1900274, https://doi.org/10.1002/solr.201900274.
[323] M. Nayak, S. Mandal, A. Pandey, S. Mudgal, S. Singh, V.K. Komarala, Nickel oxide hole-selective heterocontact for silicon solar cells: role of SiOx interlayer on device performance, Sol. RRL 3 (2019) 1900261, https://doi.org/10.1002/solr.201900261.
[324] Y. Zheng, B. Jiang, Z. Gao, G. Lin, N. Sang, L. Chen, M. Li, Optimization of SnO2-based electron-selective contacts for Si/PEDOT:PSS heterojunction solar cells, Sol. Energy 193 (2019) 502–506, https://doi.org/10.1016/j.solener.2019.09.077.
[325] S. Bhatia, I.M. Khorakiwala, P.R. Nair, A. Antony, Influence of post deposition fabrication steps and quantitative estimation of band diagram of Si/MoOX heterojunction for carrier selective solar cells, Sol. Energy 194 (2019) 141–147, https://doi.org/10.1016/j.solener.2019.10.025.
[326] J. Cho, H. Sivaramakrishnan Radhakrishnan, R. Sharma, M. Recaman Payo, M. Debucquoy, A. van der Heide, I. Gordon, J. Szlufcik, J. Poortmans, Thermal stability improvement of metal oxide-based contacts for silicon heterojunction solar cells, Sol. Energy Mater. Sol. Cells 206 (2020) 110324, https://doi.org/10.1016/j.solmat.2019.110324.
[327] J. Dréon, Q. Jeangros, J. Cattin, J. Haschke, L. Antognini, C. Ballif, M. Boccard, 23.5%-efficient silicon heterojunction silicon solar cell using molybdenum oxide as hole-selective contact, Nano Energy 70 (2020) 104495, https://doi.org/10.1016/j.nanoen.2020.104495.
[328] K. K. Markose, M. Shaji, S. Bhatia, P.R. Nair, K.J. Saji, A. Antony, M.K. Jayaraj, Novel boron-doped p-type Cu2O thin films as a hole-selective contact in c-Si solar cells, ACS Appl. Mater. Interfaces 12 (2020) 12972–12981, https://doi.org/10.1021/acsami.9b22581.
[329] F. Li, Y. Zhou, Y. Yang, G. Dong, Y. Zhou, F. Liu, D. Yu, Silicon heterojunction solar cells with MoOx hole-selective layer by hot wire oxidation–sublimation deposition, Sol. RRL 4 (2020) 1900514, https://doi.org/10.1002/solr.201900514.
[330] G. Chistiakova, B. Macco, L. Korte, Low-temperature atomic layer deposited magnesium oxide as a passivating electron contact for c-Si-based solar cells, IEEE J. Photovolt. 10 (2020) 398–406, https://doi.org/10.1109/JPHOTOV.2019.2961603.
[331] M. Nayak, S. Mudgal, S. Singh, V.K. Komarala, Investigation of anomalous behaviour in J-V and Suns-Voc characteristics of carrier-selective contact silicon solar cells, Sol. Energy 201 (2020) 307–313, https://doi.org/10.1016/j.solener.2020.03.018.
[332] M.E. Karim, A.T.M. Saiful Islam, Y. Nasuno, A. Kuddus, R. Ishikawa, H. Shirai, Solution-processed TiO2 as a hole blocking layer in PEDOT:PSS/n-Si heterojunction solar cells, EPJ Photo 11 (2020).
[333] H. Lin, J. Wang, Z. Wang, Z. Xu, P. Gao, W. Shen, Edge effect in silicon solar cells with dopant-free interdigitated back-contacts, Nano Energy 74 (2020) 104893, https://doi.org/10.1016/j.nanoen.2020.104893.
[334] J. Li, T. Pan, J. Wang, S. Cao, Y. Lin, B. Hoex, Z. Ma, L. Lu, L. Yang, B. Sun, D. Li, Bilayer MoOX/CrOX passivating contact targeting highly stable silicon heterojunction solar cells, ACS Appl. Mater. Interfaces 12 (2020) 36778–36786, https://doi.org/10.1021/acsami.0c09877.
[335] V.-A. Dao, T.T. Trinh, S. Kim, L. Van Ngoc, T.D. Viet, N.T. Thanh Giang, D. L. Duong, H.T. Thanh Nguyen, N.D. Nam, J. Yi, J. Kim, Carrier transport mechanisms of reactively direct current magnetron sputtered tungsten oxide/n-

type crystalline silicon heterojunction, J. Power Sources 472 (2020) 228460, https://doi.org/10.1016/j.jpowsour.2020.228460.
[336] E. Bobeico, L.V. Mercaldo, P. Morvillo, I. Usatii, M. Della Noce, L. Lancellotti, C. Sasso, R. Ricciardi, P. Delli Veneri, Evaporated MoOx as general back-side hole collector for solar cells, Coatings 10 (2020), https://doi.org/10.3390/coatings10080763.
[337] S. Cao, J. Li, J. Zhang, Y. Lin, L. Lu, J. Wang, M. Yin, L. Yang, X. Chen, D. Li, Stable MoOX-based heterocontacts for p-type crystalline silicon solar cells achieving 20% efficiency, Adv. Funct. Mater. 30 (2020) 2004367, https://doi.org/10.1002/adfm.202004367.
[338] Y.-T. Lee, F.-R. Lin, Z. Pei, Solution-processed titanium oxide for rear contact improvement in heterojunction solar cells, Energies 13 (2020), https://doi.org/10.3390/en13184650.
[339] L. Meng, Z. Yao, L. Cai, W. Wang, L. Zhang, K. Qiu, W. Lin, H. Shen, Z. Liang, Indium sulfide-based electron-selective contact and dopant-free heterojunction silicon solar cells, Sol. Energy 211 (2020) 759–766, https://doi.org/10.1016/j.solener.2020.09.082.
[340] W. Lin, M. Boccard, S. Zhong, V. Paratte, Q. Jeangros, L. Antognini, J. Dréon, J. Cattin, J. Thomet, Z. Liu, Z. Chen, Z. Liang, P. Gao, H. Shen, C. Ballif, Degradation mechanism and stability improvement of dopant-free ZnO/LiFx/Al electron nanocontacts in silicon heterojunction solar cells, ACS Appl. Nano Mater. 3 (2020) 11391–11398, https://doi.org/10.1021/acsanm.0c02475.
[341] J. Ma, Y. Yuan, P. Sun, Approaching 23% silicon heterojunction solar cells with dual-functional SiOx/MoS2 quantum dots interface layers, Sol. Energy Mater. Sol. Cells 227 (2021) 111110, https://doi.org/10.1016/j.solmat.2021.111110.
[342] Y. Jiang, S. Cao, L. Lu, G. Du, Y. Lin, J. Wang, L. Yang, W. Zhu, D. Li, Post-annealing Effect on Optical and Electronic Properties of Thermally Evaporated MoOX Thin Films as Hole-Selective Contacts for p-Si Solar Cells, Nanoscale Res. Lett. 16 (2021) 87, https://doi.org/10.1186/s11671-021-03544-9.
[343] S. Chowdhury, M. Quddammah Khokhar, S. Lee, Y. Kim, J. Park, D.P. Pham, J. Yi, p-type heterojunction bifacial solar cell with rear side carrier selective contact, Inorg. Chem. Commun. 129 (2021) 108658, https://doi.org/10.1016/j.inoche.2021.108658.
[344] V.S. Nguyen, A. Sekkat, D. Bellet, G. Chichignoud, A. Kaminski-Cachopo, D. Muñoz-Rojas, W. Favre, Open-air, low-temperature deposition of phase pure Cu2O thin films as efficient hole-transporting layers for silicon heterojunction solar cells, J. Mater. Chem. A 9 (2021) 15968–15974, https://doi.org/10.1039/D1TA02931B.
[345] Y. Nakagawa, K. Gotoh, T. Inoue, Y. Kurokawa, N. Usami, Improved performance of titanium oxide/silicon oxide electron-selective contacts by implementation of magnesium interlayers, Phys. Status Solidi (a) 218 (2021) 2100296, https://doi.org/10.1002/pssa.202100296.
[346] C. Lu, Rusli, A.B. Prakoso, H. Wang, Hole selective WOx and V2Ox contacts using solution process for silicon solar cells application, Mater. Chem. Phys. 273 (2021) 125101, https://doi.org/10.1016/j.matchemphys.2021.125101.
[347] X. Huang, E. Hara, H. Sugime, S. Noda, Carbon nanotube/silicon heterojunction solar cell with an active area of 4 cm2 realized using a multifunctional molybdenum oxide layer, Carbon 185 (2021) 215–223, https://doi.org/10.1016/j.carbon.2021.08.056.
[348] K. Qiu, Q. Xie, L. Meng, L. Cai, W. Lin, Z. Yao, B. Ai, Z. Liang, H. Shen, A comprehensive study of the light soaking effect in ZnS/p-Si heterojunction solar cells, Sol. Energy 225 (2021) 961–968, https://doi.org/10.1016/j.solener.2021.08.012.
[349] J. Dréon, J. Cattin, G. Christmann, D. Fébba, V. Paratte, L. Antognini, W. Lin, S. Nicolay, C. Ballif, M. Boccard, Performance limitations and analysis of silicon heterojunction solar cells using ultra-thin MoOx hole-selective contacts, IEEE J. Photovolt. 11 (2021) 1158–1166, https://doi.org/10.1109/JPHOTOV.2021.3082400.
[350] L. Li, G. Du, Y. Lin, X. Zhou, Z. Gu, L. Lu, W. Liu, J. Huang, J. Wang, L. Yang, S.-T. Zhang, D. Li, NiOx/MoOx bilayer as an efficient hole-selective contact in crystalline silicon solar cells, Cell Rep. Phys. Sci. 2 (2021) 100684, https://doi.org/10.1016/j.xcrp.2021.100684.
[351] Q. Wang, Y. Zhou, W. Guo, Y. Yang, J. Shang, H. Chen, H. Mao, T. Zhu, Y. Zhou, F. Liu, p-type c-Si/SnO2/Mg heterojunction solar cells with an induced inversion layer, Appl. Phys. Lett. 119 (2021) 263502, https://doi.org/10.1063/5.0070585.
[352] K. Ozel, A. Yildiz, Comprehensive understanding of the role of emitter layer thickness for metal–oxide–semiconductors based solar cells, IEEE J. Photovolt. 12 (2022) 251–258, https://doi.org/10.1109/JPHOTOV.2021.3119612.
[353] M.M. Makhlouf, M.M. Shehata, Multilayer emitter of molybdenum oxide/silver/molybdenum oxide thin films for silicon heterojunction solar cells: device fabrication and electrical characterization, J. Alloy. Compd. 904 (2022) 164102, https://doi.org/10.1016/j.jallcom.2022.164102.
[354] M.R. Samantaray, T. Chichkhede, D.S. Ghosh, N. Chander, Large-area si solar cells based on molybdenum oxide hole selective contacts, Silicon 14 (2022) 10263–10270, https://doi.org/10.1007/s12633-022-01743-2.
[355] X. Yang, S. Zhao, Q. Huang, C. Yu, J. Zhou, X. Liu, X. Su, Y. Zhao, G. Hou, Sub-stochiometric MoOx by radio-frequency magnetron sputtering as hole-selective passivating contacts for silicon heterojunction solar cells, Chin. Phys. B 31 (2022) 098401, https://doi.org/10.1088/1674-1056/ac5a42.
[356] J. He, G. Wang, Y. Qiu, Z. Tang, F. Ye, C. Zhang, S. Wang, L. Cai, T. Yu, P. Gao, Enabling transparent-conductive-oxide free efficient heterojunction solar cells by flexibly using dopant-free contact, Adv. Funct. Mater. 32 (2022) 2205901, https://doi.org/10.1002/adfm.202205901.
[357] M.Q. Khokhar, K. Mallem, X. Fan, Y. Kim, S.Q. Hussain, E.-C. Cho, J. Yi, Experimental and numerical simulation of molybdenum oxide films with wide bandgap and high work function for carrier-selective contact solar cells, ECS J. Solid State Sci. Technol. 11 (2022) 085001, https://doi.org/10.1149/2162-8777/ac8372.
[358] M.-R. Zamani-Meymian, N. Naderi, M. Zareshahi, Improved n-ZnO nanorods/p-Si heterojunction solar cells with graphene incorporation, Ceram. Int. 48 (2022) 34948–34956, https://doi.org/10.1016/j.ceramint.2022.08.084.
[359] L. Cao, P. Procel, A. Alcañiz, J. Yan, F. Tichelaar, E. Özkol, Y. Zhao, C. Han, G. Yang, Z. Yao, M. Zeman, R. Santbergen, L. Mazzarella, O. Isabella, Achieving 23.83% conversion efficiency in silicon heterojunction solar cell with ultra-thin MoOx hole collector layer via tailoring (i)a-Si:H/MoOx interface, Prog. Photovolt.: Res. Appl. 31 (2023) 1245–1254, https://doi.org/10.1002/pip.3638.
[360] M. Wang, G. Wang, W. Gong, S. Cheng, L. Zhao, X. Xu, D. Gong, F. Ye, L. Mo, H. Diao, W. Wang, Influence of In2O3:SnO2 films at different sputtering power on efficiency and stability of heterojunction solar cells, Sol. Energy Mater. Sol. Cells 253 (2023) 112229, https://doi.org/10.1016/j.solmat.2023.112229.
[361] Q. Geng, Z. Wang, Z. Liu, Y. Liu, Z. Gao, Y. Li, X. Sun, L. Chen, X. Lv, M. Li, Construction of V2Ox/Si heterojunction and carrier-assisted collection for high-efficiency silicon solar cells, Mater. Today Energy 34 (2023) 101317, https://doi.org/10.1016/j.mtener.2023.101317.
[362] J. Kumari, Rahul, P. Agarwal, Role of deposition parameters on optoelectronic properties of ITO films and its application in MoO3−x/c-Si(n) heterojunction solar cells, J. Mater. Sci.: Mater. Electron. 34 (2023) 1286, https://doi.org/10.1007/s10854-023-10715-0.
[363] J. Ma, J. Li, W. Zheng, Y. Fu, In situ growth MoS2 quantum dots as promising interface materials for silicon solar cells, Mater. Sci. Semicond. Process. 165 (2023) 107653, https://doi.org/10.1016/j.mssp.2023.107653.
[364] T. Wang, G. Yu, Y. Wei, W. Liu, W. Fu, Y. Lin, X. Wu, L. Xu, P. Lin, X. Yu, P. Wang, C. Cui, Solution-processed vanadium oxide by low-temperature annealing for silicon solar cells with hole selective contact, Mater. Sci. Semicond. Process. 165 (2023) 107638, https://doi.org/10.1016/j.mssp.2023.107638.
[365] Z. Xu, X. Liu, J. Zhou, Y. Yan, Y. Song, Q. Huang, H. Ren, Y. Ding, X. Zhang, Y. Zhao, G. Hou, Aluminum and molybdenum Co-doped zinc oxide films as dual-functional carrier-selective contact for silicon solar cells, ACS Appl. Mater. Interfaces 15 (2023) 34964–34972, https://doi.org/10.1021/acsami.3c05838.
[366] R. Shafique, H. Latif, A. Sattar, S.A. Shabbir, Effect of anti-reflecting layers on device performance of SWCNTs/Si hetero-junction hybrid solar cells, Opt. Mater. 143 (2023) 114215, https://doi.org/10.1016/j.optmat.2023.114215.
[367] W. Liu, W. Fu, Y. Wei, G. Yu, T. Wang, L. Xu, X. Wu, P. Lin, X. Yu, C. Cui, P. Wang, Exceptional hole-selective properties of Ta2O5 films via Sn4+ doping for high performance silicon heterojunction solar cells, Small 20 (2024) 2306666, https://doi.org/10.1002/smll.202306666.
[368] J. Li, Q. Kang, Y. Wang, Z. Zhou, Z. Sun, H. Zhang, W. Lu, X. Tao, S.-T. Zhang, X. Chen, Z. Zheng, H. Yan, D. Li, Y. Zhang, Low oxygen content MoOx and SiOx Tunnel layer based heterocontacts for efficient and stable crystalline silicon solar cells approaching 22% efficiency, Adv. Funct. Mater. 34 (2024) 2310619, https://doi.org/10.1002/adfm.202310619.
[369] M. Jeong, J. Park, Y.J. Cho, H.S. Chang, Enhancing performance of heterojunction silicon solar cells through atomic-layer-deposited MoOx hole contact and atomic-layer-deposited AlZnO layer, Vacuum 222 (2024) 113000, https://doi.org/10.1016/j.vacuum.2024.113000.
[370] C. Xing, W. Gu, Z. Xiang, X. Lou, X. Wang, X. Zhang, Y. Wang, X. Yang, B. Sun, Post-annealing-free BaOxFy/LiF-based stack electron-selective contacts for high efficiency crystalline silicon solar cells featuring ultra-low contact resistivity, Chem. Eng. J. 481 (2024) 148568, https://doi.org/10.1016/j.cej.2024.148568.
[371] M. Feifel, J. Ohlmann, J. Benick, T. Rachow, S. Janz, M. Hermle, F. Dimroth, J. Belz, A. Beyer, K. Volz, D. Lackner, MOVPE Grown Gallium Phosphide–Silicon Heterojunction Solar Cells, IEEE J. Photovolt. 7 (2017) 502–507, https://doi.org/10.1109/JPHOTOV.2016.2642645.
[372] A.N. Fioretti, M. Boccard, A.C. Tamboli, A. Zakutayev, C. Ballif, Nitride layer screening as carrier-selective contacts for silicon heterojunction solar cells, AIP Conf. Proc. 1999 (2018) 040007, https://doi.org/10.1063/1.5049270.
[373] J. He, P. Gao, Z. Ling, L. Ding, Z. Yang, J. Ye, Y. Cui, High-efficiency silicon/organic heterojunction solar cells with improved junction quality and interface passivation, ACS Nano 10 (2016) 11525–11531, https://doi.org/10.1021/acsnano.6b07511.
[374] W. Lin, W. Wu, Q. Xie, Z. Liu, K. Qiu, L. Cai, Z. Yao, L. Meng, B. Ai, Z. Liang, H. Shen, Conductive cuprous iodide hole-selective contacts with thermal and ambient stability for silicon solar cells, ACS Appl. Mater. Interfaces 10 (2018) 43699–43706, https://doi.org/10.1021/acsami.8b16883.
[375] Z. Sun, C. Yi, Z. Hameiri, S.P. Bremner, Investigation of the selectivity-mechanism of copper (I) sulfide (Cu2S) as a dopant-free carrier selective contact for silicon solar cells, Appl. Surf. Sci. 555 (2021) 149727, https://doi.org/10.1016/j.apsusc.2021.149727.
[376] Y. Wan, C. Samundsett, J. Bullock, T. Allen, M. Hettick, D. Yan, P. Zheng, X. Zhang, J. Cui, J. McKeon, A. Javey, A. Cuevas, Magnesium fluoride electron-selective contacts for crystalline silicon solar cells, ACS Appl. Mater. Interfaces 8 (2016) 14671–14677, https://doi.org/10.1021/acsami.6b03599.
[377] W. Wang, J. He, L. Cai, Z. Wang, S.K. Karuturi, P. Gao, W. Shen, Solution-processed electron-selective contacts enabling 21.8% efficiency crystalline silicon solar cells, Sol. RRL 4 (2020) 2000569, https://doi.org/10.1002/solr.202000569.
[378] X. Yang, W. Liu, M. De Bastiani, T. Allen, J. Kang, H. Xu, E. Aydin, L. Xu, Q. Bi, H. Dang, E. AlHabshi, K. Kotsovos, A. AlSaggaf, I. Gereige, Y. Wan, J. Peng, C. Samundsett, A. Cuevas, S. De Wolf, Dual-function electron-conductive, hole-blocking titanium nitride contacts for efficient silicon solar cells, Joule 3 (2019) 1314–1327, https://doi.org/10.1016/j.joule.2019.03.008.
[379] Y. Zhang, W. Cui, Y. Zhu, F. Zu, L. Liao, S.-T. Lee, B. Sun, High efficiency hybrid PEDOT:PSS/nanostructured silicon Schottky junction solar cells by doping-free

rear contact, Energy Environ. Sci. 8 (2015) 297–302, https://doi.org/10.1039/C4EE02282C.
[380] N. Itoh, K. Tanimura, Formation of interstitial-vacancy pairs by electronic excitation in pure ionic crystals, J. Phys. Chem. Solids 51 (1990) 717–735, https://doi.org/10.1016/0022-3697(90)90145-6.
[381] B.F. Bory, H.L. Gomes, R.A.J. Janssen, D.M. de Leeuw, S.C.J. Meskers, Electrical conduction of LiF interlayers in organic diodes, J. Appl. Phys. 117 (2015) 155502, https://doi.org/10.1063/1.4917461.
[382] B.F. Bory, P.R.F. Rocha, R.A.J. Janssen, H.L. Gomes, D.M. De Leeuw, S.C. J. Meskers, Lithium fluoride injection layers can form quasi-Ohmic contacts for both holes and electrons, Appl. Phys. Lett. 105 (2014) 123302, https://doi.org/10.1063/1.4896636.
[383] L. Fang, S.J. Baik, S. Lim, S. Yoo, K.S. Lim, Amorphous Si rear Schottky junction solar cell with a LiF/Al back electrode, IEEE Trans. Electron Devices 58 (2011) 3048–3052, https://doi.org/10.1109/TED.2011.2160267.
[384] J.-H. Yang, H.-H. Jung, J. Seo, K.-D. Kim, D.-H. Kim, D.-C. Lim, S.-G. Park, J.-W. Kang, M. Song, M.-S. Choi, J.-D. Kwon, K.-S. Nam, Y. Jeong, S.-H. Kwon, Y. C. Park, Y.-C. Kang, K.B. Chung, C.S. Kim, K.S. Lim, S.Y. Ryu, Dopant-free hydrogenated amorphous silicon thin-film solar cells using molybdenum oxide and lithium fluoride, J. Phys. Chem. C. 117 (2013) 23459–23468, https://doi.org/10.1021/jp4031656.
[385] J. Bullock, P. Zheng, Q. Jeangros, M. Tosun, M. Hettick, C.M. Sutter-Fella, Y. Wan, T. Allen, D. Yan, D. Macdonald, S. De Wolf, A. Hessler-Wyser, A. Cuevas, A. Javey, Lithium fluoride based electron contacts for high efficiency n-type crystalline silicon solar cells, Adv. Energy Mater. 6 (2016) 1600241, https://doi.org/10.1002/aenm.201600241.
[386] W. Wu, W. Lin, S. Zhong, B. Paviet-Salomon, M. Despeisse, Q. Jeangros, Z. Liang, M. Boccard, H. Shen, C. Ballif, Dopant-free back-contacted silicon solar cells with an efficiency of 22.1, Phys. Status Solidi (RRL) – Rapid Res. Lett. 14 (2020) 1900688, https://doi.org/10.1002/pssr.201900688.
[387] E. Nurlaela, A. Ziani, K. Takanabe, Tantalum nitride for photocatalytic water splitting: concept and applications, Mater. Renew. Sustain. Energy 5 (2016) 18, https://doi.org/10.1007/s40243-016-0083-z.
[388] J.-S. Park, H.-S. Park, S.-W. Kang, Plasma-enhanced atomic layer deposition of Ta-N thin films, J. Electrochem. Soc. 149 (2001) C28.
[389] X. Yang, E. Aydin, H. Xu, J. Kang, M. Hedhili, W. Liu, Y. Wan, J. Peng, C. Samundsett, A. Cuevas, S. De Wolf, Tantalum nitride electron-selective contact for crystalline silicon solar cells, Adv. Energy Mater. 8 (2018) 1800608, https://doi.org/10.1002/aenm.201800608.
[390] Y.-S. Kou, S.-T. Yang, S. Thiyagu, C.-T. Liu, J.-W. Wu, C.-F. Lin, Solution-processed carrier selective layers for high efficiency organic/nanostructured-silicon hybrid solar cells, Nanoscale 8 (2016) 5379–5385, https://doi.org/10.1039/C5NR08724D.
[391] Y. Wan, J. Bullock, M. Hettick, Z. Xu, C. Samundsett, D. Yan, J. Peng, J. Ye, A. Javey, A. Cuevas, Temperature and humidity stable alkali/alkaline-earth metal carbonates as electron heterocontacts for silicon photovoltaics, Adv. Energy Mater. 8 (2018) 1800743, https://doi.org/10.1002/aenm.201800743.
[392] W. Wu, J. Bao, Z. Liu, W. Lin, X. Yu, L. Cai, B. Liu, J. Song, H. Shen, Multilayer MoOx/Ag/MoOx emitters in dopant-free silicon solar cells, Mater. Lett. 189 (2017) 86–88, https://doi.org/10.1016/j.matlet.2016.11.059.
[393] C. Coluzza, M. Garozzo, G. Maletta, D. Margadonna, R. Tomaciello, P. Migliorato, n-CdS/p-Si heterojunction solar cells, Appl. Phys. Lett. 37 (1980) 569–572, https://doi.org/10.1063/1.91787.
[394] Y.J. Hsiao, T.H. Meen, L.W. Ji, J.K. Tsai, Y.S. Wu, C.J. Huang, Preparation of ZnS microdisks using chemical bath deposition and ZnS/p-Si heterojunction solar cells, J. Phys. Chem. Solids 74 (2013) 1403–1407, https://doi.org/10.1016/j.jpcs.2013.04.023.
[395] S. Limpert, K. Ghosh, H. Wagner, S. Bowden, C. Honsberg, S. Goodnick, S. Bremner, A. Ho-Baillie, M. Green, Results from coupled optical and electrical sentaurus TCAD models of a gallium phosphide on silicon electron carrier selective contact solar cell, IEEE 40th Photovolt. Spec. Conf. (PVSC) 2014 (2014) 0836–0840.
[396] A.N. Fioretti, M. Boccard, A.C. Tamboli, A. Zakutayev, C. Ballif, Nitride layer screening as carrier-selective contacts for silicon heterojunction solar cells, AIP Conf. Proc., AIP Publ. (2018).
[397] W. Sun, C.J. Bartel, E. Arca, S.R. Bauers, B. Matthews, B. Orvañanos, B.-R. Chen, M.F. Toney, L.T. Schelhas, W. Tumas, J. Tate, A. Zakutayev, S. Lany, A.M. Holder, G. Ceder, A map of the inorganic ternary metal nitrides, Nat. Mater. 18 (2019) 732–739, https://doi.org/10.1038/s41563-019-0396-2.
[398] L.W. Ji, Y.J. Hsiao, I.T. Tang, T.H. Meen, C.H. Liu, J.K. Tsai, T.C. Wu, Y.S. Wu, Annealing effect and photovoltaic properties of nano-ZnS/textured p-Si heterojunction, Nanoscale Res Lett. 8 (2013) 470, https://doi.org/10.1186/1556-276x-8-470.
[399] K.F. Abd El-Rahman, A.A.A. Darwish, E.A.A. El-Shazly, Electrical and photovoltaic properties of SnSe/Si heterojunction, Mater. Sci. Semicond. Process. 25 (2014) 123–129, https://doi.org/10.1016/j.mssp.2013.10.003.
[400] M.-L. Tsai, S.-H. Su, J.-K. Chang, D.-S. Tsai, C.-H. Chen, C.-I. Wu, L.-J. Li, L.-J. Chen, J.-H. He, Monolayer MoS2 heterojunction solar cells, ACS Nano 8 (2014) 8317–8322, https://doi.org/10.1021/nn502776h.
[401] J. Liu, F. Yi, B. Wang, T. Zhang, Y. Wang, Y. Zhou, Fabrication and photovoltaic effect of CdS/silicon nanopillars heterojunction solar cell, ChemistrySelect 1 (2016) 4901–4905, https://doi.org/10.1002/slct.201601025.
[402] S. Yachi, R. Takabe, K. Toko, T. Suemasu, Effect of p-BaSi2 layer thickness on the solar cell performance of p-BaSi2/n-Si heterojunction solar cells, Jpn. J. Appl. Phys. 56 (2017) 05DB03, https://doi.org/10.7567/JJAP.56.05DB03.
[403] K. Qiu, D. Qiu, L. Cai, S. Li, W. Wu, Z. Liang, H. Shen, Preparation of ZnS thin films and ZnS/p-Si heterojunction solar cells, Mater. Lett. 198 (2017) 23–26, https://doi.org/10.1016/j.matlet.2017.03.171.
[404] Y. Yamashita, S. Yachi, R. Takabe, T. Sato, M.E. Bayu, K. Toko, T. Suemasu, Reduction in interface defect density in p-BaSi2/n-Si heterojunction solar cells by a modified pretreatment of the Si substrate, Jpn. J. Appl. Phys. 57 (2018) 025501, https://doi.org/10.7567/JJAP.57.025501.
[405] R. Saive, H. Emmer, C.T. Chen, C. Zhang, C. Honsberg, H. Atwater, Study of the interface in a GaP/Si heterojunction solar cell, IEEE J. Photovolt. 8 (2018) 1568–1576, https://doi.org/10.1109/JPHOTOV.2018.2861724.
[406] A.T.M.S. Islam, M.E. Karim, A. Rajib, Y. Nasuno, T. Ukai, S. Kurosu, M. Tokuda, Y. Fujii, Y. Nakajima, T. Hanajiri, H. Shirai, Chemical mist deposition of organic for efficient front- and back-PEDOT:PSS/crystalline Si heterojunction solar cells, Appl. Phys. Lett. 114 (2019) 193901, https://doi.org/10.1063/1.5096579.
[407] Y. Zhang, Y. Zhuang, L. Liu, P. Qiu, L. Su, X. Teng, G. Fu, W. Yu, The microstructure evolution during MoS2 films growth and its influence on the MoS2 optical-electrical properties in MoS2/p-Si heterojunction solar cells, Superlattices Microstruct. 137 (2020) 106352, https://doi.org/10.1016/j.spmi.2019.106352.
[408] J. Yu, P. Phang, C. Samundsett, R. Basnet, G.P. Neupan, X. Yang, D.H. Macdonald, Y. Wan, D. Yan, J. Ye, Titanium nitride electron-conductive contact for silicon solar cells by radio frequency sputtering from a TiN target, ACS Appl. Mater. Interfaces 12 (2020) 26177–26183, https://doi.org/10.1021/acsami.0c04439.
[409] Y. Zhang, P. Su, L. Liu, P. Qiu, L. Su, G. Fu, W. Yu, The effect of MoS2 modulated doping with molybdenum-oxide on the photovoltaic performance for MoS2/n-Si heterojunction solar cells, Sol. Energy 208 (2020) 1048–1057, https://doi.org/10.1016/j.solener.2020.08.062.
[410] Z. Wang, J. He, W. Wang, H. Lin, Z. Xu, Q. Liu, S. Peng, J. Hou, D. He, P. Gao, Twenty percent efficiency crystalline silicon solar cells with solution-processed electron-selective contacts, ACS Appl. Energy Mater. 4 (2021) 3644–3650, https://doi.org/10.1021/acsaem.1c00041.
[411] M.Q. Khokhar, S.Q. Hussain, D.P. Pham, M. Alzaid, A. Razaq, I. Sultana, Y. Kim, Y.H. Cho, E.-C. Cho, J. Yi, Role of electron carrier selective contact layer of lithium fluoride films with wide bandgap and low work function for silicon heterojunction solar cells, Mater. Sci. Semicond. Process. 134 (2021) 105982, https://doi.org/10.1016/j.mssp.2021.105982.
[412] D. Muchahary, L.S. Ram, R. Narzary, P.P. Sahu, S. Bhattarai, S. Tayal, Heterojunction between crystalline silicon and nanocomposite coupled ZnO·SnO2 and optimization of its photovoltaic performance, Curr. Appl. Phys. 38 (2022) 15–21, https://doi.org/10.1016/j.cap.2022.02.009.
[413] Z. Liu, H. Lin, Z. Wang, L. Chen, T. Wu, Y. Pang, L. Cai, J. He, S. Peng, H. Shen, P. Gao, Dual functional dopant-free contacts with titanium protecting layer: boosting stability while balancing electron transport and recombination losses, Adv. Sci. 9 (2022) 2202240, https://doi.org/10.1002/advs.202202240.
[414] Z. Liu, H. Lin, T. Wu, Z. Wang, Y. Pang, G. Wang, Z. Cui, Q. Su, T. Yu, P. Gao, S. Peng, Tailoring protective metals for high-efficient and stable dopant-free crystalline silicon solar cells, Sol. Energy Mater. Sol. Cells 256 (2023) 112343, https://doi.org/10.1016/j.solmat.2023.112343.
[415] I. Lee, R. Sahu, K. Kim, Silicon solar cell with tunneling oxide on sulfur-deficient intrinsic MoS2 thin film, Phys. Status Solidi (a) 220 (2023) 2300601, https://doi.org/10.1002/pssa.202300601.
[416] W. Fu, W. Liu, Y. Wei, D. Liu, S. Li, D. Zhao, X. Wu, L. Xu, P. Lin, C. Cui, X. Yu, P. Wang, Solution-processed copper(i) iodide via co-doping for enhanced hole selective contacts in p-type crystalline silicon solar cells, J. Mater. Chem. C. 12 (2024) 1386–1395, https://doi.org/10.1039/D3TC02988C.
[417] J. He, Y. Wan, P. Gao, J. Tang, J. Ye, Over 16.7% efficiency organic-silicon heterojunction solar cells with solution-processed dopant-free contacts for both polarities, Adv. Funct. Mater. 28 (2018) 1802192, https://doi.org/10.1002/adfm.201802192.
[418] W. Ji, T. Allen, X. Yang, G. Zeng, S. De Wolf, A. Javey, Polymeric electron-selective contact for crystalline silicon solar cells with an efficiency exceeding 19, ACS Energy Lett. 5 (2020) 897–902, https://doi.org/10.1021/acsenergylett.0c00110.
[419] C. Reichel, U. Würfel, K. Winkler, H.-F. Schleiermacher, M. Kohlstädt, M. Unmüssig, C.A. Messmer, M. Hermle, S.W. Glunz, Electron-selective contacts via ultra-thin organic interface dipoles for silicon organic heterojunction solar cells, J. Appl. Phys. 123 (2018) 024505, https://doi.org/10.1063/1.5010937.
[420] D. Wang, J. Sheng, S. Wu, J. Zhu, S. Chen, P. Gao, J. Ye, Tuning back contact property via artificial interface dipoles in Si/organic hybrid solar cells, Appl. Phys. Lett. 109 (2016) 043901, https://doi.org/10.1063/1.4959839.
[421] X. Yang, Z. Ying, Z. Yang, J.-R. Xu, W. Wang, J. Wang, Z. Wang, L. Yao, B. Yan, J. Ye, Light-promoted electrostatic adsorption of high-density lewis base monolayers as passivating electron-selective contacts, Adv. Sci. 8 (2021) 2003245, https://doi.org/10.1002/advs.202003245.
[422] Y. Zhang, F. Zu, S.-T. Lee, L. Liao, N. Zhao, B. Sun, Heterojunction with organic thin layers on silicon for record efficiency hybrid solar cells, Adv. Energy Mater. 4 (2014) 1300923, https://doi.org/10.1002/aenm.201300923.
[423] J. Liu, Y. Ji, Y. Liu, Z. Xia, Y. Han, Y. Li, B. Sun, Doping-free asymmetrical silicon heterocontact achieved by integrating conjugated molecules for high efficient solar cell, Adv. Energy Mater. 7 (2017) 1700311, https://doi.org/10.1002/aenm.201700311.
[424] Y. Han, Y. Liu, J. Yuan, H. Dong, Y. Li, W. Ma, S.-T. Lee, B. Sun, Naphthalene diimide-based n-type polymers: efficient rear interlayers for high-performance silicon–organic heterojunction solar cells, ACS Nano 11 (2017) 7215–7222, https://doi.org/10.1021/acsnano.7b03090.
[425] J. He, W. Zhang, J. Ye, P. Gao, 16% efficient silicon/organic heterojunction solar cells using narrow band-gap conjugated polyelectrolytes based low resistance

electron-selective contacts, Nano Energy 43 (2018) 117–123, https://doi.org/10.1016/j.nanoen.2017.11.025.
[426] W. Li, E. Martínez-Ferrero, E. Palomares, Self-assembled molecules as selective contacts for efficient and stable perovskite solar cells, Mater. Chem. Front. 8 (2024) 681–699, https://doi.org/10.1039/D3QM01017A.
[427] A. Al-Ashouri, A. Magomedov, M. Roß, M. Jošt, M. Talaikis, G. Chistiakova, T. Bertram, J.A. Márquez, E. Köhnen, E. Kasparavičius, S. Levcenco, L. Gil-Escrig, C.J. Hages, R. Schlatmann, B. Rech, T. Malinauskas, T. Unold, C.A. Kaufmann, L. Korte, G. Niaura, V. Getautis, S. Albrecht, Conformal monolayer contacts with lossless interfaces for perovskite single junction and monolithic tandem solar cells, Energy Environ. Sci. 12 (2019) 3356–3369, https://doi.org/10.1039/C9EE02268F.
[428] A. Magomedov, A. Al-Ashouri, E. Kasparavičius, S. Strazdaite, G. Niaura, M. Jošt, T. Malinauskas, S. Albrecht, V. Getautis, Self-assembled hole transporting monolayer for highly efficient perovskite solar cells, Adv. Energy Mater. 8 (2018) 1801892, https://doi.org/10.1002/aenm.201801892.
[429] F. Ali, C. Roldán-Carmona, M. Sohail, M.K. Nazeeruddin, Applications of self-assembled monolayers for perovskite solar cells interface engineering to address efficiency and stability, Adv. Energy Mater. 10 (2020) 2002989, https://doi.org/10.1002/aenm.202002989.
[430] S.Y. Kim, S.J. Cho, S.E. Byeon, X. He, H.J. Yoon, Self-assembled monolayers as interface engineering nanomaterials in perovskite solar cells, Adv. Energy Mater. 10 (2020) 2002606, https://doi.org/10.1002/aenm.202002606.
[431] A. Prasetio, R.R. Pradhan, P. Dally, M. Ghadiyali, R. Azmi, U. Schwingenschlögl, T.G. Allen, S. De Wolf, Efficient silicon solar cells through organic self-assembled monolayers as electron selective contacts, Adv. Energy Mater. 14 (2024) 2303705, https://doi.org/10.1002/aenm.202303705.
[432] J. Ouyang, Secondary doping" methods to significantly enhance the conductivity of PEDOT:PSS for its application as transparent electrode of optoelectronic devices, Displays 34 (2013) 423–436, https://doi.org/10.1016/j.displa.2013.08.007.
[433] Q. Liu, R. Ishikawa, S. Funada, T. Ohki, K. Ueno, H. Shirai, Highly Efficient Solution-Processed Poly(3,4-ethylenedio-xythiophene):Poly(styrenesulfonate)/Crystalline–Silicon Heterojunction Solar Cells with Improved Light-Induced Stability, Adv. Energy Mater. 5 (2015) 1500744, https://doi.org/10.1002/aenm.201500744.
[434] J.P. Thomas, K.T. Leung, Mixed co-solvent engineering of PEDOT:PSS to enhance its conductivity and hybrid solar cell properties, J. Mater. Chem. A 4 (2016) 17537–17542, https://doi.org/10.1039/C6TA07410C.
[435] J.P. Thomas, S. Srivastava, L. Zhao, M. Abd-Ellah, D. McGillivray, J.S. Kang, M. A. Rahman, N. Moghimi, N.F. Heinig, K.T. Leung, Reversible structural transformation and enhanced performance of PEDOT:PSS-based hybrid solar cells driven by light intensity, ACS Appl. Mater. Interfaces 7 (2015) 7466–7470, https://doi.org/10.1021/acsami.5b01252.
[436] Q. Xu, T. Song, W. Cui, Y. Liu, W. Xu, S.-T. Lee, B. Sun, Solution-processed highly conductive PEDOT:PSS/AgNW/GO transparent film for efficient organic-Si hybrid solar cells, ACS Appl. Mater. Interfaces 7 (2015) 3272–3279, https://doi.org/10.1021/am508006q.
[437] J.P. Thomas, M.A. Rahman, S. Srivastava, J.-S. Kang, D. McGillivray, M. Abd-Ellah, N.F. Heinig, K.T. Leung, Highly Conducting Hybrid Silver-Nanowire-Embedded Poly(3,4-ethylenedioxythiophene):Poly(styrenesulfonate) for High-Efficiency Planar Silicon/Organic Heterojunction Solar Cells, ACS Nano 12 (2018) 9495–9503, https://doi.org/10.1021/acsnano.8b04848.
[438] Y. Li, M. Liu, Y. Li, K. Yuan, L. Xu, W. Yu, R. Chen, X. Qiu, H.-L. Yip, Poly(3,4-Ethylenedioxythiophene): methylnaphthalene sulfonate formaldehyde condensate: the effect of work function and structural homogeneity on hole injection/extraction properties, Adv. Energy Mater. 7 (2017) 1601499, https://doi.org/10.1002/aenm.201601499.
[439] Y. Wang, Z. Xia, L. Liu, W. Xu, Z. Yuan, Y. Zhang, H. Sirringhaus, Y. Lifshitz, S.-T. Lee, Q. Bao, B. Sun, The light-induced field-effect solar cell concept – perovskite nanoparticle coating introduces polarization enhancing silicon cell efficiency, Adv. Mater. 29 (2017) 1606370, https://doi.org/10.1002/adma.201606370.
[440] Y. Zhu, T. Song, F. Zhang, S.-T. Lee, B. Sun, Efficient organic-inorganic hybrid Schottky solar cell: the role of built-in potential, Appl. Phys. Lett. 102 (2013) 113504, https://doi.org/10.1063/1.4796112.
[441] Y. Zhu, T. Song, F. Zhang, S.-T. Lee, B. Sun, Efficient organic-inorganic hybrid Schottky solar cell: The role of built-in potential, Appl. Phys. Lett. 102 (2013).
[442] S. Avasthi, S. Lee, Y.-L. Loo, J.C. Sturm, Role of majority and minority carrier barriers silicon/organic hybrid heterojunction solar cells, Adv. Mater. 23 (2011) 5762–5766, https://doi.org/10.1002/adma.201102712.
[443] P. Yu, C.-Y. Tsai, J.-K. Chang, C.-C. Lai, P.-H. Chen, Y.-C. Lai, P.-T. Tsai, M.-C. Li, H.-T. Pan, Y.-Y. Huang, C.-I. Wu, Y.-L. Chueh, S.-W. Chen, C.-H. Du, S.-F. Horng, H.-F. Meng, 13% efficiency hybrid organic/silicon-nanowire heterojunction solar cell via interface engineering, ACS Nano 7 (2013) 10780–10787, https://doi.org/10.1021/nn403982b.
[444] Y. Liu, Z.-g Zhang, Z. Xia, J. Zhang, Y. Liu, F. Liang, Y. Li, T. Song, X. Yu, S.-t Lee, B. Sun, High performance nanostructured silicon–organic quasi p–n junction solar cells via low-temperature deposited hole and electron selective layer, ACS Nano 10 (2016) 704–712, https://doi.org/10.1021/acsnano.5b05732.
[445] D. Zielke, C. Niehaves, W. Lövenich, A. Elschner, M. Hörteis, J. Schmidt, Organic-silicon solar cells exceeding 20% efficiency, Energy Procedia 77 (2015) 331–339, https://doi.org/10.1016/j.egypro.2015.07.047.
[446] X. Crispin, F.L.E. Jakobsson, A. Crispin, P.C.M. Grim, P. Andersson, A. Volodin, C. van Haesendonck, M. Van der Auweraer, W.R. Salaneck, M. Berggren, The origin of the high conductivity of poly(3,4-ethylenedioxythiophene)−Poly (styrenesulfonate) (PEDOT−PSS) plastic electrodes, Chem. Mater. 18 (2006) 4354–4360, https://doi.org/10.1021/cm061032+.
[447] H.M. Zeyada, M.M. El-Nahass, E.M. El-Menyawy, Fabrication and transport mechanisms of 2-(2,3-dihydro-1,5-dimethyl-3-oxo-2-phenyl-1H-pyrazol-4-ylimino)-2-(4-nitrophenyl)acetonitrile/p-silicon hybrid solar cell, Sol. Energy Mater. Sol. Cells 92 (2008) 1586–1592, https://doi.org/10.1016/j.solmat.2008.07.006.
[448] T. Ino, M. Ono, N. Miyauchi, Q. Liu, Z. Tang, R. Ishikawa, K. Ueno, H. Shirai, Electrospray Deposition of Poly(3-hexylthiophene) Films for Crystalline Silicon/Organic Hybrid Junction Solar Cells, Jpn. J. Appl. Phys. 51 (2012) 061602, https://doi.org/10.1143/JJAP.51.061602.
[449] Q. Liu, M. Ono, Z. Tang, R. Ishikawa, K. Ueno, H. Shirai, Highly efficient crystalline silicon/Zonyl fluorosurfactant-treated organic heterojunction solar cells, Appl. Phys. Lett. 100 (2012) 183901, https://doi.org/10.1063/1.4709615.
[450] I. Khatri, T. Imamura, A. Uehara, R. Ishikawa, K. Ueno, H. Shirai, Chemical mist deposition of graphene oxide and PEDOT:PSS films for crystalline Si/organic heterojunction solar cells, Phys. Status Solidi C. 9 (2012) 2134–2137, https://doi.org/10.1002/pssc.201200132.
[451] Q. Liu, F. Wanatabe, A. Hoshino, R. Ishikawa, T. Gotou, K. Ueno, H. Shirai, Crystalline Silicon/Graphene Oxide Hybrid Junction Solar Cells, Jpn. J. Appl. Phys. 51 (2012) 10NE22, https://doi.org/10.1143/JJAP.51.10NE22.
[452] Q. Liu, T. Imamura, T. Hiate, I. Khatri, Z. Tang, R. Ishikawa, K. Ueno, H. Shirai, Optical anisotropy in solvent-modified poly(3,4-ethylenedioxythiophene):poly (styrenesulfonic acid) and its effect on the photovoltaic performance of crystalline silicon/organic heterojunction solar cells, Appl. Phys. Lett. 102 (2013) 243902, https://doi.org/10.1063/1.4811355.
[453] P. Yu, C.Y. Tsai, J.K. Chang, C.C. Lai, P.H. Chen, Y.C. Lai, P.T. Tsai, M.C. Li, H. T. Pan, Y.Y. Huang, C.I. Wu, Y.L. Chueh, S.W. Chen, C.H. Du, S.F. Horng, H. F. Meng, 13% efficiency hybrid organic/silicon-nanowire heterojunction solar cell via interface engineering, ACS Nano 7 (2013) 10780–10787, https://doi.org/10.1021/nn403982b.
[454] D. Zielke, A. Pazidis, F. Werner, J. Schmidt, Organic-silicon heterojunction solar cells on n-type silicon wafers: The BackPEDOT concept, Sol. Energy Mater. Sol. Cells 131 (2014) 110–116, https://doi.org/10.1016/j.solmat.2014.05.022.
[455] J. Sheng, K. Fan, D. Wang, C. Han, J. Fang, P. Gao, J. Ye, Improvement of the SiOx Passivation Layer for High-Efficiency Si/PEDOT:PSS heterojunction solar cells, ACS Appl. Mater. Interfaces 6 (2014) 16027–16034, https://doi.org/10.1021/am503949g.
[456] Q. Xu, T. Song, W. Cui, Y. Liu, W. Xu, S.T. Lee, B. Sun, Solution-processed highly conductive PEDOT:PSS/AgNW/GO transparent film for efficient organic-Si hybrid solar cells, ACS Appl. Mater. Interfaces 7 (2015) 3272–3279, https://doi.org/10.1021/am508006q.
[457] J. He, P. Gao, M. Liao, X. Yang, Z. Ying, S. Zhou, J. Ye, Y. Cui, Realization of 13.6% Efficiency on 20 μm Thick Si/Organic Hybrid Heterojunction Solar Cells via Advanced Nanotexturing and Surface Recombination Suppression, ACS Nano 9 (2015) 6522–6531, https://doi.org/10.1021/acsnano.5b02432.
[458] J. Sheng, D. Wang, S. Wu, X. Yang, L. Ding, J. Zhu, J. Fang, P. Gao, J. Ye, Ideal rear contact formed via employing a conjugated polymer for Si/PEDOT:PSS hybrid solar cells, RSC Adv. 6 (2016) 16010–16017, https://doi.org/10.1039/C5RA26152J.
[459] M.H. Yun, J.W. Kim, S.Y. Park, D.S. Kim, B. Walker, J.Y. Kim, High-efficiency, hybrid Si/C60 heterojunction solar cells, J. Mater. Chem. A 4 (2016) 16410–16417, https://doi.org/10.1039/C6TA02248K.
[460] X. Dai, T. Chen, H. Cai, H. Wen, Y. Sun, Improving performance of organic-silicon heterojunction solar cells based on textured surface via acid processing, ACS Appl. Mater. Interfaces 8 (2016) 14572–14577, https://doi.org/10.1021/acsami.6b03164.
[461] T. Ohki, K. Ichikawa, J. Hossain, Y. Fujii, T. Hanajiri, R. Ishikawa, K. Ueno, H. Shirai, Effect of substrate bias on mist deposition of conjugated polymer on textured crystalline-Si for efficient c-Si/organic heterojunction solar cells, Phys. Status Solidi (a) 213 (2016) 1922–1925, https://doi.org/10.1002/pssa.201532951.
[462] P.-T. Tsai, M.-C. Li, Y.-C. Lai, W.-H. Tseng, C.-I. Wu, S.-H. Chen, Y.-C. Lin, Y.-C. Chen, R.-C. Hsiao, S.-F. Horng, P. Yu, H.-F. Meng, Solution p-doped fluorescent polymers for enhanced charge transport of hybrid organic-silicon nanowire photovoltaics, Org. Electron. 34 (2016) 246–253, https://doi.org/10.1016/j.orgel.2016.04.005.
[463] S. Wu, W. Cui, N. Aghdassi, T. Song, S. Duhm, S.-T. Lee, B. Sun, Nanostructured Si/organic heterojunction solar cells with high open-circuit voltage via improving junction quality, Adv. Funct. Mater. 26 (2016) 5035–5041, https://doi.org/10.1002/adfm.201600441.
[464] J. Hossain, Q. Liu, T. Miura, K. Kasahara, D. Harada, R. Ishikawa, K. Ueno, H. Shirai, Nafion-modified PEDOT:PSS as a transparent hole-transporting layer for high-performance crystalline-si/organic heterojunction solar cells with improved light soaking stability, ACS Appl. Mater. Interfaces 8 (2016) 31926–31934, https://doi.org/10.1021/acsami.6b10272.
[465] Y. Jiang, X. Gong, R. Qin, H. Liu, C. Xia, H. Ma, Efficiency enhancement mechanism for poly(3, 4-ethylenedioxythiophene):poly(styrenesulfonate)/silicon nanowires hybrid solar cells using alkali treatment, Nanoscale Res. Lett. 11 (2016) 267, https://doi.org/10.1186/s11671-016-1450-5.
[466] X. Shen, L. Chen, J. Pan, Y. Hu, S. Li, J. Zhao, Improved work function of poly(3,4-ethylenedioxythiophene): poly(styrenesulfonic acid) and its effect on hybrid silicon/organic heterojunction solar cells, Nanoscale Res. Lett. 11 (2016) 532, https://doi.org/10.1186/s11671-016-1759-0.

[467] C.-C. Chueh, M. Crump, A.K.Y. Jen, Optical enhancement via electrode designs for high-performance polymer solar cells, Adv. Funct. Mater. 26 (2016) 321–340, https://doi.org/10.1002/adfm.201503489.
[468] Y.-T. Lee, F.-R. Lin, C.-H. Chen, Z. Pei, A 14.7% organic/silicon nanoholes hybrid solar cell via interfacial engineering by solution-processed inorganic conformal layer, ACS Appl. Mater. Interfaces 8 (2016) 34537–34545, https://doi.org/10.1021/acsami.6b10741.
[469] S. Mahato, L.G. Gerling, C. Voz, R. Alcubilla, J. Puigdollers, High efficiency ITO-free hybrid solar cell using highly conductive PEDOT:PSS with co-solvent and surfactant treatments, Mater. Lett. 186 (2017) 165–167, https://doi.org/10.1016/j.matlet.2016.10.014.
[470] S. Diao, X. Zhang, Z. Shao, K. Ding, J. Jie, X. Zhang, 12.35% efficient graphene quantum dots/silicon heterojunction solar cells using graphene transparent electrode, Nano Energy 31 (2017) 359–366, https://doi.org/10.1016/j.nanoen.2016.11.051.
[471] H. Wen, H. Cai, Y. Du, X. Dai, Y. Sun, J. Ni, J. Li, D. Zhang, J. Zhang, Improving the organic/Si heterojunction hybrid solar cell property by optimizing PEDOT:PSS film and with amorphous silicon as back surface field, Appl. Phys. A 123 (2016) 14, https://doi.org/10.1007/s00339-016-0612-8.
[472] Z. Yang, P. Gao, J. He, W. Chen, W.-Y. Yin, Y. Zeng, W. Guo, J. Ye, Y. Cui, Tuning of the contact properties for high-efficiency Si/PEDOT:PSS heterojunction solar cells, ACS Energy Lett. 2 (2017) 556–562, https://doi.org/10.1021/acsenergylett.7b00015.
[473] J. He, P. Gao, Z. Yang, J. Yu, W. Yu, Y. Zhang, J. Sheng, J. Ye, J.C. Amine, Y. Cui, Silicon/organic hybrid solar cells with 16.2% efficiency and improved stability by formation of conformal heterojunction coating and moisture-resistant capping layer, Adv. Mater. 29 (2017) 1606321, https://doi.org/10.1002/adma.201606321.
[474] Y.-H. Nam, D.-H. Kim, S.S. Shinde, J.-W. Song, M.-J. Park, J.-Y. Yu, J.-H. Lee, Planar n-Si/PEDOT:PSS hybrid heterojunction solar cells utilizing functionalized carbon nanoparticles synthesized via simple pyrolysis route, Nanotechnology 28 (2017) 475402, https://doi.org/10.1088/1361-6528/aa9014.
[475] S.B. Kang, M.H. Jeong, I.Y. Choi, S.-D. Sohn, S.H. Kim, H.-J. Shin, W.I. Park, J. C. Shin, M.H. Song, K.J. Choi, Self-assembled, highly crystalline porous ferroelectric poly(vinylidene fluoride-co-trifluoroethylene) interlayer for Si/organic hybrid solar cells, Nano Energy 41 (2017) 243–250, https://doi.org/10.1016/j.nanoen.2017.09.033.
[476] S. Jäckle, M. Liebhaber, C. Gersmann, M. Mews, K. Jäger, S. Christiansen, K. Lips, Potential of PEDOT:PSS as a hole selective front contact for silicon heterojunction solar cells, Sci. Rep. 7 (2017) 2170, https://doi.org/10.1038/s41598-017-01946-3.
[477] X. Jiang, P. Zhang, J. Zhang, J. Wang, G. Li, X. Fang, L. Yang, X. Chen, High Performance of PEDOT:PSS/n-Si solar cells based on textured surface with AgNWs electrodes, Nanoscale Res. Lett. 13 (2018) 53, https://doi.org/10.1186/s11671-018-2462-0.
[478] D. Zielke, R. Gogolin, M.-U. Halbich, C. Marquardt, W. Lövenich, R. Sauer, J. Schmidt, Large-Area PEDOT:PSS/c-Si Heterojunction Solar Cells With Screen-Printed Metal Contacts, Sol. RRL 2 (2018) 1700191, https://doi.org/10.1002/solr.201700191.
[479] Y. Liu, N. Sun, J. Liu, Z. Wen, X. Sun, S.-T. Lee, B. Sun, Integrating a silicon solar cell with a triboelectric nanogenerator via a mutual electrode for harvesting energy from sunlight and raindrops, ACS Nano 12 (2018) 2893–2899, https://doi.org/10.1021/acsnano.8b00416.
[480] H. Tong, Z. Yang, X. Wang, Z. Liu, Z. Chen, X. Ke, M. Sui, J. Tang, T. Yu, Z. Ge, Y. Zeng, P. Gao, J. Ye, Dual functional electron-selective contacts based on silicon oxide/magnesium: tailoring heterointerface band structures while maintaining surface passivation, Adv. Energy Mater. 8 (2018) 1702921, https://doi.org/10.1002/aenm.201702921.
[481] C. Zhang, Y. Zhang, H. Guo, Q. Jiang, P. Dong, C. Zhang, Efficient planar hybrid n-Si/PEDOT:PSS solar cells with power conversion efficiency up to 13.31% achieved by controlling the SiOx interlayer, Energies 11 (2018), https://doi.org/10.3390/en11061397.
[482] J. Zhu, X. Yang, J. Sheng, P. Gao, J. Ye, Double-Layered PEDOT:PSS Films Inducing Strong Inversion Layers in Organic/Silicon Hybrid Heterojunction Solar Cells, ACS Appl. Energy Mater. 1 (2018) 2874–2881, https://doi.org/10.1021/acsaem.8b00533.
[483] K. Kasahara, J. Hossain, D. Harada, K. Ichikawa, R. Ishikawa, H. Shirai, Crystalline-Si heterojunction with organic thin-layer (HOT) solar cell module using poly(3,4-ethylenedioxythiophene):poly(styrene sulfonate)(PEDOT:PSS), Sol. Energy Mater. Sol. Cells 181 (2018) 60–70, https://doi.org/10.1016/j.solmat.2017.10.016.
[484] A.A. Al-Muntaser, M.M. El-Nahass, A.H. Oraby, M.S. Meikhail, H.M. Zeyada, Fabrication and transport mechanisms of 5,10,15,20-tetraphenyl-21H,23H-porphrine manganese(III) chloride/n-type silicon heterojunction solar cell, J. Mater. Sci.: Mater. Electron. 29 (2018) 10911–10920, https://doi.org/10.1007/s10854-018-9169-y.
[485] Z. Zou, W. Liu, D. Wang, Z. Liu, E. Jiang, S. Wu, J. Zhu, W. Guo, J. Sheng, J. Ye, Electron-selective quinhydrone passivated back contact for high-efficiency silicon/organic heterojunction solar cells, Sol. Energy Mater. Sol. Cells 185 (2018) 218–225, https://doi.org/10.1016/j.solmat.2018.05.041.
[486] L. Yang, J. Chen, K. Ge, J. Guo, Q. Duan, F. Li, Y. Xu, Y. Mai, Polymer/Si heterojunction hybrid solar cells with rubrene:DMSO organic semiconductor film as an electron-selective contact, J. Phys. Chem. C. 122 (2018) 23371–23376, https://doi.org/10.1021/acs.jpcc.8b07987.
[487] L. Zhang, Z. Wang, H. Lin, W. Wang, J. Wang, H. Zhang, J. Sheng, S. Wu, P. Gao, J. Ye, T. Yu, Thickness-modulated passivation properties of PEDOT:PSS layers over crystalline silicon wafers in back junction organic/silicon solar cells, Nanotechnology 30 (2019) 195401, https://doi.org/10.1088/1361-6528/ab012d.
[488] M.-U. Halbich, D. Zielke, R. Gogolin, R. Sauer-Stieglitz, W. Lövenich, J. Schmidt, Improved surface passivation and reduced parasitic absorption in PEDOT:PSS/c-Si heterojunction solar cells through the admixture of sorbitol, Sci. Rep. 9 (2019) 9775, https://doi.org/10.1038/s41598-019-46280-y.
[489] X.-G. Hu, P.-X. Hou, J.-B. Wu, X. Li, J. Luan, C. Liu, G. Liu, H.-M. Cheng, High-efficiency and stable silicon heterojunction solar cells with lightly fluorinated single-wall carbon nanotube films, Nano Energy 69 (2020) 104442, https://doi.org/10.1016/j.nanoen.2019.104442.
[490] L.-M. Yu, T. Chen, N. Feng, R. Wang, T. Sun, Y. Zhou, H. Wang, Y. Yang, Z.-H. Lu, Highly conductive and wettable PEDOT:PSS for simple and efficient organic/c-Si planar heterojunction solar cells, Sol. RRL 4 (2020) 1900513, https://doi.org/10.1002/solr.201900513.
[491] L. Lancellotti, E. Bobeico, M. Della Noce, L.V. Mercaldo, I. Usatii, P. Delli Veneri, G.V. Bianco, A. Sacchetti, G. Bruno, Graphene as non conventional transparent conductive electrode in silicon heterojunction solar cells, Appl. Surf. Sci. 525 (2020) 146443, https://doi.org/10.1016/j.apsusc.2020.146443.
[492] W. Fang, P. Wang, Z. Ni, T. Sun, C. Xiang, K. Yue, R. Wang, J. Yang, Y. Zhou, C. Wang, Y. Yang, Planar Organic-Si Hybrid Solar Cell with MoOx Mixed PEDOT:PSS as Hole Injection Layer Profits from Mo5+ and Mo6+ Synergistic Effects, Adv. Mater. Interfaces 7 (2020) 2000754, https://doi.org/10.1002/admi.202000754.
[493] K.K. Markose, M. Jasna, P.P. Subha, A. Antony, M.K. Jayaraj, Performance enhancement of organic/Si solar cell using CNT embedded hole selective layer, Sol. Energy 211 (2020) 158–166, https://doi.org/10.1016/j.solener.2020.09.024.
[494] R. Shen, Z. Sun, Y. Shi, Y. Zhou, W. Guo, Y. Zhou, H. Yan, F. Liu, Solution Processed Organic/Silicon Nanowires Hybrid Heterojunction Solar Cells Using Organosilane Incorporated Poly(3,4-ethylenedioxythiophene):poly (styrenesulfonate) as hole transport layers, ACS Nano 15 (2021) 6296–6304, https://doi.org/10.1021/acsnano.0c10526.
[495] Y. Zhao, L. Zhang, M. Lv, C. Jiao, P. Cheng, Y. Fu, J. Li, Q. Liu, D. He, Improvement of the optoelectrical properties of a transparent conductive polymer via the introduction of ITO nanoparticles and its application in crystalline silicon/organic heterojunction solar cells, ACS Appl. Mater. Interfaces 13 (2021) 31171–31179, https://doi.org/10.1021/acsami.1c07415.
[496] S.A. Al-Ghamdi, A.A.A. Darwish, T.A. Hamdalla, K.F. Abd El-Rahman, Electronic and photovoltage performance of TTBTP/n-Si heterojunctions for possible use in solar cell, Mater. Sci. Semicond. Process. 130 (2021) 105828, https://doi.org/10.1016/j.mssp.2021.105828.
[497] Z. Lu, G. Hou, J. Chen, J. Xu, K. Chen, Achieving a record open-circuit voltage for organic/si hybrid solar cells by improving junction quality, Sol. RRL 5 (2021).
[498] Y. Kurushima, N. Katsuyama, H. Okuzaki, Effect of PEDOT:PSS composition on photovoltaic performance of PEDOT:PSS/n-Si hybrid solar cells, Jpn. J. Appl. Phys. 60 (2021) 091001, https://doi.org/10.35848/1347-4065/ac19d2.
[499] H. Guo, T. Chen, L. Yu, A. Chen, T. Sun, J. Wang, C. Wang, J. Zhang, Y. Yang, Enhanced performance of Si/PEDOT: PSS heterojunction solar cells via multi-walled carbons coated with polydopamine, Opt. Mater. 120 (2021) 111375, https://doi.org/10.1016/j.optmat.2021.111375.
[500] M. Lv, Z. Wang, C. Jiao, Y. Zhao, L. Jin, Y. Fu, Q. Liu, D. He, High-Efficiency Si/PEDOT:PSS hybrid heterojunction solar cells using solution-processed graphene oxide as an antireflection and inversion-induced layer, ACS Appl. Energy Mater. 4 (2021) 13279–13287, https://doi.org/10.1021/acsaem.1c02869.
[501] N.Y. Park, G.S. Jeong, Y.J. Yu, Y.C. Jung, J.H. Lee, J.H. Seo, J.Y. Choi, Photovoltaic Device Application of a Hydroquinone-Modified Conductive Polymer and Dual-Functional Molecular Si Surface Passivation Technology, Polym. (Basel) 14 (2022), https://doi.org/10.3390/polym14030478.
[502] C. Li, Z. He, Q. Wang, J. Liu, S. Li, X. Chen, W. Ma, Y. Chang, Performance Improvement of PEDOT:PSS/N-Si Heterojunction Solar Cells by Alkaline Etching, Silicon 14 (2022) 2299–2307, https://doi.org/10.1007/s12633-021-01034-2.
[503] W. Zhou, H. Zhang, J. Wang, Q. Wei, Z. Chen, C. Wang, Y. Yang, High conductivity PEDOT:PSS thin films affording improved open circuit voltages in PEDOT:PSS-Si heterojunction solar cells, Mater. Lett. 312 (2022) 131466, https://doi.org/10.1016/j.matlet.2021.131466.
[504] R. Shen, Z. Sun, Y. Zhou, Y. Shi, J. Shang, H. Chen, Y. Zhou, F. Liu, Organic/silicon nanowires hybrid solar cells using isobutyltriethoxysilane incorporated poly(3,4-ethylenedioxythiophene):poly (styrenesulfonate) as hole transport layer, Prog. Photovolt.: Res. Appl. 30 (2022) 661–669, https://doi.org/10.1002/pip.3540.
[505] Z. Ni, S. Ding, H. Zhang, R. Dai, A. Chen, R. Wang, J. Zhang, Y. Zhou, J. Yang, T. Sun, G. Hu, Phosphorus and Selenium Co-Doped WO3 nanoparticles for interface modification and photovoltaic properties enhancement of monolayer planar silicon/PEDOT:PSS hybrid solar cells, Adv. Mater. Interfaces 9 (2022) 2200812, https://doi.org/10.1002/admi.202200812.
[506] Q. Gao, J. Yan, L. Wan, C. Zhang, Z. Wen, X. Zhou, H. Li, F. Li, J. Chen, J. Guo, D. Song, B.S. Flavel, J. Chen, High-efficiency graphene-oxide/silicon solar cells with an organic-passivated interface, Adv. Mater. Interfaces 9 (2022) 2201221, https://doi.org/10.1002/admi.202201221.
[507] H.H. Hegazy, A.M. Afzal, A. Dahshan, M.W. Iqbal, I. Kebaili, High-performance 2D/3D hybrid dimensional p–n heterojunction solar cell with reduced recombination rate by an interfacial layer, J. Mater. Chem. C. 10 (2022) 14982–14992, https://doi.org/10.1039/D2TC02548E.
[508] C. Zhang, B. Chen, X. Zhang, J. Yan, J. Chen, Q. Gao, X. Zhou, J. Guo, F. Li, J. Wang, D. Song, S. Wang, J. Chen, Large area and high-efficiency MXene–silicon

solar cells by organic enhanced dispersity and work function, Sol. RRL 6 (2022) 2200743, https://doi.org/10.1002/solr.202200743.
[509] C. Yang, Z. Luo, W. Ma, S. Li, G. Lv, K. Fu, K. Liu, H. Li, H. Sun, X. Chen, Study on the Fabrication of PEDOT:PSS/Si Hybrid Solar Cells Incorporated with F4TCNQ and VTMO, J. Phys. Chem. C. (2023).
[510] X.-G. Hu, Y.-M. Zhao, H. Yang, P.-X. Hou, C. Liu, J. Chang, Y. Hao, Interfacial chemical bridging constructed by multifunctional lewis acid for carbon nanotube/silicon heterojunction solar cells with an efficiency approaching 17.7%, Adv. Sci. 10 (2023) 2206989 https://doi.org/10.1002/advs.202206989.
[511] T. Tom, E. Ros, J. López-Vidrier, J.M. Asensi, P. Ortega, J. Puigdollers, J. Bertomeu, C. Voz, Poly(amidoamine) Dendrimer as an Interfacial Dipole Modification in Crystalline Silicon Solar Cells, J. Phys. Chem. Lett. 14 (2023) 4322–4326, https://doi.org/10.1021/acs.jpclett.3c00643.
[512] M.A.A. Rosle, H.D. Omar, M.Z. Pakhuruddin, PEDOT:PSS emitter on textured monocrystalline silicon solar cells, J. Mater. Sci.: Mater. Electron. 34 (2023) 1533, https://doi.org/10.1007/s10854-023-10944-3.
[513] W. Jiang, Y. Wang, C. Jiao, Y. Wang, Y. Zhao, M. Lv, Z. Fan, Y. Fu, J. Li, Q. Liu, D. He, Solution-Processed PEDOT:PSS/p-Si/ZnO Heterojunction Solar Cells, Phys. Status Solidi (RRL) – Rapid Res. Lett. 17 (2023) 2300168, https://doi.org/10.1002/pssr.202300168.
[514] D. Sharma, A. Srivastava, J.S. Tawale, P. Prathap, S.K. Srivastava, High efficiency flexible PEDOT:PSS/silicon hybrid heterojunction solar cells by employing simple chemical approaches, J. Mater. Chem. C. 11 (2023) 13488–13502, https://doi.org/10.1039/D3TC02236F.
[515] Y. Wang, W. Jiang, Y. Zhao, M. Lv, Y. An, Y. Wang, Q. Zhang, H. Liu, C. Liu, Z. Fan, Q. Liu, D. He, Structural Design and Simple Posttreatment of the Hole Transport Layer to Improve Performance of Hybrid Solar Cells, Phys. Status Solidi (RRL) – Rapid Res. Lett. 17 (2023) 2300086, https://doi.org/10.1002/pssr.202300086.
[516] U. Punia, P. Kumari, R.K. Sharma, S. Laxmi, R. Srivastava, S.K. Srivastava, Fabrication of low-cost and efficient PEDOT:PSS-silicon hybrid heterojunction solar cell via tailoring the organic layer thickness, J. Mater. Sci.: Mater. Electron. 35 (2023) 42, https://doi.org/10.1007/s10854-023-11812-w.
[517] Y. Cui, J. Wei, Y. Xiong, Q.-Y.T. Shang, Q. Liu, L. Huang, Y. Zhang, W. Yu, PEDOT:PSS-Nafion/n-Si hybrid heterojunction TOPCon solar cells: experiment and simulation, J. Phys. Chem. C. 128 (2024) 2767–2775, https://doi.org/10.1021/acs.jpcc.3c07469.
[518] A. Srivastava, R.K. Sharma, U. Punia, S.K. Srivastava, Rapid and low temperature micro inverted pyramid texturing of silicon via copper catalyzed chemical etching for high efficiency PEDOT:PSS/silicon hybrid solar cells, Surf. Interfaces 46 (2024) 104066, https://doi.org/10.1016/j.surfin.2024.104066.